**Phase Evolution During Mechanical Milling of Pre-alloyed Gas Atomized Maraging Steel
Powders and Magnetic Characterization**

by

Ganesh Varma Thotakura

**A thesis submitted in partial fulfillment
of the requirements for the degree of
Master of Science
(Mechanical Engineering)
in the University of Michigan-Dearborn
2019**

Master's Thesis Committee:

    Assistant Professor Tanjore V. Jayaraman, Chair
    Professor Hong-Tae Kang
    Professor Pravansu S. Mohanty

ACKNOWLEDGEMENTS

TABLE OF CONTENTS

LIST OF TABLES

LIST OF FIGURES

ABSTRACT

Maraging steels are an important class of high strength steels that exhibit an exciting combination of magnetic and mechanical properties. Past research work, specifically on the magnetic properties, focused on improving the magnetic properties of the bulk form of the steel, fabricated by conventional materials processing and manufacturing. With the recent focus towards additive manufacturing, it is imperative to investigate the structure and magnetic properties of the maraging steel powder and the influence of temperature.

In this thesis work, firstly, the structural and magnetic characterization of a commercially available pre-alloyed gas atomized powder was investigated. It comprised of primarily the martensite phase (α) and a small amount of austenite (γ). The powder particle size characteristics, D_{90} of the as-received powder was estimated as ~21 μm. The saturation magnetization (M_S), intrinsic coercivity (H_{CI}), and remanent magnetization (M_R) of the as-received powder, at ambient temperature, was ~176 Am^2/kg, ~3 kA/m, and ~1.4 Am^2/kg, respectively. Thermal treatment of the powder up to 900 K for ~1 h showed an inappreciable change in M_S, while the coercivity decreased, suggesting good magnetic properties and promising opportunities to reuse the powder.

Subsequently, phase evolution during mechanical milling of the pre-alloyed powder was investigated. Powder milled from 3 h to 8 h comprised nanocrystalline martensitic phase. The estimated grain size was as low as ~20 nm. The M_S, H_{CI}, and M_R ranged between ~164 Am^2/kg and ~169 Am^2/kg, ~4.9 kA/m and ~6.7 kA/m, and ~3.4 Am^2/kg to ~3.9 Am^2/kg, respectively. Milling more than 8 h resulted in the formation of austenite and extraneous intermetallic phases, resulting in the reduction of M_S and increase in H_{CI}. At cryogenic temperatures (60 K-300 K), $M_S(0)$ (M_S at 0 K) and maximum magnetic moment per atom (μ_H) of the nanocrystalline milled maraging powders were ~ 178 Am^2/kg and ~ 1.83 μ_B, respectively. The thermally treated maraging steel powders retained the nanostructure, and their M_S and H_{CI} were comparable to as-received powder.

CHAPTER 1: INTRODUCTION

1.1 Maraging steels

Maraging steels are an important class of high-strength steels characterized by the low carbon content (~0.01 wt.%) and principal alloying additions (e.g. Ni, Co, Mo, etc.) [1]. The strengthening effect is because of the precipitation of intermetallics during the aging process [1-7]. The term "maraging" was obtained from the combination of "mar" from martensite and "aging" from age hardening.

The 18 wt.% Ni maraging steels were discovered by Decker et al. in 1960 [1]. There are different grades of maraging steels, which are 18 Ni (200), 18 Ni (250), 18Ni (300) and 18 Ni (350). These alloys typically constitute 18 wt.% of Ni and differ in the wt.% of Co, Mo, and Ti and attain yield strength of 200 ksi, 250 ksi, 300 ksi, and 350 ksi respectively. Ti plays as a supplementary hardener and in being a refining agent of residual carbon. Precipitation hardening of maraging steel is due to the formation of precipitates of the intermetallic compounds between Ni and Mo, Ni and Ti or between other alloying elements and Ni or other element combinations. These improve the steel properties, characterized by high tensile strength combined with high toughness and good weldability and malleability.

Several research investigations were carried out on studying the effects on the properties of these steels due to the synthesizing techniques, processing variables such as aging duration, aging temperatures, and changes in the composition, etc. These steels find a wide range of applications including, but not limited to, aerospace (e.g. larger, smaller, and multi-purpose rocket motor casing, aircraft forgings, helicopter landing leg, etc.); hydrospace (e.g. pressure hulls for deep submergence vehicles); tooling (e.g. dies, cores, core pins, bolts, punches, extrusion rams, etc.); structural (e.g. index plate for mounting on a turret, load cell, flexural pivot, leg, etc.) and so forth [1-15].

Later, it was found that these maraging steels can be used in high-speed rotors, hysteresis motors, sensors for force-related parameters, etc. [20-27]. These applications require a relatively good combination of magnetic and mechanical properties. Generally, maraging steels when cooled from austenitizing temperature is predominantly comprised of high ductile martensite phase along with the retained austenite and intermetallic precipitates. The martensite phase exhibits decent magnetic properties. From the past research work, using conventional material processing and manufacturing estimated the magnetic properties differ as a function of aging temperature [22, 25-26]. The retained austenite affects the saturation magnetization (M_S) and coercivity (H_{CI}). The increase in the volume percentage of the austenite phase generally tends to increase H_{CI} and contrarily reduce M_S. Also, the increase in the Ni content and cold working before aging showed a decrement in H_{CI} and M_S. Thus, to achieve desirable magnetic properties, the austenite formation should be maintained as low as possible.

With the recent focus towards additive manufacturing, it is imperative to investigate the structure and magnetic properties in the powder form of maraging steel. Firstly, commercially available gas-atomized powder has not been characterized for magnetic properties. It is important to characterize the magnetic properties and their thermal stability. Secondly, grain size and the phase distribution significantly affect the magnetic properties. Mechanical milling is known to reduce particle size, grain size, and induce phase transformations [31]. Hence, it is essential to investigate the phase evolution and associated changes in the magnetic properties during mechanical milling.

Current research work investigates phase evolution during mechanical milling at ambient temperature and pressure of the commercially available pre-alloyed gas-atomized powder. The changes in the structural and magnetic properties of the commercially available pre alloyed gas-atomized maraging steel powder and the milled powders with the increase in hours of milling duration, up to ~60 h, were investigated. The structure and magnetic properties of the gas-atomized and the milled maraging steel powders were compared. The magnetic properties of these powders are measured and compared from cryogenic temperatures as low as ~60 K to elevated temperatures as high as ~900 K. The changes in the structural and magnetic properties due to the thermal treatments on these powders were also studied at ambient and sub-ambient temperatures.

CHAPTER 2: LITERATURE REVIEW AND BACKGROUND

2.1 Metallurgical behavior of maraging steels

Maraging steels metallurgical behavior is associated with the thermal hysteresis between the formation of martensite on cooling and its reversion to austenite on heating in the Fe-Ni alloys [1-2]. These alloys containing 3-30 wt.% Ni content, at lower temperatures, show the equilibrium phases of ferrite and austenite. However, in practice, it appears that by cooling from austenite field region, the alloys containing between ~10-25 wt.% Ni content will not decompose into the equilibrium austenite and ferrite compositions as predicted from the phase diagram, even if held for a sufficiently long time in the two-phase region. Instead, the austenite transforms to a b.c.c. martensite. Also, the martensite transformation temperatures (M_s) depends on the nickel content and is shown in Figure 1.
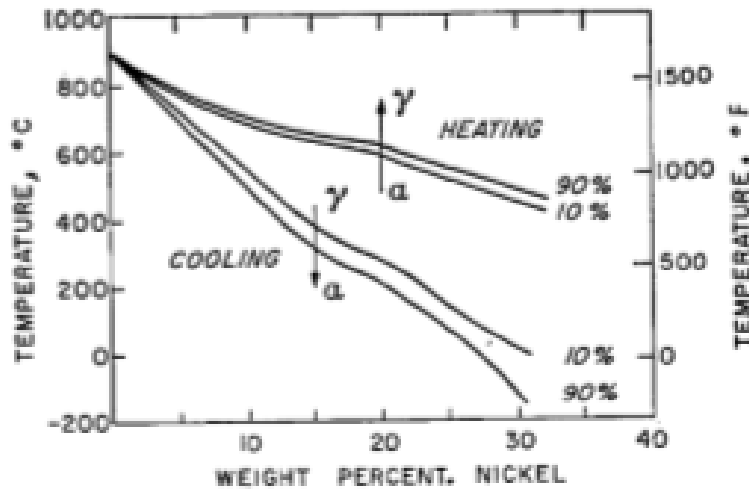
Figure 1 Metastable Fe-rich Fe-Ni phase diagram [1]

Later, it was found that a variety of transformations can take place in these alloys. The transformation of austenite to ferrite occurs for Ni content in the range of 0-5% and is independent

of the cooling rate. While in the range of 5-10 wt.% Ni, the transformation of austenite to ferrite occurs at slower cooling rates and the transformation of austenite to martensite at higher cooling rates. With further increase in the %, Ni content lowers the cooling rate necessary to form martensite. Lath (massive) martensite is formed when the range is in between ~10-25 % Ni.

On the other hand, with above 25 wt.% Ni, two types of martensite morphologies form which are twinned structure martensite and surface martensite. Alloying elements also affect the M_s temperature. Alloying elements generally lower the M_s temperature, but the effect of any individual addition often is not constant but depends upon the total composition of the alloy. One rather significant exception is cobalt, which raises the M_s temperature in Fe-Ni alloys and maraging steels.

Aging the maraging steels in complete martensite phase leads to the formation of several precipitates of intermetallic compounds. Some of them are η-Ni$_3$(Ti, Mo), Fe$_2$(Mo, Ti), and Fe$_3$Mo, etc. Many investigators suggested that these precipitates were of different geometrical shapes such as needles, disks, and ribbons, etc. Most often, the precipitate of Ni$_3$Mo tends to form during the initial stages of aging. While aging for longer durations or at higher temperatures lead to the formation of more stable Fe$_2$Mo precipitate. These precipitates lead to the strengthening of maraging steel. Another vital contribution of strengthening is due to the combination of Co and Mo. Addition of cobalt lowers the solubility of molybdenum in the martensite matrix, and thus increases the amount of Mo-containing precipitates.

Austenite reversion takes place if the martensite is reheated to a temperature below the A_s temperature the martensite will decompose into the equilibrium austenite and ferrite compositions. On the other hand, the alloy is heated above the A_s temperature; the martensite transforms by a shear transformation back to austenite of the same composition. Also, the rate of reversion of austenite is composition dependent. It was found that increasing the nickel content generally accelerates the austenite formation. The effect of other alloying elements on the austenitic reversion depends on whether the element is an austenitic stabilizer or not. However, the precipitation reactions have a significant influence on the reversion when compared to the alloying elements. The presence of austenite affects both mechanical and magnetic properties. Presence of austenite reduces the strength but improves the ductility of the steel. The magnetization of the steel reduces due to the presence of the austenite.

2.2 Structural and mechanical properties of maraging steel powders

In 1998, M. Farooque et al., investigated the nucleation mechanism of reverted austenite, especially coupled twin morphology(inter-lath martensite and intra-lath martensite) performed annealing on 18% Ni 350 grade maraging steel (with a chemical composition as mentioned in Table 1) samples of size 4mm×5 mm×30 mm size and were encapsulated individually in quartz tubes under a vacuum of 10^{-5} mbar. These samples were heat treated using two different heating rates, i.e., 523 and 1273 K/min. After heat treatment, they cut the samples into thin slices of 15 mm thick and 3 mm discs for which they used spark erosion machine. They used a scanning transmission electron microscope (STEM) equipped with an energy dispersive spectrometer working at an operating voltage of 200 keV for microstructural and crystallographic evaluations. Samples were made into thin foils using a twin-jet electro polisher using a solution of 10% perchloric acid in ethanol.

Table 1 Chemical composition of 18% Ni 350 grade maraging steel (wt.%) [50]

Ni	Co	Mo	Ti	Al	C	S	Fe
18	12	4.31.7	1.7	0.2	0.015	0.003	Balance

When heat treating the sample at a heating rate of 523 K/min to the austenite phase and continued with cooling back to room temperature results in the formation of reverted austenite of two types of morphology. They are inter-lath reverted austenite (which grows along the martensite lath boundaries), and intra-lath reverted austenite. The inter-lathe reverted austenite nucleate on the martensite lath boundaries. Along with both inter-lath and intra-lath austenite phases, Ni$_3$Ti precipitates also tend to form and are finely distributed throughout the martensite matrix, as shown in the bright-field micrograph in Figure 2a. The corresponding diffraction pattern (as shown in Figure 2c) showed the reflections of both precipitates and martensite matrix. The measured interplanar spacings of the different precipitate spots are in accordance with the η-Ni$_3$Ti phase.
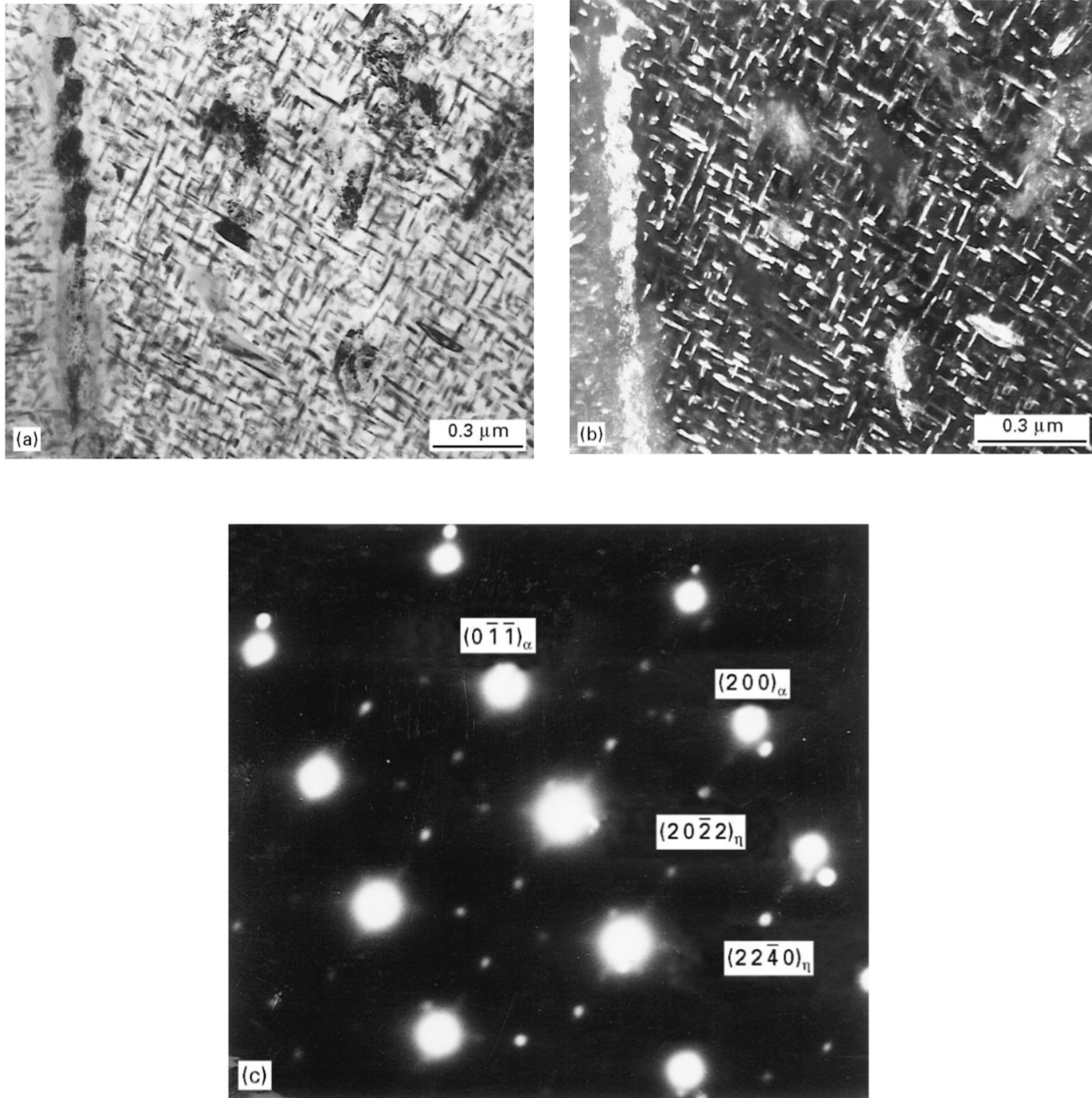
Figure 2 a) Bright-field transmission electron micrograph showing the growth of Ni_3Ti precipitates inside the martensite matrix, (b) the corresponding dark-field image with the precipitates highlighted, and (c) the corresponding electron diffraction pattern with the indexed planes marked [50]

Table 2 EDS analysis between the inter-lath and the intra-lath reverted austenite compositions [50]

Elements(wt.%)	Inter-lath austenite	Intra-lath austenite
Fe	59	57
Ni	21.6	24
Co	10	9.8
Mo	6.9	7
Ti	1.7	1.8

While heat treating at a faster heating rate of 1273 K/min to the austenite phase and continued with cooling back to room temperature resulted in the absence of the nucleation of γ-twins, although inter-lath reverted austenite was observed grown on the martensite lath boundaries. η-Ni_3Ti precipitate and the Mo enriched tend to form at the early stages of aging. Because of the faster heating rate (overaging), precipitate Fe_2Mo is formed.

From the EDS analysis between the inter-lath and the intra-lath reverted austenite, the composition of the two austenites are different, as shown in Table 2. Table 2 shows that the intra-lath reverted austenite is rich in Ni and Mo content, suggesting that a depleted region and an enriched region was obtained because of segregation of the alloying elements. Thus, the intra-lath austenite is grown on the Ni_3Ti precipitate sites, which are the enriched regions, having higher contents of Ni and Mo, and are formed by the dissolution of these precipitates, which leads to local Ni enrichment. Also from the morphology, orientation relationship and midrib of the intra-lath reverted austenite, they suggested that it nucleates by a diffusionless transformation mechanism and grows further by a diffusion-controlled shear motion.

In 2017, V. X. L. Filhoa et al., studied the influence of solution annealing on microstructure and mechanical properties of maraging 300 Steel.

Table 3 Chemical composition of maraging 300 steel (wt.%) [15]

Ni	Mo	Co	Ti	Al	C	Mn	Si	Fe
18.4	5.04	9.35	0.76	0.1	0.01	0.02	0.05	Bal

A maraging 300 steel round bar produced by vacuum induction melting process (VIM) followed by vacuum arc refining process (VAR), hot forged and solution annealed at 860 °C (for 10 hours to complete homogenization of the ingot). The chemical composition of the steel is presented in Table 3. Samples were cold-rolled and solution annealed at 860 ºC, 900 ºC, 950 ºC, 1000 ºC, 1050 ºC, 1100 ºC, and 1150 ºC for one hour. Some of the samples were aged at 480 °C for 3 hours to achieve peak hardness. Samples were quenched in water after each heat treatments to suppress the thermal embrittlement phenomena, which is usually observed in maraging steels after exposure to temperatures above 1100 °C.

Microstructural analysis performed by scanning electron microscope FEI XL30 on the maraging 300 samples produced by VIM followed by VAR, hot forged and solution annealed at 860 °C comprised the microstructure mainly martensite, as can be seen in Figure 3. X-ray diffraction patterns, as shown in Figure 4 were recorded using PANalytical X-Pert.-Pro diffractometer, which shows that the solution annealed and aged samples are mainly composed by the cubic phase martensite (α).
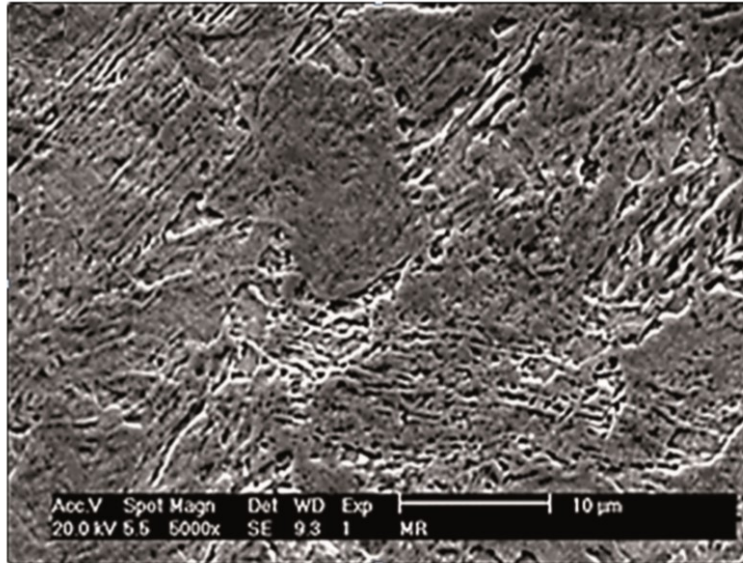
Figure 3 SEM image with 5000X magnification of maraging steel 300 [15]
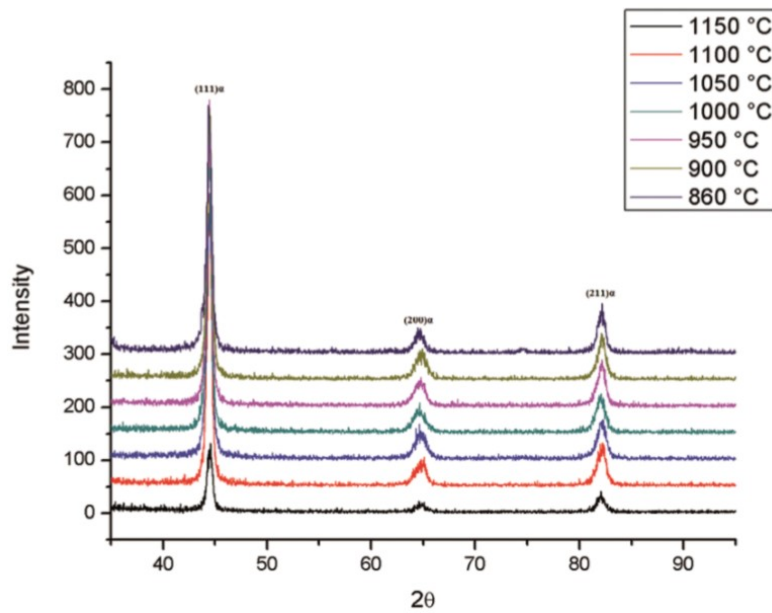
Figure 4 X-ray Diffraction patterns for samples annealed at various temperatures and aged at 480 °C [15]

Optical microscope images of annealed samples revealed uniform and equiaxed microstructure of prior austenite grains, without abnormal grain growth. The grain size tends to increase with the increase in the heat treatment temperature. Figure 5(a-g) shows typical

micrographs of samples annealed at temperatures of 860 ºC, 900 ºC, 950 ºC, 1000 ºC, 1050 ºC, 1100 ºC and 1150 ºC for 1 hour.
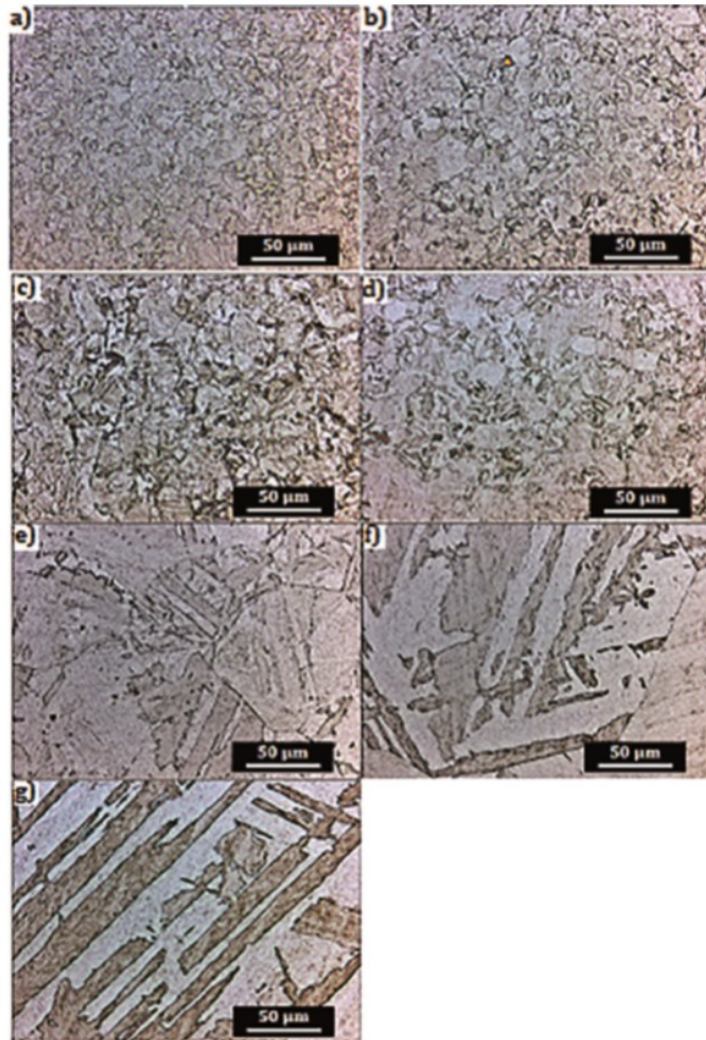
Figure 5 Microstructure of samples solution annealed for 1 hour at a) 860 °C, b) 900 °C, c) 950 °C, d) 1000 °C, e) 1050 °C f) 1100 °C g) 1150 °C. Magnification 500X [15]

The growth rate of the prior austenite grain size is relatively slow between 860 °C and 1000 °C and quickly rises above 1150 ºC, with values ranging approximately 8 µm at 860 °C to 164 µm for the sample annealed at 1150 °C. Measurement of the grain size for the annealed and aged samples revealed that there was small variation than those which were only annealed. The grain size for the sample annealed at 860 °C followed by aging is 6 µm and for the sample annealed at 1150 °C followed by the same aging process is 198 µm.
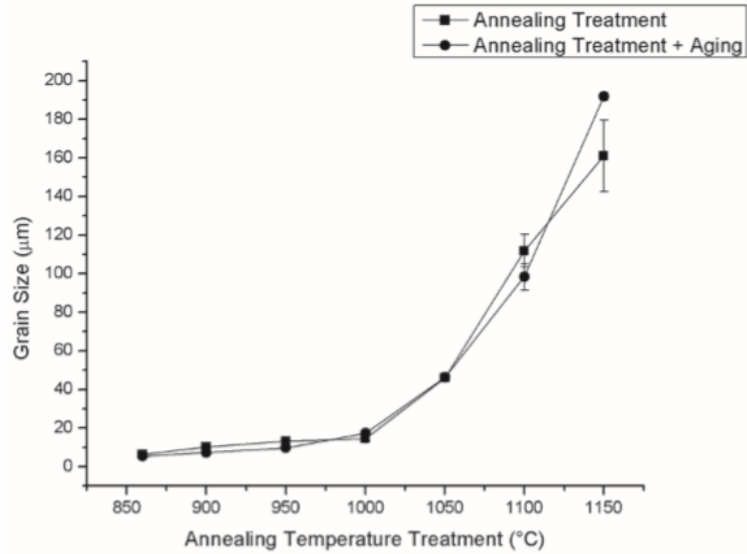
Figure 6 Prior austenite grain size for different annealing temperatures [15]

Annealing and aging affect the hardness and toughness in the maraging samples (as shown in Figures 7a and 7b). The hardness values for annealing and aged samples are almost double the values for samples subjected only to the solution treatment. While toughness showed an increase in the trend of Charpy energy for temperatures between 860 °C and 1000 °C, upon this temperature, it tends to fall back to reverse. They found that the material solution annealed, without aging heat treatment, presented absorbed energy of 48 J in the Charpy impact test. While the best result for aged samples was observed to be 23 J for the sample solution annealed at 1000 °C and aged for 3 hours at 480 °C.

11
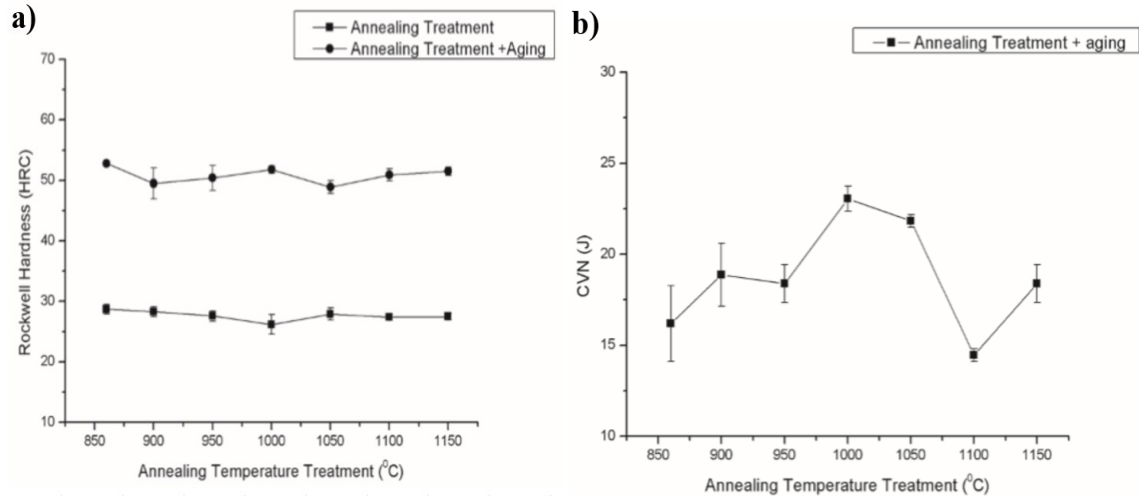
Figure 7 a) Results of the Rockwell Hardness tests of the solution treatment samples and solution treatment + aging samples; b) Charpy impact energy for samples solution annealed and aged at 480 °C [15]

In this work, even with the increase of the grain size, the increase in toughness of the material was observed, particularly when compared the results of solution annealed samples between 860 °C and 1000 °C and aged at 480 °C which is in contrary to the assumption stating grain growth of austenite result in martensite with lower ultimate strength and toughness. Only after the heat treatments performed above 1050 °C, they were possible to conclude that increased grain caused that reduction on the Charpy energy.

In 2016, A. Goncalves dos Reis et al., attempted to fill the gap of the phase transformation behavior of maraging steels with the help of high-temperature X-ray diffraction (HTXRD) technique. Maraging 300 steel samples were made into 20 mm×6 mm×1 mm thickness as a parallelepiped piece. The samples were solution annealed at 820 °C for 1 h and then air-cooled. They carried out in-situ HTXRD and room temperature X-ray diffraction (XRD) by using a Rigaku model Ultima IV diffractometer with Cu kα radiation ($\lambda = 0.15405$ nm) from a rotating anode (at 45 kV/40mA), on which a high-temperature chamber was mounted.

By heating the sample with a heating rate of 10 °C/min from room temperature to 800 °C, and recording sequence of X-ray diffraction patterns at different temperatures (400 °C, 500 °C, 600 °C, 650 °C, 700 °C, and 800 °C) in the 2θ range 42–46° is shown in Figure 8. These XRD patterns showed the more representative peaks of the martensite α(110) and austenite γ(111). The

12

microstructure that from room temperature until 600 °C the microstructure of the solution annealed sample was completely martensitic (α(110)) phase. From 650 °C until 800 °C, the microstructure gradually transformed from α— γ phase showed by the increasing peak intensity of γ (111) and reduction in α(110). At 800 °C the microstructure is entirely γ(111) phase.
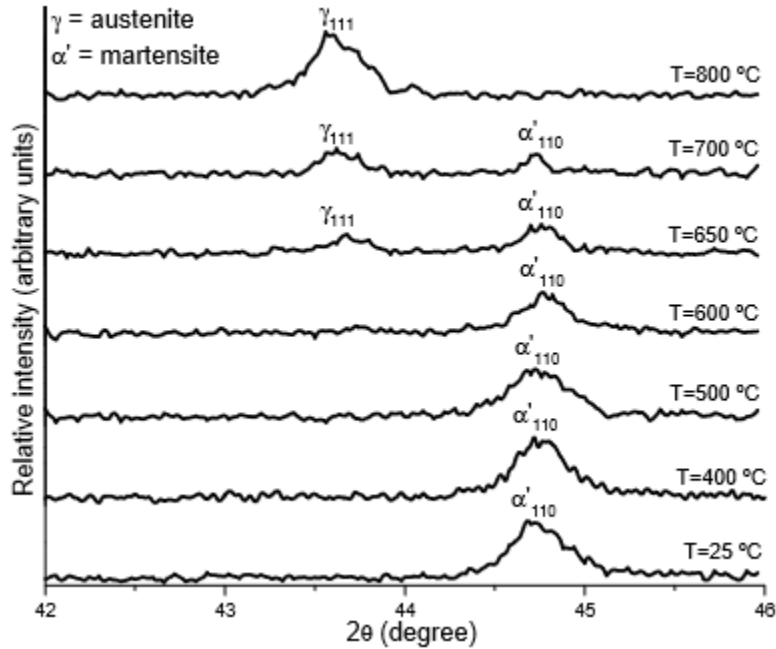
Figure 8 Sequence of X-ray diffraction patterns recorded upon the heating rate of 10 °C/min from room temperature to 800 °C showing peaks corresponding to the martensite(α) and austenite(γ) phases [19]

By heating the sample from room temperature to 600 °C at a heating rate of 10 °C/min and holding the sample at 600 °C and recording the XRD patterns analysis after 0, 0.25, 1, 2, 3 and 4 hours, consecutively is shown in Figure 9a. The martensite reversion to austenite was influenced by high temperature (600 °C) exposure time was conclusive from the XRD pattern. The volume fraction of austenite increased with increasing time of exposure at 600 °C, as shown in Figure 9b, reaching 50/50 volume fraction of austenite and martensite after 4 hours of exposure. They concluded that austenite reversion could occur when these alloys are held at temperatures below the A_s for prolonged periods because the martensite that formed during solution treatment is metastable and the system decomposes to the equilibrium austenite and ferrite structures via diffusion-controlled reactions. Dissolution of metastable nickel-rich precipitate particles in favor of equilibrium iron-rich precipitates locally enriches the matrix in nickel, which favors austenite

formation. Upon increasing the exposure time at 600 °C, more nickel-enriched is available in some areas of the matrix, and more martensite converted to austenite.
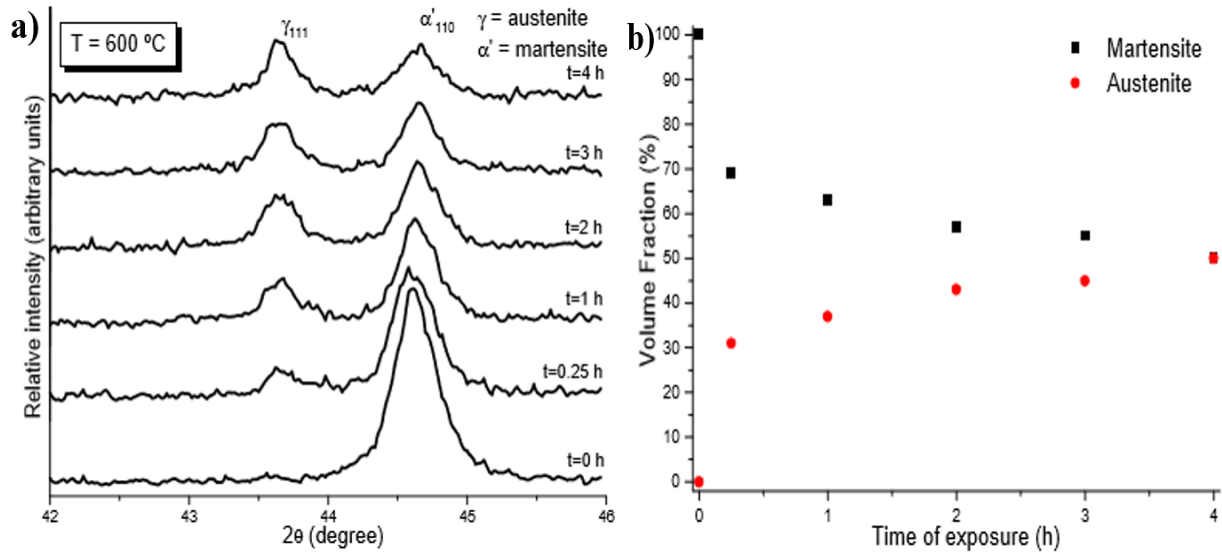
Figure 9 a) Sequence of X-ray diffraction patterns recorded upon the heating rate of 10 °C/min from room temperature and held at 600 °C for 4 hours showing peaks corresponding to the martensite(α) and austenite(γ) phases. b) The volume fraction of martensite and reverted austenite phases versus time of exposure calculated from the sequence of X-ray diffraction patterns [19]

The X-ray diffraction pattern of the sample that was held for 4 hours at 600 °C at room temperature after cooling down in the air showed that the reverted austenite at high temperature is retained at room temperature. The volume fractions of austenite and martensite found by HTXRD are similar at room temperature XRD after the sample is cooled.

2.3 Structural and magnetic properties of maraging steel powders

In 1994, AHMED et al., studied the magnetic properties of maraging steel in relation to deformation and structural phase transformations. The chemical composition of the 18% Ni-2400 grade maraging steel used in the present study is given in Table 4. Samples were annealed at 820 °C for 1 h in a vacuum furnace, and argon quenched to room temperature followed by rolling. Later they were aged for 1 h in a vacuum furnace.

Table 4 Chemical composition (wt.%) of 18% Ni-2400 grade maraging steel [22]

Element	Composition(wt.%)
Nickel	17.80
Cobalt	12.32
Titanium	1.70
Molybdenum	4.16
Silicon	0.08
Aluminum	0.08
Carbon	<0.01
Iron	Balance

Magnetic properties (coercive field and saturation magnetization) as a function of aging temperature both for the cases of annealed and cold rolled samples is shown in Figures 10a and 10 b. Coercive field increases gradually as a function of aging temperature to a maximum of ~ 160 Oe, at 680 °C and 650 °C for the annealed and cold rolled specimens, respectively. Also, the coercive field for specimens that were aged following cold rolling is higher in the temperature range between 450 and 650 °C than for the annealed material. While the temperatures at the minimum in saturation magnetization are close to the temperatures at which maximum in coercivity is obtained. The saturation magnetization values have similar values until 550 °C for both annealed and cold rolled specimens. The saturation magnetization values in the temperature range from 590 °C to 690 °C are lower in the case of rolled specimens. In addition to the coercive field and saturation magnetization, remanence is also affected by prior treatment. The remanence is much higher for the case of specimens subjected to cold rolling before aging than for annealed material. From Figure 10 c, the remanence ratio (M_R/ M_S) as a function of aging temperature in the case of cold rolled and annealed specimens shows the ratio much higher for cold-rolled specimens at all aging temperatures.
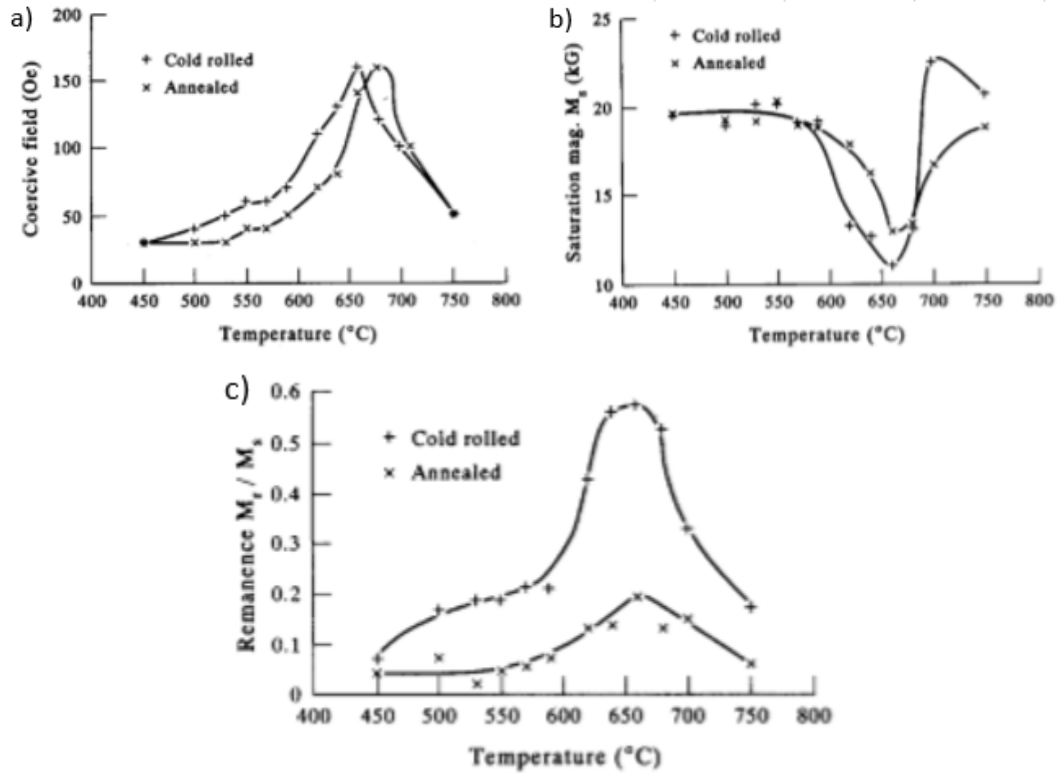
Figure: 10 a) Coercive field, b) Saturation magnetization (M_S) and c) Remanence ratio (M_R/ M_S) obtained in annealed, and cold rolled specimens as a function of aging temperature [22]

Figure 11 represents the X-ray spectra obtained from annealed and cold rolled specimens. The relative peak intensities from annealed specimens are different from the specimens that are cold rolled. The change in relative peak intensities is undoubtedly due to texture introduced during cold rolling. The amount of austenite formed at various temperatures for different degrees of deformation imparted by cold rolling is presented in Figure 12. It suggests that the reverted austenite for a particular aging temperature increases as the degree of deformation increases. In the case of cold rolling, 25-30% additional reverted austenite forms in comparison with annealed samples until ~680 °C. In contrast, at aging temperatures beyond ~ 700 °C, the cold rolled specimens show lower volume percent of reverted austenite in comparison with the annealed specimens.

16
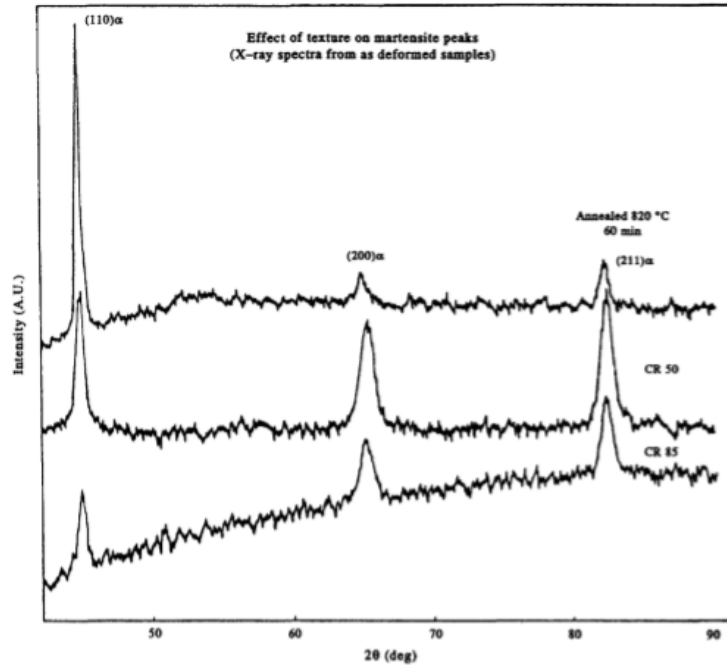
Figure 11 X-ray spectra obtained from annealed and cold rolled samples [22]
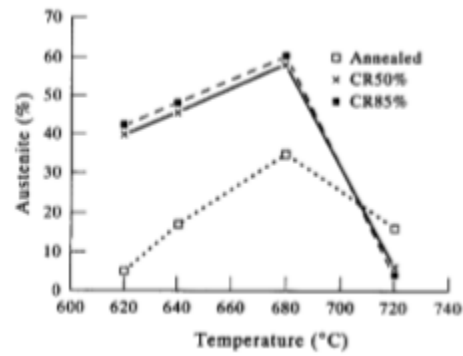
Figure 12 Effect of deformation on the vol. % of austenite formed at various aging temperatures [22]
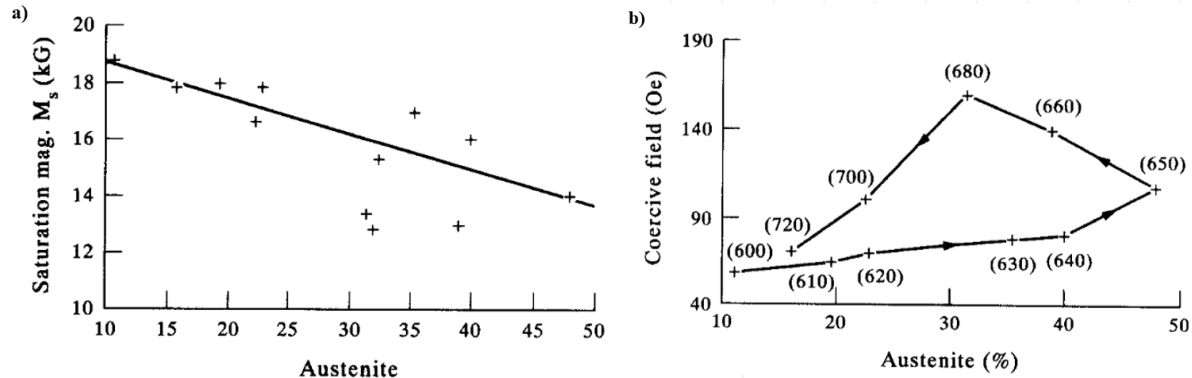
Figure 13 a) Saturation magnetization (M_S) and b) coercive field as a function of reverted austenite in the annealed specimens [22]

Saturation magnetization and coercive field as in Figure 13 a and b against the vol.% of reverted austenite obtained at various temperatures in specimens that were annealed before aging. Saturation magnetization decreases as the austenite content increases, which is expected if austenite is non-magnetic or weakly magnetic. Thus, it is conclusive that to achieve higher values in saturation magnetization, the amount of austenite should be kept at a minimum. The coercive field increases as the vol.% austenite increases in the temperature range between 600 °C to 650 °C. This trend reversed in the temperature range ~650 °C - 680 °C, where an increase in the coercive field is associated with a decrease in vol. % of reverted austenite. At temperatures beyond 680 °C, the coercive field decreases, and so does the vol. % of austenite. In the temperature range from 600 °C to 650 °C and at temperatures beyond 680 °C, it does appear that the coercive field rises and decreases proportionally with the austenite content. Also, samples when dipped in liquid nitrogen for 15 min after aging at 680 °C for 1 h. The magnetic properties were compared to the values determined before dipping. Dipping in liquid nitrogen transforms some of the retained austenite to martensite (3-4%). Saturation magnetization and coercive field values increased by 10 % and 5 % respectively. Thus, austenite content is not a favorable phase for magnetic properties.

In 1995, Ahmed et al. studied the influence of the nickel concentration on the magnetic properties of maraging steels. The alloys were made using a maraging steel grade 18% Ni-2400Mpa scrap. The chemical compositions of the alloys investigated are given in Table 5. Samples were annealed at 800 °C for 1 hour and followed by cold rolling. Samples were aged in a vacuum furnace for a fixed time period of 1 hour in the temperature range of 450 °C to 750 °C.

18

Table 5 Composition in wt.% of the alloys investigated [23]

Alloy	Composition in Wt %					
	Ni	Co	Mo	Ti	C	Fe
1	12.2	12.1	3.8	1.4	0.030	Bal
2	14.1	11.5	3.5	1.5	0.021	Bal
3	15.9	11.6	3.6	1.6	0.030	Bal
4	18.0	12.0	3.6	1.6	0.021	Bal
5	21.9	11.4	3.8	1.5	0.024	Bal
6	24.1	11.0	3.5	1.5	0.030	Bal

All the alloys except 24 wt.% Ni exhibited a martensitic structure following cooling from an elevated temperature. In the 24 wt.% Ni alloy, the transformation from high-temperature fcc phase to martensite phase did not take place. However, during the cold rolling of 24 wt.% Ni at 92% reduction it also transformed to martensite during rolling.

The coercive field and saturation magnetization values at different aging temperatures for all alloys showed a general trend and was quite similar in all alloys. The coercive field rises gradually up to about 600 °C. This is followed by a relatively sharp increase and equally sharp decrease beyond the maxima. While the saturation magnetization values showed a reverse trend to the coercive field, i.e., the rise in the coercivity is accompanied by a drop in saturation magnetization values. The minimum in saturation magnetization appears to be located at temperatures where the maximum in the coercive field was observed.

From Figure 14, the influence of Ni % on the coercive field at two different temperatures (at 500 °C and other at maxima) can be understood. A gradual rise in the coercive field observed up to 18 % Ni may be associated with the degree of precipitation induced during aging. Similarly, from Figure 15, the influence of Ni % on the saturation magnetization at two different temperatures (at 500 °C and other at maxima) can be understood. Both the values decrease almost linearly as a function of nickel concentration. Thus, it appears that the amount of Ni % and saturation magnetization are inversely proportional. The coercive field increased from ~55 to ~175 Oe, and the corresponding saturation magnetization decreased from ~18,500 to ~ 4000 G when the Ni % increased from 12 to 24 wt %.
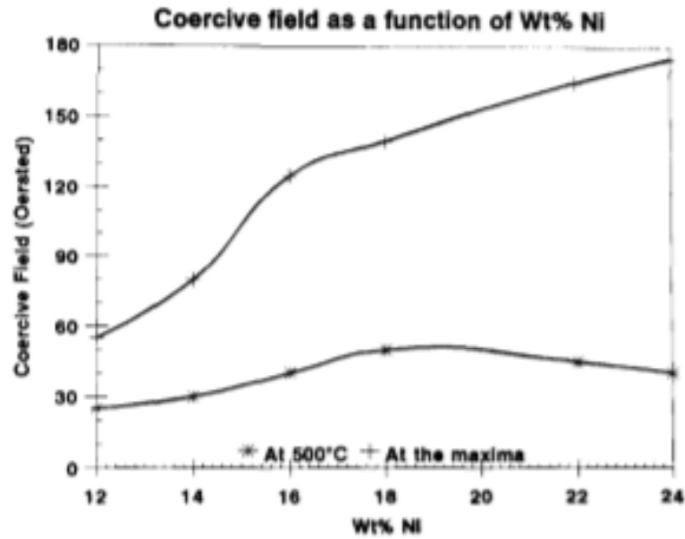
Figure 14 Coercive force plotted as a function of Ni % [23]
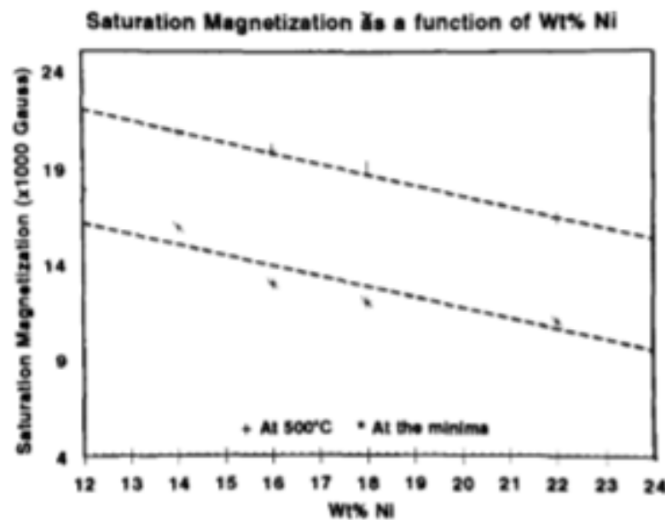
Figure 15 Saturation magnetization plotted as a function of Ni % [23]

In 2003, Tavares et al. performed a thermomagnetic study of the martensite(α)–austenite (γ) phase transition in the maraging 350 steel. A maraging 350 steel (19.8 %Ni, 10.7 %Co, 4.7 %Mo, 1.47 %Ti, 0.98 %Al, 0>0.007 %C, wt.%) was solution treated at 1000°C. After quenching, the steel was rolled from 5.5 to 1.1 mm at room temperature. The microstructure of the solution treated and deformed steel showed the presence of a completely α- phase, as shown in Figure 16.
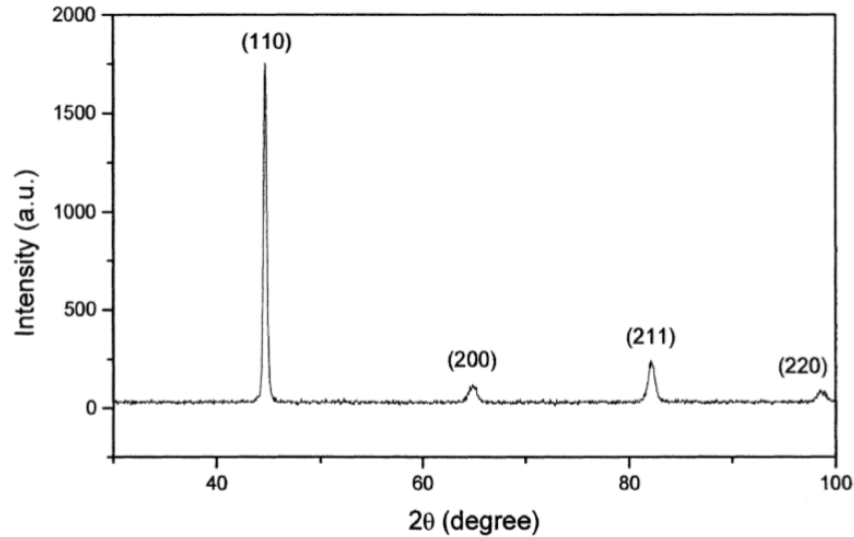
Figure 16 X-ray diffraction of the solution treated and deformed maraging 350 steel [24]

The thermomagnetic analysis (TMA) with heating and cooling rates of 10 °C/min (Figure 17) showed that the magnetization does not change significantly with temperature until 690 °C and then starts to decrease, reaching to zero at about 800°C. While cooling, the magnetization was not reversible until 175 °C, where it starts to recover the initial room temperature magnetization which is obtained at about 130°C. From the results shown in Figure 17 the A_s (austenite start temperature)-(690±10 °C), A_f (austenite finish temperature)- (800±10 °C), M_s (martensite start temperature)-(175±10 °C) and M_f (martensite finish temperature)-(130±10 °C) temperatures of the steel for the heat treatment rates used. A TMA experiment to 730 °C with a stop of 5 min at this temperature (Figure 18) showed that the magnetization was not reversible with cooling. This magnetization decrease between 690 °C and 800 °C could be due to the transformation from $\alpha \rightarrow \gamma$. The $\alpha \rightarrow \gamma$ transformation progressed isothermally, and during the cooling, however, the $\gamma \rightarrow \alpha$ did not occur till 100 °C. This is probably because the austenite formed was enriched with stabilizing elements.
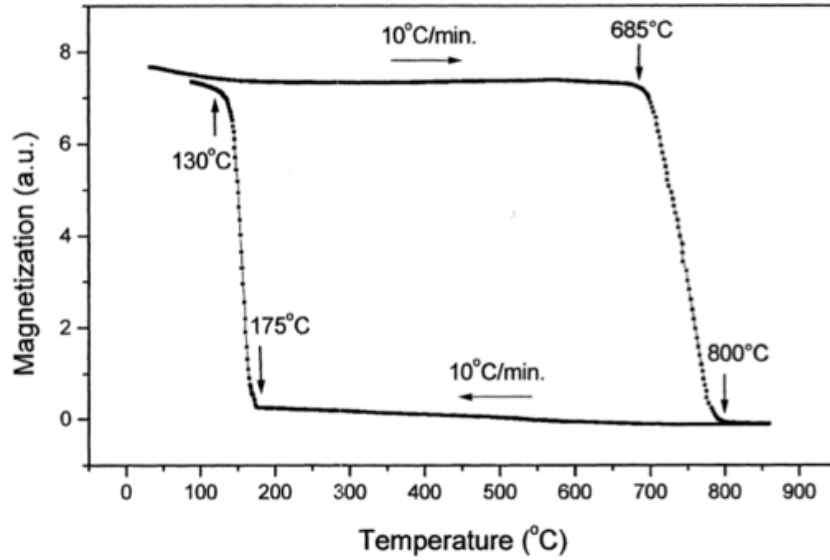
Figure 17 TMA curve of a maraging 350 steel [24]
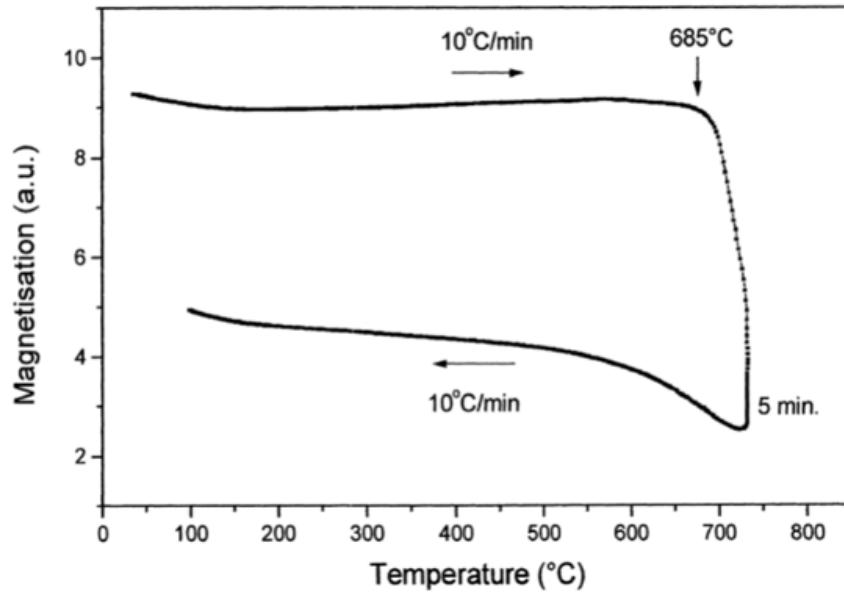
Figure 18 TMA curve up to 730 °C of the maraging 350 steel. The sample was kept for 5 min at 730 °C [24]

The TMA curve with the low heating rate (1°C/min) is compared with the TMA curve with a heating rate of 10 °C/min in Figure 19. With the low heating rate of 1°C/min a small decrease of magnetization was observed before the A_s temperature, which is attributed to the austenite formation associated with Fe_2Mo precipitation and $Ni_3(Mo, Ti)$ dissolution. Comparing the high

and low-speed curves, it is conclusive that Ni-enriched austenite starts at about 510 °C. Also, the A_s and A_f temperatures are lower in the low-speed curve, and it is rather an effect due to the rate of a test than due to the precipitation during the TMA.
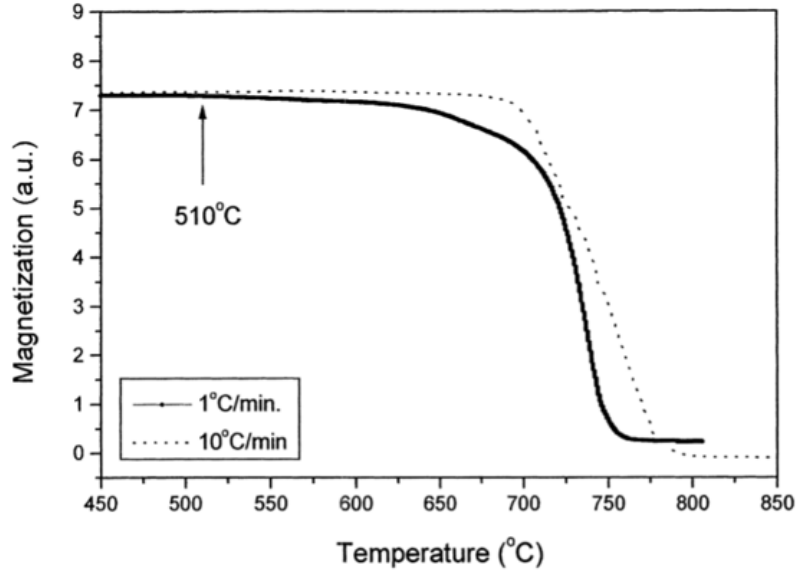
Figure 19 TMA heating curves obtained at 1 and 10°C/min [24]

TMA for three samples: unaged, aged at 560 °C, and aged at 650 °C for 5 h each with a heating rate of 10 °C/min is shown in Figure 20. The A_s temperature is not affected by the aging at 560 °C, but it is significantly increased by the aging at 650 °C. The formation of Ni-rich stable austenite during the aging retards the beginning of the $\alpha \rightarrow \gamma$ reaction. The M_s temperature is not affected by aging.
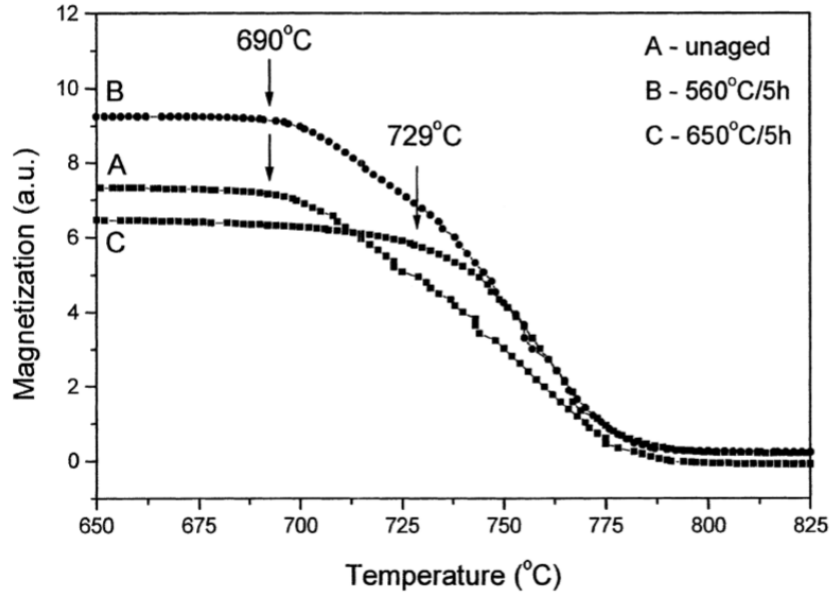
Figure 20 TMA heating curves of samples: unaged (A), aged at 560 °C (B), and aged at 650 °C (C) for 5 h [24]

A TMA curve, but with a higher holding duration for 30 minutes at 730 °C, as shown in Figure 21. In the TMA with 5 minutes holding duration they observed that after 5 min at 730 °C the $\alpha \rightarrow \gamma$ transformation progressed isothermally and during the cooling, however, the $\gamma \rightarrow \alpha$ did not occur till 100 °C. While in the TMA with 30 minutes holding duration at 730 °C, the M_s temperature could be measured (127 °C), but M_f was placed below 100 °C. Hence, with the increase of time at 730 °C promotes a higher homogenization of the austenite formed and, as a consequence, M_s increased.
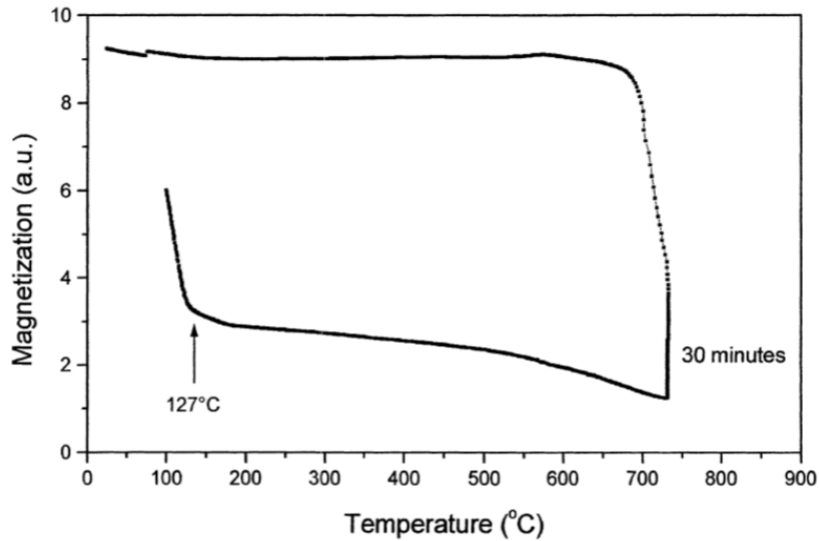
Figure 21 TMA curve up to 730 °C of the maraging 350 steel. The sample was kept for 30 min at 730 °C [24]

In 2004, Tavares et al., performed a magnetic study of maraging steel. A maraging 350 steel (19.8 %Ni, 10.7 %Co, 4.7 %Mo, 1.47 %Ti, 0.98 %Al, 0>0.007 %C, wt.%) was solution treated at 900°C. As would be expected, the microstructure was completely martensitic (b.c.c.). The samples were aged in the temperature range of 440–750 °C for 1 h. Some samples were cold rolled before aging.

The behavior of magnetization saturation and coercive field as a function of aging temperature are shown in Figures 22 a and 22 b. Saturation magnetization starts to decrease at about 560 °C and reaches a minimum value at 650 °C (Figure22 a). This attributes to the formation of austenite associated with precipitation reactions as suggested by Li and Yin [16] that the austenite results from the partial dissolution of $Ni_3(Mo, Ti)$ and Fe_2Mo formation. The Ni-rich austenite formed by aging in the 500–700 °C range is stable at room temperature. The austenite formation also promotes the increase of H_C (Figure 22 b). Cold rolling before aging does not change significantly the shape of the curves. The austenite formation between 560 °C and 700 °C promotes the increase of coercive force and the decrease of magnetization saturation. Thus for magnetic purposes, the steel may not be treated or used in this range.
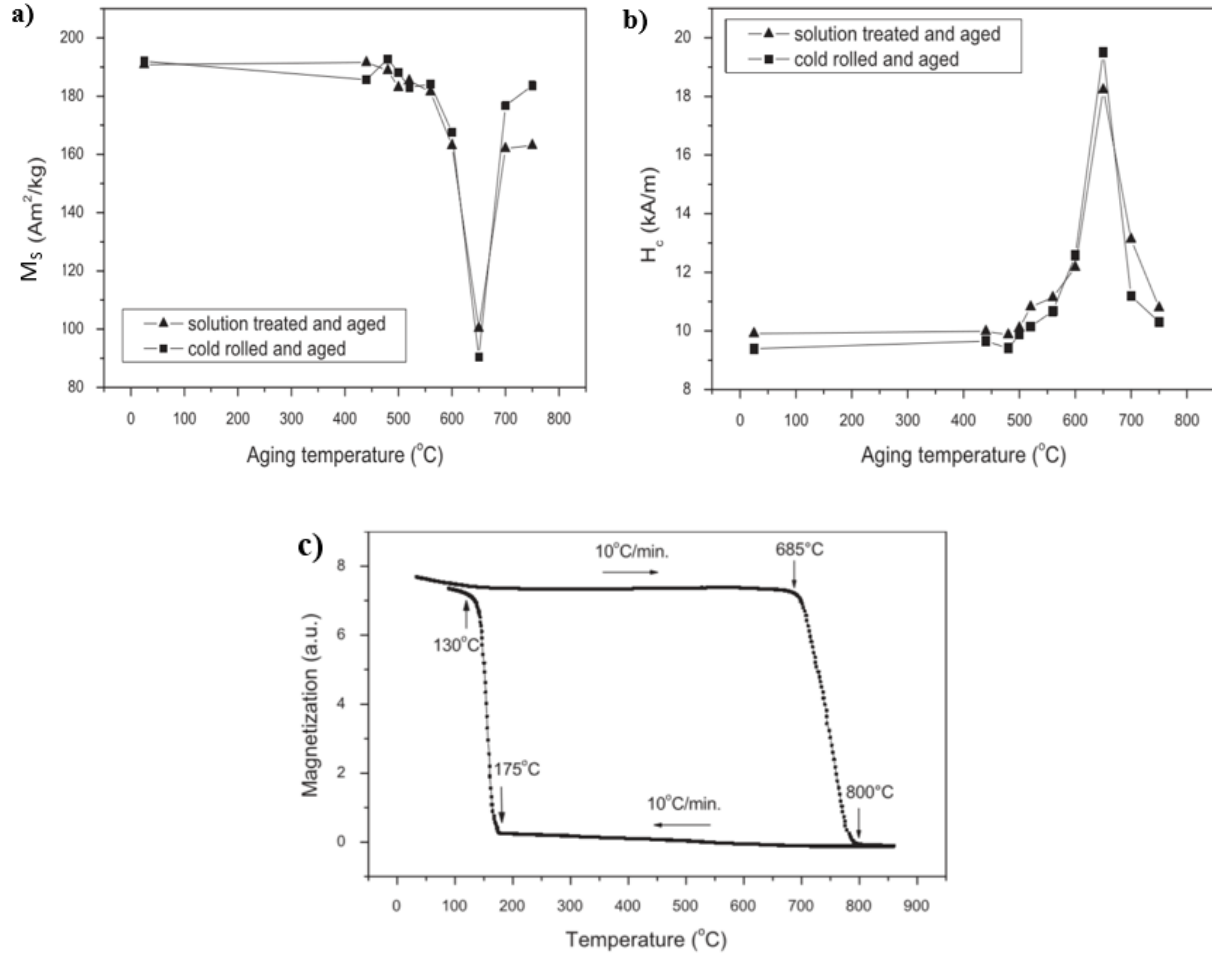
Figure 22 a) Saturation magnetization M_S (Am^2/kg), b) Coercive field H_C (kA/m) vs. aging temperature; c) Thermomagnetic analysis (TMA) of the maraging 350 steel [25]

The thermomagnetic analysis TMA curve obtained with heating and cooling rates at 10 °C/min is shown in Figure 22 c. The start(A_s) and final (A_f) temperatures of the martensite (α) to austenite (γ) transformation are 690 °C and 800 °C, respectively: the martensite start (M_s) and final (M_f) temperatures are 175 °C and 130 °C, respectively. Thus the thermomagnetic analysis may be used to determine the starting and final points of the α-γ and γ-α transformations.

In 2007, Tavares et al., the influence of temperature and aging time on the hardness and magnetic properties of the 300-grade maraging steel were studied. Sheet samples were chosen of dimensions (20 mm × 10 mm × 2.5 mm) of maraging 300 steel.

Samples were solution treated at 900 °C ± 10 °C for 40 min, followed by cold rolling. Some samples were made by solution treating followed with aging, and others were aged without solution treatment after deformation. The samples were aged at 440 °C, 480 °C, 510 °C, 560 °C, 600 °C, and 650 °C for different treatment times.

X-ray diffraction analysis was recorded, and the volume fraction of the austenite (γ) and martensite(α) phases were obtained by the direct comparison method, described by Cullity [36], and taking into account the different values in the scattering factors for austenite (γ) and martensite (α) phases for maraging, as steels suggested by Pardal et al. [11].
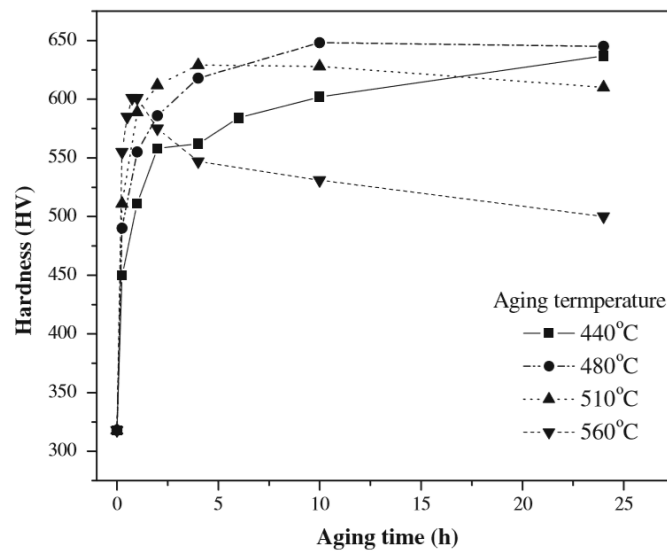
Figure 23 Hardness versus aging time at 440 ° C, 480 ° C, 510 °C, and 560 °C [25]

Hardness as a function of aging time shows the precipitation hardening curves of the maraging 300 steel aged at 440 °C, 480°C, 510°C, and 560 °C as shown in Figure 23. The precipitation hardening curves of 440 °C and 480 °C do not show over-aging until 24 h. While the samples aged at temperature 510 °C for different times presented a maximum peak hardness of 629 HV after 4 h of aging, and further aging times higher than 10 h produced a slight reduction in the hardness. In the case of aging at 560 °C, the hardness peak (601 HV) occurred at 1 h, and over-aging was observed after this time.

Aging at low temperatures (440 °C and 480 °C) showed that for short times the hardness increases slowly and continuously, in comparison with aging at higher temperatures. Thus, the

initial age hardening is due to the formation of S precipitates, that give place later to the ordered ω precipitate as reported by many types of research [12]. The aging at 510 °C the hardness peak is due to the precipitation of ellipsoidal Ni_3(Ti, Mo) at the dislocations clusters in the martensite matrix [12]. In the case of aging at 560 °C, this phenomenon occurs faster and the over-aging, mainly at 560 °C, is due to Fe_2Mo precipitation which maintains the hardness at a higher level for longer aging times [8]. Thus, one of the reasons for the hardness reduction, however, beyond the precipitates growth, is the partial dissolution of the Ni_3(Ti, Mo) intermetallic compound which gives place to the formation of the above mentioned Fe_2Mo and the nickel rich austenite [8].
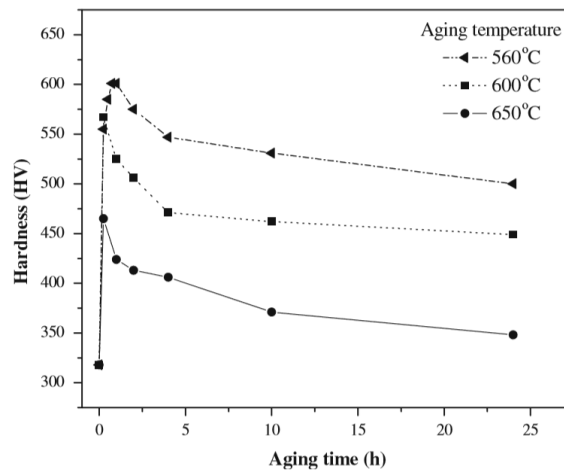
Figure 24 Hardness versus aging time at 560 °C, 600 °C, and 650 °C [25]
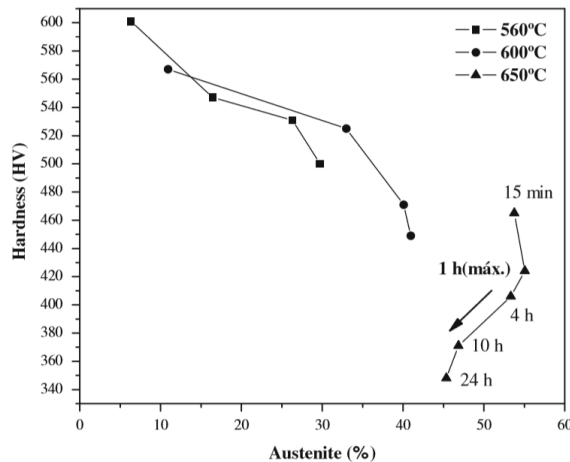
Figure 25 Hardness as function amount of precipitated austenite [25]

28

From Figure 24, for the samples treated at the 600 °C and 650 °C, the hardness peak occurs for 15 min of aging and presents values of 567 and 465 HV, respectively. So, when over-aged, the hardness decreases due to the austenite precipitation. Also, the growth, coalescence, and incoherence of the precipitates influence the drop of this property.

The influence of the austenite volumetric percentage on the hardness for 560 °C, 600 °C, and 650 °C in different aging times is shown in Figure 25. The increase of the precipitated austenite produced a substantial drop in the hardness for the aged samples at 560 °C and 600 °C in different time conditions due to the dissolution of intermetallic precipitates. The minimum hardness value is obtained in the sample aged 650 °C for 24 h. At 650°C, in contrast with 560 °C and 600 °C, the amount of austenite decreases with the increase of aging time after 1 h.
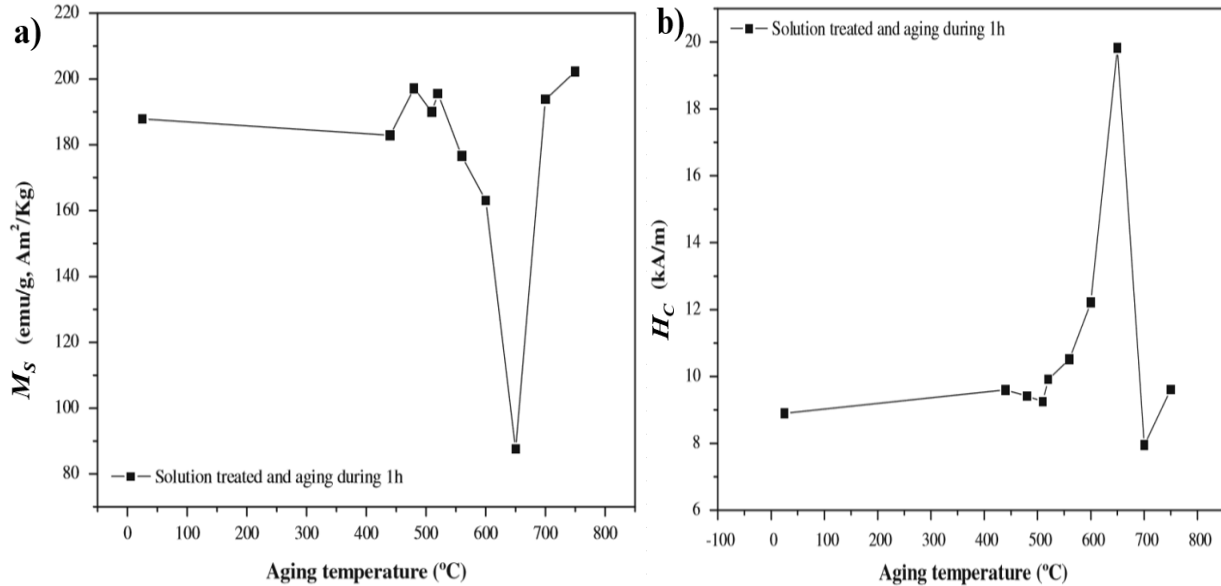
Figure 26 a) Saturation magnetization (M_S) and b) coercive force (H_C) as a function of aging temperature [25]

Magnetic characterization was carried out at room temperature using a vibrating sample magnetometer (VSM). The saturation magnetization and the coercive force of the solution treated samples aged for 1 h vary with the aging temperatures are shown in Figures 26 a and b, respectively. Aging between 560 °C and 700 °C produced extreme variations in the M_S and H_C values, which they attributed to the nickel rich reverted austenite formation. The minimum value

29

of M_S (88 A^{2}m/kg) and the maximum values of H_C (19.83 kA/m) were both obtained in the sample aged at 650 °C for 1 h.

The squareness ratio values (Br/Bs) as a function of the aging temperature, on the solution treated and aging samples during 1 h showed that in samples aged between 520 °C and 600 °C the squareness ratio values are higher than 0.8, which is characteristic in anisotropic materials for applications in electric motors.
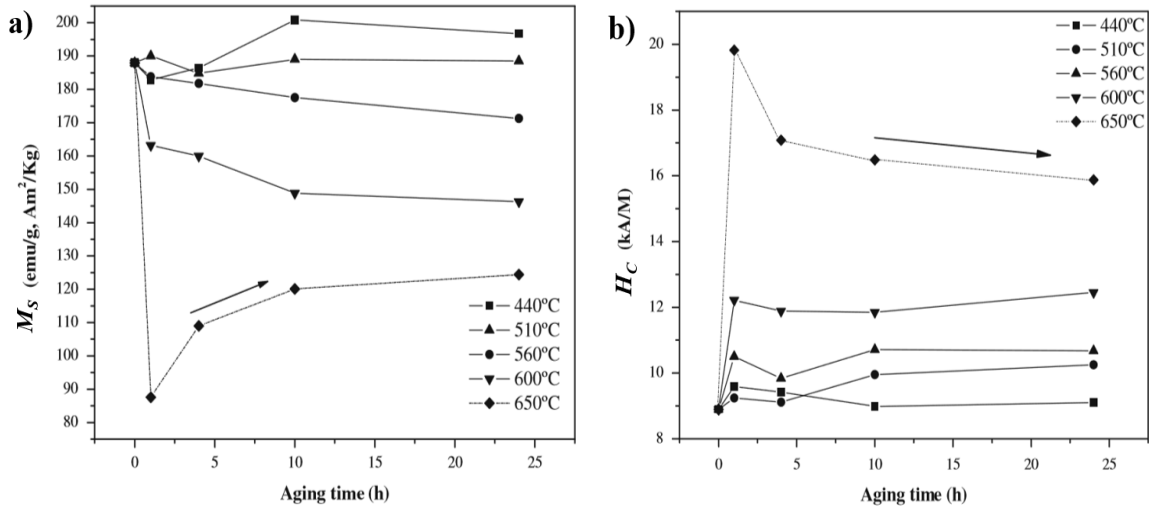
Figure 27 a) Saturation magnetization (M_S) and b) coercive force (H_C) versus aging time [25]
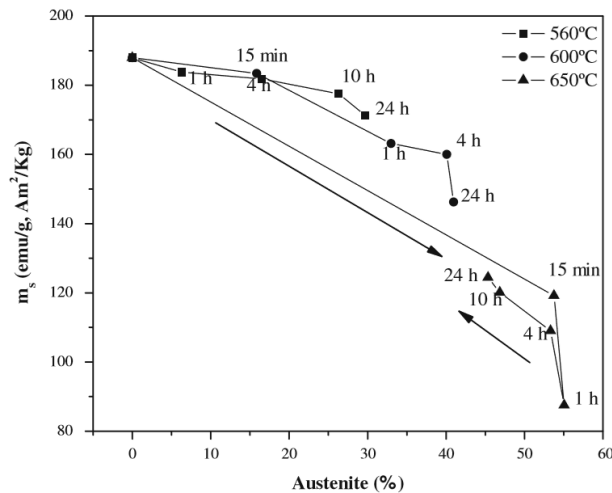
Figure 28 Saturation magnetization (M_S) versus austenitic volumetric percentage at 560 °C, 600 °C, and 650 °C [25]

The behavior of saturation magnetization (M_S) and coercive force (H_C) against the aging time are shown in Figures 27 a and b. A small effect of magnetic hardening (increase of the H_C) force occurred only after at 510 °C. Therefore, the mechanical hardening effect is more critical than the magnetic hardening at temperatures less than 510 °C. Aging at 560 °C, the increase of the austenite content above 560 °C promotes the decrease of the saturation magnetization (M_S) and hardness, concomitant with the decrease of coercive force (H_C). Increasing the aging time at 560 °C and 600 °C also raises H_C and makes ms falls. On the other hand, from Figure 28, at 650 °C, the increase of aging time promotes the decrease of the austenite content, which induces the increase of M_S and the decrease of H_C.

Aging at 560 °C for 1h allows high mechanical resistance and good magnetic properties (*Br/Bs*, H_C, and M_S) in the maraging steel 300. Finally, they fitted a square equation(1) to obtain a correlation between the M_S and the amount of austenite and suggested that this correlation can be used to obtain an estimative of the austenite volume fraction in maraging steels.

$$\gamma = -0.00672 \, M_S{}^2 + 1.426 \, M_S - 22.097 \tag{1}$$

In 2015, H.F.G. Abreu et al., examined the influence of the cooling rate on the phase fraction of the reverted austenite and how the mechanical properties, coercive force, and magnetization saturation were affected.

Maraging 350 steel cold-rolled samples were solution annealed at 870 °C for 1 h and then air cooled. In sequence, the samples were aged at temperatures ranging from 450 °C to 650 °C for 1 h.

Aging treatments above 550 °C promote the reversion of austenite in maraging steels. The phase fraction of the formed austenite can be totally or partially retained at room temperature after cooling, depending on the chemical composition. The Ni content plays a significant role in the stability of the austenitic phase as a result of the dissolution of precipitates formed in Ni-rich regions, and the reversion of austenite results in a γ phase richer in Ni and an α phase weaker in Ni. The composition variations of the austenite phase with temperature are shown in Table 6. The M_s was calculated using equation(2) from the past work[53], which is more specific for maraging grade alloys.

31

Table 6 Calculated composition of reverted austenite at different aging temperatures [52]

Aging temperature(°C)	Fe (wt.%)	Co (wt.%)	Ti (wt.%)	Ni (wt%)	Mo (wt.%)	M_s temperature(°C)
550	59.0	5.6	0.25	31.4	3.5	-28.3
600	62.0	7.5	0.5	25.7	4.3	57.1
650	63.3	10.0	1.0	20.6	4.8	122.5
700	63.4	10.7	1.4	19.7	4.8	124

According to the calculations, Ni content necessary to stabilize austenite decreases with an increase in temperature, reaching the nominal composition of the alloy at 700 °C. Also for the aging temperature of 550 °C, the calculated M_s temperature falls below -40 °C, stating that with cooling in liquid nitrogen after 1 h aging, there will be no stable reverted austenite at room temperature. This confirmed the assumption to be correct from the Figure 29, which compares the XRD patterns for samples aged for 1 h at 550 °C followed by air and liquid nitrogen cooling. The sample cooled in air showed peaks of austenite different from the sample cooled in liquid nitrogen where only martensite peaks are present.

M_S (°C)= 549 - 500 C+15.9 Al – 3.8 Co – 18.3 Cr – 6 Cu – 22 Mn + 0.2 Mo – 1.6 Nb – 17.5 Ni – 10 Si – 29 Ti – 54 V　　　　　　　　　　　　　　　　　　　　　　　　　　　(2)
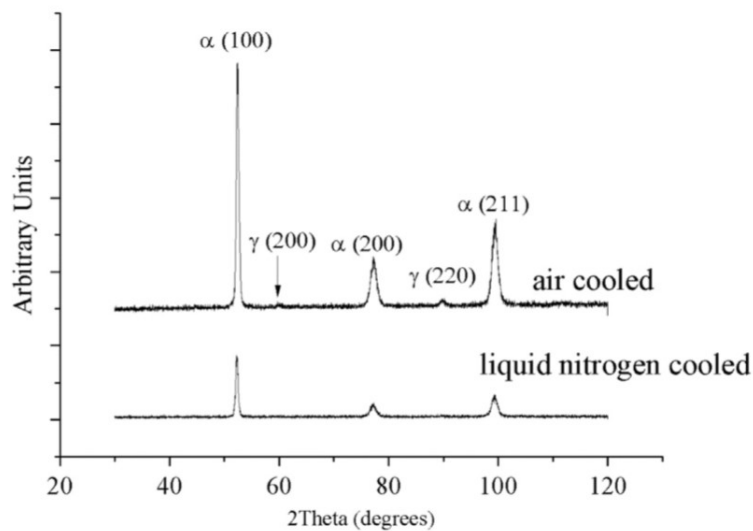
Figure 29 XRD patterns of the sample aged at 550 °C for 1 h followed by air and liquid nitrogen cooling [52]

The volume phase fraction of reverted austenite, for the 90% cold-rolled samples aged at 450 °C to 650 °C and cooled in air and liquid nitrogen, as shown in Figure 30. For samples aged at temperatures above 550 °C, a lower phase fraction of reverted austenite is observed when the sample is cooled in liquid nitrogen as compared to air.
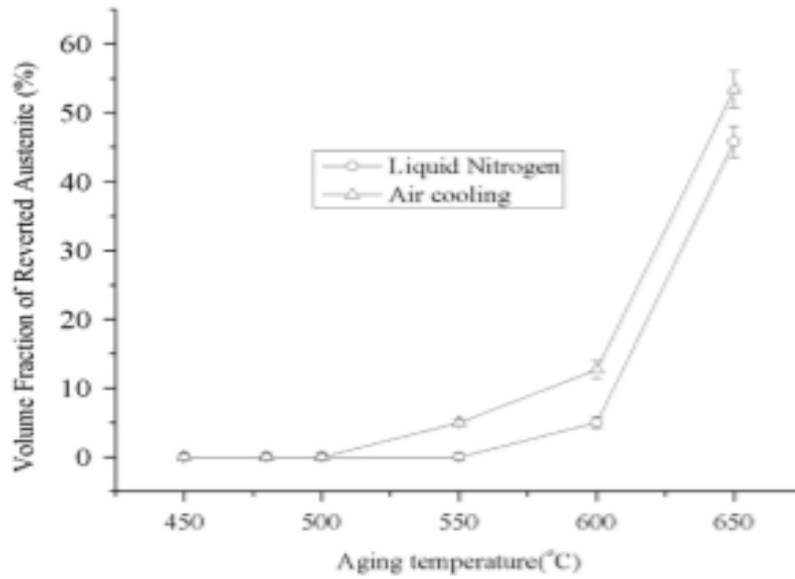
Figure 30 Quantification of the austenitic phase by XRD for samples cold rolled to 90% thickness, aged for 1 h and cooled in air and liquid nitrogen [52]
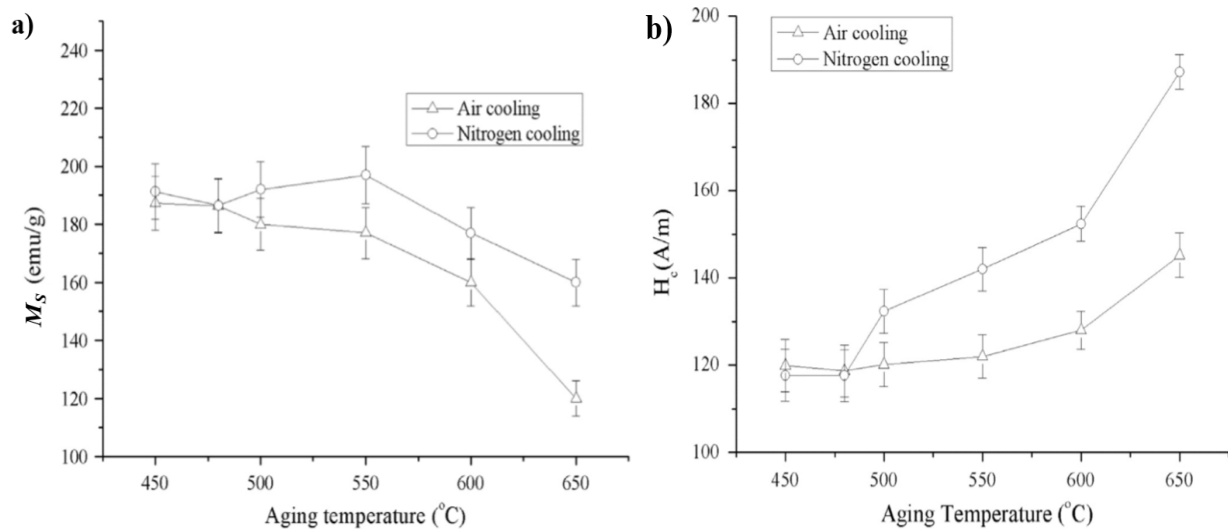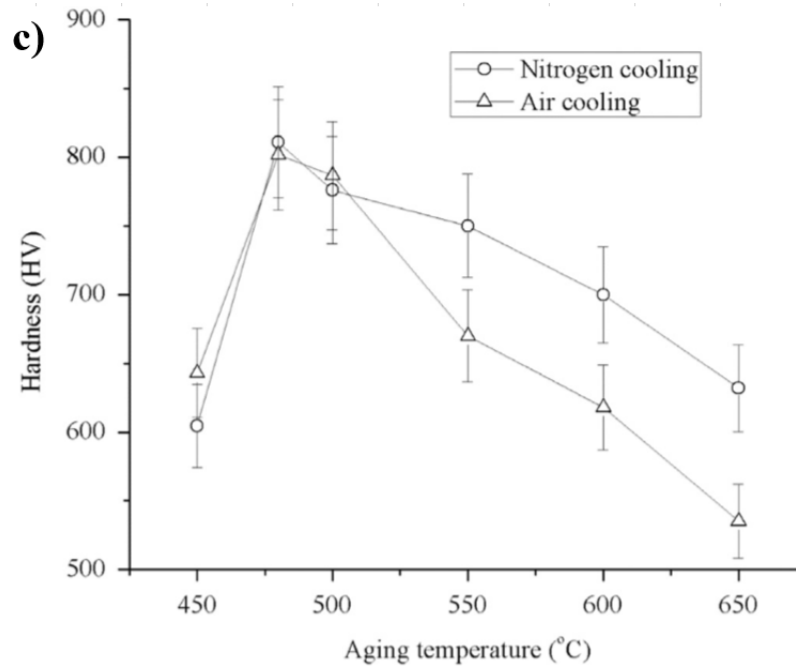
Figure 31 a) Saturation magnetization, b) Coercive force, and c) hardness for samples cooled in air and liquid nitrogen [52]

Saturation magnetization, Coercive force, and hardness for samples cooled in air and liquid nitrogen against the aging temperature show the effect of the presence of reverted austenite on both magnetic and mechanical properties as shown in Figure 31. The saturation magnetization(M_S) decreased with increasing aging temperatures, as shown in Figure 31 a. This effect is more pronounced in samples cooled in the air where the fraction of reverted austenite is higher. The coercive force (H_C) is also affected by the fraction of reverted austenite, resulted in smaller H_C when cooled in liquid nitrogen, as shown in Figure 31 b. Hardness (HV) was found to be affected by the fraction of reverted austenite. Samples cooled in liquid nitrogen had a smaller decrease in hardness with increasing aging temperature when compared with samples cooled in the air (Figure 31 c).

Finally, the Ni content necessary to stabilize austenite decreases with an increase in aging temperature, thus affecting the M_s temperature, and consequently, the phase fraction of reverted austenite when a sample is aged and cooled in liquid nitrogen. Cooling samples in liquid nitrogen after aging above 550 °C reduces the phase fraction of reverted austenite and increases

magnetization. The presence of retained austenite simultaneously increases the coercive force and decreases the saturation magnetization and mechanical hardness.

2.4 Mechanical milling

Mechanical milling (MM) is a simple and in-expensive processing technique to achieve equilibrium and metastable phases. This technique has been known as a 'mechanochemical synthesis' technique, 'solid-state processing' technique, 'far from equilibrium' or a 'Non-equilibrium' synthesis technique because of the way it functions. Milling uniform (often stoichiometric) composition powders, such as pure metals, intermetallics, or pre-alloyed powders, where a material transfer is not required for homogenization. MM has an advantage over mechanical alloying (MA) since the powders are already alloyed and only a reduction in particle size and/or other transformations need to be induced mechanically, the time required for processing is short.

The central underlying theme is to synthesize materials in a non-equilibrium state by "energizing and quenching." The energization involves bringing the material into a highly non-equilibrium (metastable) state by some external dynamical forcing (through storing of mechanical energy by plastic deformation). During high-energy milling the powder particles undergo continual deformation as they are repeatedly flattened, cold welded, fractured and rewelded. This deformation is carried out by extremely energetic collisions of grinding media (balls) moving with high kinetic energy and the powders with themselves and the inner walls of the vial.

2.5 Mechanism of mechanical milling

A blend of pre-alloyed powders is taken into a suitable vial. A suitable grinding media, mostly steel balls, are used to provide the required energy transfer. A small amount of the powder is trapped between the balls during a collision, as shown in Figure 32. The force of the impact plastically deforms the powder particles leading to work hardening and fracture. The new surfaces created to enable the particles to weld together, and this leads to an increase in particle size. Since in the early stages of milling, the particles are soft (if we are using either ductile-ductile or a ductile-brittle material combination), their tendency to weld together and form large particles is high. A broad range of particle sizes develops, with some as large as three times that of the starting

particles. In the initial stages, the tendency to fracture predominates over cold welding. The process schematic is shown in Figures 32.
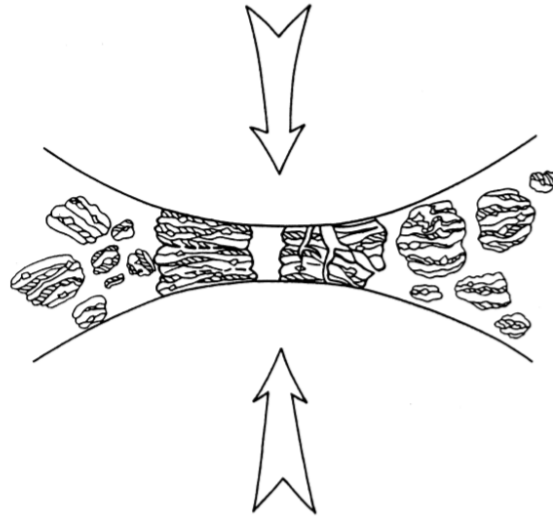
Figure 32 Sample trapped during Ball-powder-ball collision of powder mixture during mechanical milling [31]

Milling is continued still steady-state equilibrium is attained, i.e., when a balance is achieved between the rate of welding and fracturing., which tends to increase the average particle size, and the rate of fracturing. Some chances of excessive cold-welding can be observed during the milling process. Due to this excessive cold-welding, the smaller particles agglomerate and form into bigger particles. This can be reduced using a process control agent (PCA). The obtained powder is subjected to heat treatment if necessary, to obtain a required compound with desired microstructure and properties.

2.6 Processing variables in mechanical milling

There are several process variables involved in the MM process and also which are also not completely independent. Thus to achieve the desired product phase and microstructure optimization of these variables is critical. Some of the critical parameters that affect the final product of the powder are:

1. Type of Mill

2. Milling Container

3. Milling Speed

4. Milling Time

5. Type, Size and size distribution of grinding medium

6. Ball to powder ratio

7. The extent to filling the vial

8. Milling atmosphere

9. Process control agent

10. Temperature of Milling

Examples of some of these parameters being dependent are, as the Milling speed is mostly specific to the type of mill. Also, the optimum milling time depends on the type of mill, the ball to powder ratio, type, size, and size distribution of grinding medium, and the extent to filling the vial. It also depends on the type, and the amount of process control agent used.

2.6.1 Type of mill

For the processing of materials to produce mechanically milled samples, different types of high energy milling equipment are used. Planetary ball mills, Attritor mills, SPEX shaker mills, and some commercial mills are the different types of mills being used. These mills differ by their capacity, efficiency, and structure. There are recent developments in the different types of grinding media (vials and the balls) of these mills that could be used for the processing of different materials.

In all these milling processes, the of uniforms (often stoichiometric) composition powders, such as pure metals, intermetallics, or pre-alloyed powders are subjected to high energy collisions from the balls when the vials are rotated or shaken with high kinetic energy.

Out of these mills, SPEX shaker mills are most commonly used for laboratory purposes. A typical example of such a shaker mill is SPEX 8000 is shown in Figure 33. The capacity of this mill is about 10-20 g of the powder at a time (unlikely the capacity of the planetary mill is about 100-250 g). Initially, one vial was used for the milling process. Later after further developments,

two vials are being simultaneously milled to improve the throughput. After adding the charge (powder) into the vial along with the grinding media (balls), the vials are clamped and swung energetically back and forth several thousand times a minute. This back-and-forth shaking motion of the vials appears to be an infinity sign ∞ as it moves. During this motion of the vials, the balls impact with each other and with the walls of the vial at very high velocities having some amount of powder trapped between them. The force of the impact plastically deforms the powder particles leading to work hardening and fracture. A variety of vial materials is available for the SPEX mills, and these include hardened steel, alumina, tungsten carbide, zirconia, stainless steel, silicon nitride, agate, plastic, and methacrylate.

Figure 33 SPEX 8000 mixer/mill [31]

2.6.2 Milling container

Type of milling container used plays a vital role in the mechanical milling process. It is essential because it undergoes high impact collisions between its walls and the balls. All the energy transfer is carried inside the container. During the milling process, due to these high impact collisions of grinding medium on the inner walls of the container dislodges some material of the container and will be and get incorporated into the powder. This can contaminate the powder or alter the stoichiometry of the powder. In case, if the material of the milling container is different from that of the powder, then the powder may be contaminated with the milling container material. On the other hand, if the materials are the same, then the stoichiometry may be altered in the final product unless proper precautions are taken to compensate for the additional amount of the

elements incorporated into the powder. Different types of milling containers are used based on the interest of materials to be processed. Hardened steel, tool steel, hardened chromium steel, tempered steel, stainless steel, WC-Co, WC-lined steel, and bearing steel are the most common types of materials used for the milling containers. Also, there are some specific milling container materials like copper, titanium, sintered corundum, yttria-stabilized zirconia (YSZ), partially stabilized zirconia + yttria, sapphire, agate, hard porcelain, Si_3N_4, and Cu-Be that have been used where it was observed that those materials wouldn't react with the powders or where it was acceptable to have a little to no contamination [31].

2.6.3 Milling speed

Milling speed plays a crucial role in the mechanical milling process. It is easy to realize that the faster the mill rotates, the higher would be the energy input into the powder. Milling speed depending on the design of the mill has certain limitations. Above a critical speed; the balls get pinned to the inner walls of the vial, hence reducing energy transfer to powders (reducing the effectiveness of the mechanical milling process drastically). The temperature of the vial is another limitation to the maximum speed as it may reach a high value. This may be advantageous in some cases where diffusion is required to promote homogenization in the powders. While, in some cases, the increase in temperature may contaminate the powders. Also, during the nanocrystal formation, the average crystal size increases, and the internal strain decreases at higher milling intensities—due to the enhanced dynamical recrystallization. Therefore, the maximum speed should be just below this critical speed to have an effective milling process.

2.6.4 Milling time

The time chosen for the milling of powder particles is looking for the charge in the milling to achieve a steady state, i.e., achieving a balance between the fracturing and cold-welding. Milling time is a dependent factor on the other processing variables in the mechanical milling process. One example is that, if the ball to powder ratio is high, then the time required to reach a steady state is low when compared to a lower ball to powder ratio used. The time should be decided for each combination of the processing variables and the particular powder system. Milling for a higher duration results increase in the level of contamination and also some undesirable phases can be formed. Therefore, it is desirable that the powder is milled just for the required duration and not any longer.

2.6.5 Type, size and size distribution of grinding medium

Many different types of materials have been used for grinding medium like Hardened steel, stainless steel, tool steel tempered steel, hardened chromium steel WC-Co and bearing steel. It is desirable to use grinding media of the same material as the powders being milled or alloyed to avoid cross-contamination[31]. The size of the balls/grinding media has a massive impact on how effective the milling is in a given time. Bigger balls certainly have higher impact resulting in faster milling as the energy transfer in each impact is very high. On the other hand, when using small balls, several balls to be used are more to attain a particular ball to powder ratio, and this means a higher number of impacts but with significantly lower impact energy. It was observed that amorphous phases formed when using smaller balls as they produce intense frictional action, whereas when using bigger balls, more stable and crystalline compounds were obtained. Even though in most cases, only one size of balls/grinding media are used, there were some instances where different sized balls have been used together[31]. Previous reports stated that using a combination of large and small balls for milling reduces the amount of cold welding[31]. Also when using a set of same-sized balls in the vial, they tend to produce tracks which indicates that the motion is not random and they move along a defined trajectory whereas when using a mixture of balls of different sizes, it was noticed that the motion was random[31].

2.6.6 Ball to powder ratio

Ball to powder ratio (BPR) is the ratio of the mass of balls to the mass of the powder chosen for milling, which is also sometimes referred to as charge ratio (CR). BPR is an essential variable in the milling process. Generally, speaking, a BPR of 10:1 is most commonly used while milling the powder in research laboratories or a small capacity mill such as a SPEX mill. In the past, this BPR has been varied by different investigators from a value as low as 1:1 to as high as 220:1. Generally speaking, a ratio of 10:1 is most commonly used while milling the powder in a small capacity mill such as a SPEX mill. However, when milling is conducted in a large capacity mill, like an attritor, a higher BPR of up to 50:1 or even 100:1 is used.

The BPR has a significant effect on the time required to achieve a particular phase in the powder being milled. As mentioned earlier, higher the BPR lower the milling time and vice versa.

It was observed in the literature that for the formation of an amorphous phase in a Ti-33at%Al powder mixture milled in a SPEX mill took 7 h at a BPR of 10:1, 2 h at a BPR of 50:1 and 1 h at a BPR of 100:1 [31]. At a high BPR, because of an increase in the weight proportion of the balls, the number of collisions per unit time increases and consequently more energy is transferred to the powder particles, and so milling takes place faster. It is also possible that due to the higher energy, more heat is generated and this could also change the constitution of the powder.

2.6.7 The extent of filling the vial

In the mechanical milling, the milling is performed by the exerting high impact forces of the balls, milling container and the powder stuck between them. Thus to have effective milling, it is necessary that there is enough space for the balls and the powder particles to move around freely in the milling container. The longer the ball travels, the more impact energy it supplies, and thus, each impact is highly effective. Filling the vial space for more than 50 % would lead to a significant decrease in energy being supplied to powders, thus taking a long time to obtain the required phases [31]. If a small amount is taken such that greater than 70% of the vial is left empty, the production rate would be relatively low. Hence the extent to which the vial is being filled must be considered carefully to have an active process.

2.6.8 Milling atmosphere

Milling atmosphere plays a vital role in the contamination of the milling powders. Most material/metals, although not very reactive in solid form, are highly reactive when they are ground to a powder form; ex: Mn. Typically, the loading and unloading of the powders into the vial is carried out inside an atmosphere-controlled glove box. These glove boxes are usually repeatedly evacuated and refilled with the argon gas. While in the case, when the loading and unloading of the powders of the milling process in the atmosphere, there are some chances of the amount of oxygen present in the vial, could lead to the formation of oxides and thus results in the contamination. Thus proper care should be taken while loading and unloading the powders in the milling process.

Different atmospheres have been used during milling for specific purposes. Nitrogen or ammonia atmospheres have been used to produce nitrides [31]. Hydrogen atmosphere was used to produce hydrides [31]. The presence of air in the vial has been shown to produce oxides and

nitrides in the powder, especially if the powders are reactive. Thus, care should also be taken to use an inert atmosphere during milling. Also, from the previous results from the past, it was concluded that the type of atmosphere also seems to affect the nature of the final phase.

2.6.9 Process control agents

During mechanical milling, the powder particles get excessively cold-welded to each other, due to the substantial plastic deformation experienced because of repeated cold welding and fracturing; and the balance between these two is necessary for the milling/alloying to be effective. This is most commonly observed when the powder is ductile. This affects the milling in reaching a steady state, i.e., the balance between the welding and fracturing. To reduce/prevent this excessive cold welding, a process control agent (PCA)(also called as a surfactant or a lubricant) is added to the powder particles during the milling. These PCA's can be in solid, liquid, or gaseous form. Most of the PCA's are organic compounds which act as surface-active agents [31]. The PCA used adsorbs on the surface of the powder particles and minimizes cold welding between powder particles and thereby inhibits agglomeration. Typically, a range between 1-5 wt% PCA of the total powder charge (mass of the powder excluding the mass of balls) is used in practice.

Different types of PCA's such as ethanol, methanol, hexane, Oxalic acid, Benzene, ethyl acetate, Heptane, polyethylene glycol, naphthalene, cyclopentane, Toluene, and stearic acid have been used depending on the level and type of contamination they would induce and also their effectiveness on milling process [31]. It was found that the nature and quantity of the PCA used and the powder milled would determine the final size, shape, and purity of the powder particles. Increasing the amount of PCA helps reduce the particle size exponentially for a given milling time [31].   One way of determining the effectiveness of the PCA is to determine the powder yield after mechanical milling. If the powder yield is high, the PCA is useful. If the powder yield is not high, then either the amount of PCA used is not sufficient, or probably it is not the right PCA for those materials.

2.6.10 Temperature of milling

The temperature of milling is another important parameter in deciding the constitution of the milled powder. It directly affects the final composition of the powders milled. In the formation of alloys phases, diffusion process occurs irrespective of whether the final phase is a solid solution,

intermetallic, nanostructure, or an amorphous phase and temperature of milling has a significant effect in this process.

There have been few investigations where the temperature of the milling was varied intentionally. They were performed to study the effect of temperature of milling on solid solubility levels and the formation of either amorphous or crystalline phases at different temperatures. To mill at lower temperatures, the milling vial was dripped on with liquid nitrogen and to obtain higher temperatures, the vial heated electrically.

2.7 Contaminations in mechanical milling

Several factors are leading to contamination in this synthesis process, of which major contamination was observed to be from three different sources which are explained below.

2.7.1 Contamination from milling tools

One of the most common contaminations in mechanically milled powders is Fe and Cr elements from the milling vial and balls since most milling tools are made from those types of elements. During mechanical milling, the balls impact onto the powder mixture, the vial as well as onto each other. The powder particles are, therefore, not only cold-weld with powder particles themselves but also with the milling tools under high energy collision. The cold-welded powder will sooner or later be fractured from the balls and the vial by direct collision and relative friction, leading to transfer of atoms from the milling tool to the powder particles. It appears that contamination from milling tool is unavoidable, especially at high impact intensity and long milling duration. It is a serious problem in mechanical milling, and several methods have been suggested to reduce this sort of contamination:

a. Using hardened milling tools.

b. Employ milling tools with similar composition as the powder mixture so that the contamination will have the same composition as the milled materials.

c. Increase cold welding so that the milling tools may be covered with the powder mixture.

2.7.2 Contamination from atmosphere

When the loading and the unloading are performed in the atmosphere, there are chances of formation of oxide contamination. Even when inert gases such as argon, nitrogen, and helium are employed to prevent oxidation, they may themselves react with the powder mixtures being mechanically alloyed. Depending on different material systems, sometimes this reaction can be severe.
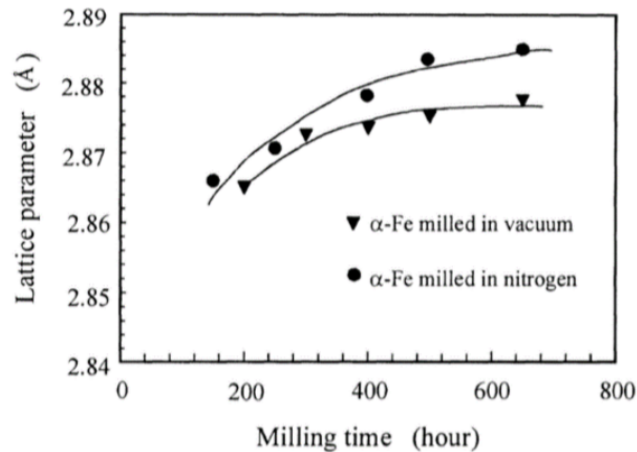
Figure 34 Influence of vacuum and nitrogen environments on the change in average lattice parameter of Fe [33]

The figure above shows the average lattice parameter of Fe powder ball milled under two milling environments, namely, vacuum and nitrogen protection [33]. The lattice parameters change under both conditions: there is a large increment when the Fe powder is milled in a nitrogen atmosphere, but only a little increase in the latter case. About 0.8% increase in lattice parameter in the former case is attributed to the absorption of nitrogen and a corresponding expansion of the lattice. In the latter case, the lack of gases leads to a slower increase in lattice expansion; about 0.4% increase in lattice parameter is associated with the residual gases. For materials that will readily form nitrides, the use of nitrogen to provide an inert atmosphere should be avoided. Research shows that nitrides may be formed if Ti, Ta, Zr, Mo, and Si are milled in a molecular nitrogen atmosphere.

2.7.3 Contamination from process control agents

Decomposition of process control agents during mechanical milling cannot be avoided. As these process control agents normally contain carbon, oxygen, and hydrogen, their decomposition may cause carbon, oxygen, and hydrogen contamination. Use of stearic acid has been found to give contamination of 1.1wt.% carbon and 0.8wt.% oxygen [33]. Direct formation of hydride in mechanical alloying of Al-Zr has also been reported [33], indicating the decomposition of the process control agent. It has been explained that the process control agent decomposes into hydrogen, oxygen, and carbon due to rise in temperature in the mechanical alloying/milling process. Repeated cold welding and fracturing result in the formation of very fine powder particles (sub-micron size). Because of large surface area to volume fraction, the surface energy of the mechanically milled powder particles increases with the increase in milling duration. The new surface created by the fracturing process promotes diffusion. In comparison to oxygen and carbon, the diffusion rate of hydrogen is much faster than that of oxygen [33]. The table below gives the amount of H_2, O_2, and C contents of different types of the process control agent.

Table 7 Amount of H_2, O_2 and C percentage in each process control agent which could lead to contamination [33]

Generic name	Chemical formula	H_2 (%)	O_2 (%)	C (%)
Stearic acid	$CH_3(CH_2)_{16}CO_2H$	13	11	76
Heptane	$CH_3(CH_2)_5CH_3$	16	0	84
Ethyl acetate	$CCH_3CO_2C_2H_5$	9	36	55
Ethylenebidisteramide	$C_2H_{2-2}(C_{18}H_{36}ON)$	13	5	77
Dodecane	$CH_3(CH2)_{10}CH_3$	15	0	85
Hexanes	C_6H_{14}	16	0	84
Methyl alcohol	CH_3OH	13	50	37
Ethyl alcohol	C_2H_5OH	13	35	52

The degree to which the H_2, O_2, or C gets absorbed into the material being synthesized depends upon the materials that are being milled.

CHAPTER 3: MOTIVATION

Maraging steels have a superior combination of magnetic and mechanical properties and are used in a wide range of applications [1-7,22-27]. With the growing interests towards additive manufacturing, it is imperative to investigate the structural, mechanical, and magnetic properties of the steel in the powder form and also its thermal stability. There are several gaps in the study of magnetic properties of the maraging steel powder. Few gaps in the literature that piqued the interest are as follows: Firstly, the commercially available gas-atomized powder has not been characterized for magnetic properties. It is essential to characterize the magnetic properties as well as their thermal stability. Secondly, the effect of mechanical milling the pre-alloyed gas-atomized powder, i.e., phase evolution and associated changes in the structural and magnetic properties during mechanical milling (at ambient temperature and pressure) of the commercially available powder, coupled with the thermal effect on their magnetic properties.

CHAPTER 4: EXPERIMENTAL PROCEDURE

4.1 Materials synthesis

The pre-alloyed maraging steel powder, produced using inert gas atomization technique, was procured from EOS of North America, Inc., which is shown in Figure 35. As per the mill test certificate/data sheet provided by the manufacturer—EOS Finland, the composition of the as-received pre-alloyed maraging steel powder is shown in Table 8. Its composition corresponds to atypical 18 wt.% Ni (300) maraging steel [6-7]. The mill test certificate/data sheet provides the manufacturer particle size D_{90}, D_{50} and D_{10} were ~51μm, ~32μm and ~18μm respectively (based on the particle size analyses by laser diffraction technique—ISO 13320).

Figure 35 The as-received, pre-alloyed gas-atomized maraging steel powder

Table 8 Chemical composition of the as-received pre-alloyed maraging steel powder

ELEMENT	COMPOSITION (wt.%)
Nickel	18.5
Cobalt	8.7
Molybdenum	4.9
Titanium	0.7
Aluminum	0.1
Chromium	0.1
Manganese	0.07
Copper	0.03
Silicon	0.02
Carbon	0.01
Sulfur	0.01
Phosphorous	<0.01
Iron	Balance

Structural and magnetic characterization of the procured pre-alloyed gas atomized powder was performed. In order to investigate the phase evolution in the procured maraging steel powder, it was set for mechanical milling. Milling was carried out in a high energy ball mill (SPEX SamplePrep 8000 Dual mill), as shown in Figure 36. Hardened steel vial and hardened steel balls (SPEX 8001) are shown in Figure 37 were chosen as grinding/milling media. The ball-to-powder ratio adopted during the milling was 8:1. Stearic acid—$CH_3(CH_2)_{16}COOH$— was used as a process control agent (PCA) for the milling process to reduce the effect of cold welding. The powder along with the balls was loaded into a hardened steel vial, filling about 20 to 30 % of the vial space; leaving ~70 % or space for the mechanical milling process to be effective. All the material handling—loading sealing, and unloading of the powder particles, along with the balls and PCA, into the vial, were performed at ambient temperature and pressure conditions.

Figure 36 SPEX SamplePrep 8000 dual high energy ball mill

Figure 37 SPEX 8001 hardened steel vial used for the milling

Mechanical milling was performed as a cycle of 3 h of milling and an interval of ~ 30 minutes as rest for the mill motor to prevent the damage due to excessive heating. The temperature of the vial was recorded at the start, at every 3 hours of continuous milling, and the end of milling. The milling was stopped at certain interest hours of milling and also when the milling ceased due to excessive cold welding. In each case, the vial was removed and was set for overnight cool-down by placing the vial on an Al-block. The vial was opened and carefully observed whether there are any fumes turn up when exposed to ambient air. The walls of the vials are scraped to remove the powder stuck to the walls of the vial and the balls. A small amount of sample was removed from

the vial and stored in glass vials as a representative of the hours of milling and stored in a desiccator. The milling was further continued with the remaining sample in the vial. PCA of 3 wt.% was added intermediately to the remaining sample only when the milling stopped due to excessive cold welding.

4.2 Materials characterization

4.2.1 Structural characterization

The pre-alloyed gas-atomized powder (S0) and the milled powders (3h, 5h, 8h, 14h, 20h, 23h, 35h, 47h, and 56h) before and after the thermal treatment were analyzed using a Rigaku miniflex 600 diffractometer (Rigaku Americas Corporation, The Woodlands, Texas, US) to identify the phases present and the phase-evolution with milling (as shown in figure 38). The source of x-ray was Cu $K\alpha$ radiation (with wavelengths of $K_{\alpha1}$~ 0.15406 nm and $K_{\alpha2}$~ 0.15444 nm) at a voltage and current of 40 kV and 15 mA respectively, and a Ni filter is used to filter the K_β radiation. The (θ-2θ) scans were recorded between the 2θ angles of 20°- 100° with a step size of 0.02°. The phases were identified by using the direct comparison method with similar compositions from the literature. The $2\theta_{(hkl)}$ of the planes having miller indices h, k, and l was obtained by fitting the corresponding diffraction peaks with a pseudo-voigt function in Origin Pro 2018. The positions of the peaks in an x-ray diffraction pattern depend on the crystal structure (more specifically, the shape and size of the unit cell) of the material and this helped to determine the structure and lattice parameter.

Figure 38 Rigaku miniflex powder X-ray diffractometer

In a cubic system, the lattice parameter $a_{(hkl)}$ for the diffraction from (h, k, l) corresponding to the diffraction (Bragg) angle is expressed as follows.

$$a_{(hkl)} = (h^2+k^2+l^2)^{1/2}(\lambda/2 \sin\theta_{(hkl)}) \tag{3}$$

Where λ is the wavelength of the x-ray diffraction (nm). The precise lattice parameter (a) of the phase was estimated by plotting the value $a_{(hkl)}$ calculated from each reflection (Bragg angle $\theta_{(hkl)}$) of the phase against the function $(\cos^2\theta_{(hkl)})/(\sin\theta_{(hkl)})$. By extrapolating to a value corresponding to $\theta=90°$ precise lattice parameter (a) was estimated [37-39].

The grain size (crystallite size) and the lattice strain induced in the powders can be estimated from the broadening of the x-ray diffraction peaks. Broadening of x-ray diffraction peaks arises mainly due to three factors: instrumental effects (B_i), grain size (B_c), and lattice strain (B_s) They can be estimated using the Williamson-Hall method. The instrumental width (B_i) is the full-width half maxima(FWHM) of a standard LaB_6 sample which was used for the calibration, provided by Rigaku. To determine the remanent width (B_r) i.e., due to the combined effects of crystallite size (B_c) and lattice strain (B_s), the instrumental peak width (B_i) is to be canceled out from the observed x-ray peak width (B_o) and is expressed as[38-39]:

$$B_r = \sqrt{(B_o - B_i)\sqrt{(B_o{}^2 - B_i{}^2)}} \qquad (4)$$

$$B_r cos\theta = k\lambda/L + \eta\, sin\theta \qquad (5)$$

Equation(3) also shows the combined effect of grain size and lattice strain, where k is the shape factor, a constant-generally approximated as ~1, λ is the wavelength of the x-ray radiation, L is the crystallite size, and η is the lattice strain. By plotting graph between $B_r cos\theta$ and $sin\theta$, the lattice strain and crystallite size were calculated.

Scanning electron microscopy/Energy disperse x-ray spectroscopy (SEM/EDS) was performed to capture the micrographs and to obtain the chemical composition of the powder by using a JOEL IT500 Scanning electron microscope as shown in figure 39 (SEM) at an accelerating voltage15 kV and in a secondary electron mode, in order to observe the morphology of the powders. The powder particle size was estimated from the SEM micrographs by using a public domain Java-based image processing software ImageJ 1.8 [32-33, 41] as a representative of the population. The statistical analysis of the particle size distribution is performed using a commercially available statistical analysis software MINITAB®. The bright field image and the selected area diffraction pattern was obtained using a JOEL-3010 transmission electron microscope (TEM) as shown in figure 40 operating at 300 KV. The average grain size was estimated from the TEM micrographs by image analysis technique using ImageJ 1.8 and was compared with the estimated grain size from the XRD for the respective powder.

Figure 39 JOEL IT500 scanning electron microscope

Figure 40 JOEL-3010 transmission electron microscope

4.2.2 Magnetic characterization

Magnetic characterization of the samples was performed by using Quantum Design VersaLab 3-T vibrating sample magnetometer (VSM). The equipment is shown in Figure 41. The

magnetic properties—saturation magnetization (M_S) intrinsic coercivity (H_{CI}) and remanent magnetization (M_R) of the as-received (S0) and the milled powders were approximated from the magnetization (M) versus applied magnetic field (H) curves (hysteresis loops) at ambient temperature (300 K), at sub-ambient temperatures (as low as ~60 K), and at elevated temperatures (as high as ~900 K). Thermomagnetic curves (M) v Temperature(T) from ~ 300-900 K were used to understand the nature of the sample either reversible or irreversible and also any possible occurrence of phase changes with the exposure to temperature. All the elevated temperature runs were performed in a high vacuum to avoid oxidation of the samples. The samples were wrapped in a copper foils during the measurement to withstand at elevated temperatures. The MvH curves of the thermally treated sub-ambient runs were also generated at ambient and sub-ambient temperatures.

Figure 41 Quantum Design VersaLab 3-T vibrating sample magnetometer setup

The saturation magnetization (M_S) was evaluated from the hysteresis loop by adopting the Law of Approach to Saturation (LAS) [1–3,64,65], while the intrinsic coercivity (H_{CI}) and the remanent magnetization (M_R) were approximated by averaging the intercepts of the hysteresis loop at the magnetization (M) and applied magnetic field (H) axis. The estimation of M_S for ferromagnetic and/ or ferromagnetic materials is based on the following expression:

$$M = M_S (1 - a/H - b/H^2) + \psi H \tag{6}$$

where M is the magnetization for an applied magnetic field H, M_S is the saturation magnetization. The terms a/H, b/H^2, and ψH are related to the presence of inhomogeneity (micro stress, inclusions, etc.), magneto crystalline anisotropy, and forced magnetization, respectively. At H greater than $\sim$475kA/m ($\sim$6kOe), the M vs $1/H^2$ plot was fitted to a straight line, and the intercept at the magnetization axis was estimated as M_S. For a decent statistical sampling, the characterization was performed on a minimum of three sets of samples for each condition, and the results correspond to an average and standard deviation.

For ferromagnetic materials, the dependence of M_S on T in the region of low temperatures is given by Bloch's law:

$$M_S(T) = M_S(0)\,[1-AT^{3/2}] \tag{7}$$

where $M_S(0)$ is the saturation magnetization at absolute zero (0 K), and A is a constant [36, 39-40]. Upon fitting the experimental results with Eq. 5, from the sub-ambient runs, $M_S(0)$ and A of the samples were estimated.

At absolute zero, where complete saturation is attained, the saturation magnetization is given by the maximum magnetic moment per atom (μ_H) in the direction of the applied magnetic field multiplied by the number of atoms per gram, given by:

$$M_S(0) = \mu_H\,(N/A_w) \tag{8}$$

where N is the Avogadro's number, and A_w is the atomic weight (or molecular weight). This gives the magnetic moment of the alloy without any exterior inclusions.

CHAPTER 5: RESULTS AND DISCUSSION

5.1 Vial temperature

The macroscopic temperatures of the vial were measured at the start, at the end of milling after every 3 h cycle and intermediately when excessive cold-welding occurred. Stearic acid of ~3 wt.% was added intermediately at 5 h, and 23 h of milling as excessive cold welding was observed. A graph is plotted between milling time and vial temperature (Figure 42) which shows the effect on vial temperatures with the increase in the duration of milling. This plot can give information about the complex milling process based on the temperature variations. Qualitatively, the vial temperatures recorded showed two different trends, and the difference in the trend is shown in the plot with a gradient change. The vial temperatures were observed to be in the range of $\sim 315.3 \pm 1$ K till 10 h of milling. These increased with further milling after 10 h and maintaining a range of $\sim 318.2 \pm 1.4$ K. Unlikely as estimated trends; there is a dip in the vial temperature at 23 h of milling, this is due to the effect of excessive cold welding. After adding the PCA, the vial temperature raised and followed the trend.
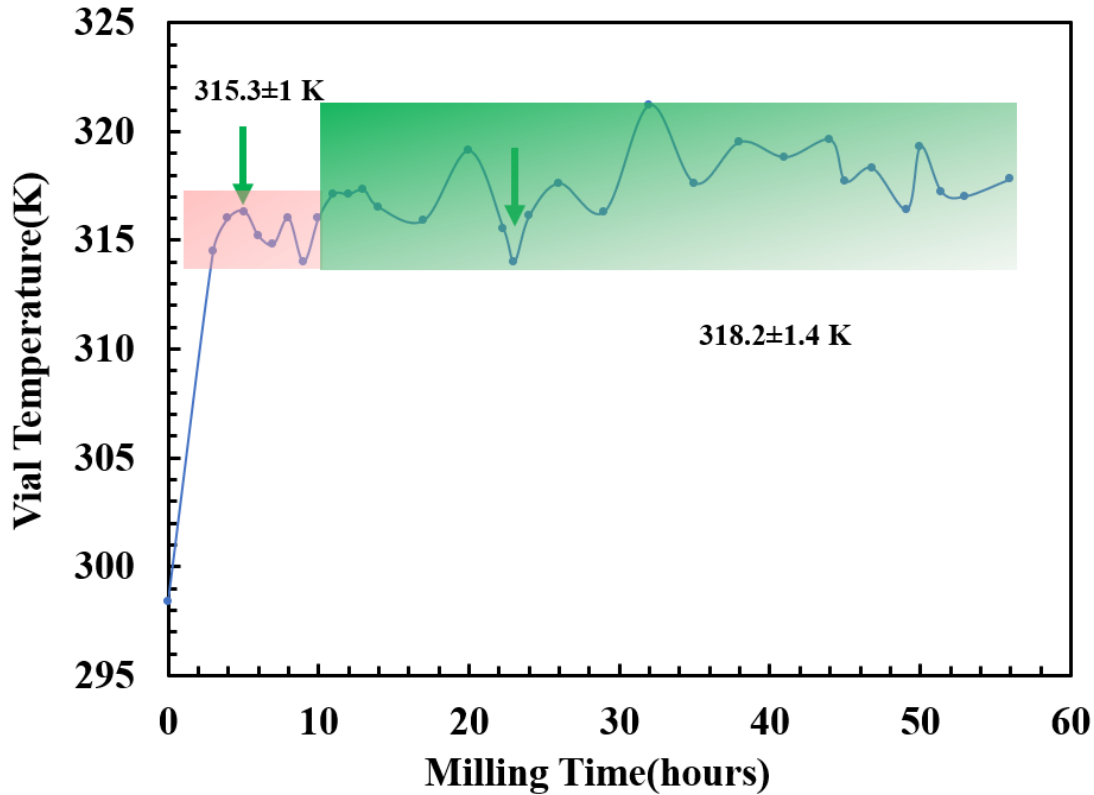
Figure 42 The macroscopic temperature of the vial during the milling

The rise in the macroscopic measurement of the vial temperature during milling is indirectly the measure of the macroscopic measurement of the powders inside the vial during the milling. Even though the temperature rise is a very less, i.e., only by ~3 K, using Minitab, performing a paired-T test gave the P-value is 0.003 stating that there is a statistically significant change in the vial temperature.

The increase in temperature during the milling is due to the kinetic energy imparted by grinding media and any exothermic (or endothermic) processes occurring during the milling that generates heat. The mechanical milling of the powders results in severe mechanical deformation of the powder that leads to the generation of crystal defects. These crystal defects, along with the balance between the repeated cold-welding and fracturing among the powder particles, affect the structure of the powders [31-32]. After milling for a certain length of time, a steady-state equilibrium is to be attained when a balance is achieved between the rate of welding and the rate of fracturing. Excessive cold welding was observed after certain hours of milling. The initial

increase in the vial temperature till 10 h corresponds due to the dominance of fracturing of elemental powders over cold welding. The further increase in the temperature to a near-constant temperature at milling time greater than ~10 h indicates the possible chances of occurrence of phase changes in the powder due to severe plastic deformation. This observed increase in the temperature may be due to the difference in the ball to powder ratio, wt.% of PCA and the nature of the material being milled.

The macroscopic rise of temperature of the vial (or powder) has been measured with thermocouples in some cases. In the case of Al-Mg, the temperature of the vial stabilized at ~323 K during milling in a SPEX 8000 mill at a ball-to-powder ratio of 7:1. In the case of Group V transition metal-silicon systems— V-Si, Nb-Si, and Ta-Si; with a ball-powder ratio 5:1 for V-Si and 10:1 for Nb-Si and Ta-Si— the maximum temperature did not exceed ~353 K [54]. The vial temperature in this study is less when compared with them. Thus, the differences in the vial temperature are probably due to the differences in the nature of the material, the ball to powder ratio, and the media.

5.2 Structure and magnetic properties at ambient temperature

Mechanical milling was performed on the pre-alloyed gas-atomized powder/as-received powder (S0) by adding 3wt.% stearic acid whenever cold-welding was observed and removing a small amount of powder at certain intervals (intermediate stages) for characterization as a representative for the hours of milling(3h, 5h, 8h, 14h, 20h, 23h, 35h, 47h, and 56h). X-ray diffraction spectra of these powders along with the as-received powder at a 2θ range 20°-100°. Figure 43 shows the x-ray diffraction pattern of these powders recorded at room temperature. The x-ray diffraction patterns showed the presence of different phases with the milling. The peaks were identified using the direct comparison method by comparing the peaks of the XRD patterns in the literature. The as-received powder consists of predominantly martensite α phase and small traces of retained-austenite γ phase, as shown in Figure 43. Milling the as-received powder till 8 hours resulted in complete martensitic α phase and there were no traces of retained-austenite. While further milling resulted in the evolution of some extraneous phases of precipitates from 14 hours of milling.
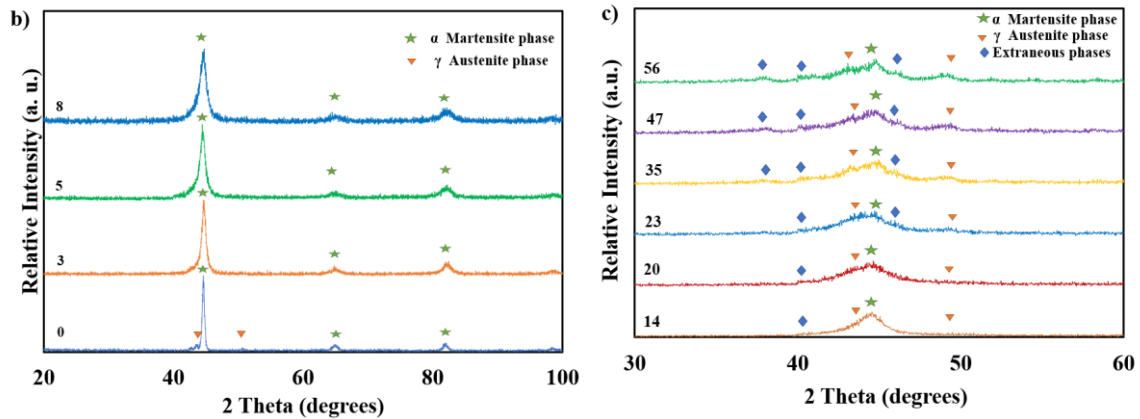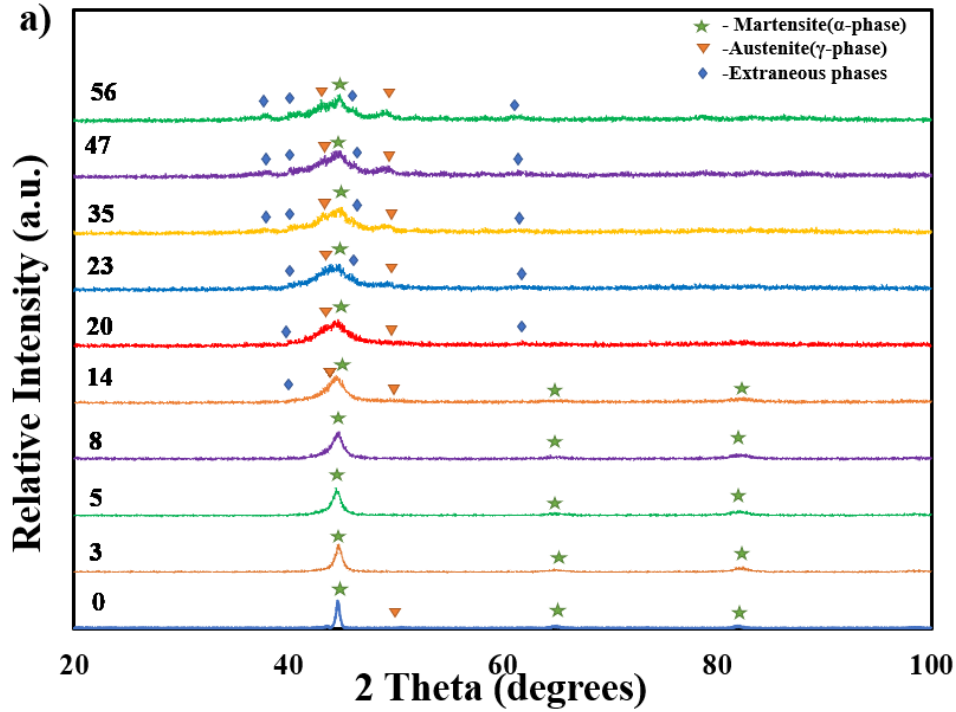
Figure 43 a) X-ray diffraction spectra of the milled powders and the pre-alloyed gas-atomized powder (S0). b) X-ray diffraction spectra of the S0 powder and milled powders (S3, S5, and S8) at a 2θ range 20°-100°. c) X-ray diffraction spectra of the milled powders (S14, S20, S23, S35, S47, and S56) at a 2θ range 30°-60°

For a better understanding of the phases, the XRD patterns of the S0, S3, S5, and S8 are shown in Figure 43 b. It was observed that the as-received powder comprises of predominantly martensite α phase and small traces of retained austenite γ phase. A similar trend was also observed in the maraging steel 300 synthesized by hot forging and selective laser melted (SLM). They too

showed a relatively small traces of retained austenite along with the martensite [10, 15-17]. The retained austenite usually tends to arise from the micro segregation of solute elements (particularly Ni) at cellular boundaries during solidification. The traces of austenite detection can be due to the enrichment of Ni, which stabilizes the retained austenite [52]. While mechanical milling of the as-received powder for a duration till 8 h showed the presence of only martensitic α phase. No traces of retained austenite were found. The retained austenite is metastable and is known to transform to martensite during cold-working [11]. The severe mechanical deformation of the powder particles due to the repeated flattening, cold-welding, fracturing, and rewelding of the milling media during the mechanical milling transformed the retained austenite present in the as-received powder to martensite. Similarly, maraging steel when solution treated at 1273 K, followed by water quenching and deformation is known to have a complete martensitic structure. The broadening of the peaks indicated the presence of nanocrystalline grains and lattice strain in the milled powder. Also, the broadening of the peak increased with the increase in hours of milling stating the powder being nanocrystalline even milled for longer durations.

By continuing milling further after 8 h showed the evolution of some extraneous phases. The evolution of the extraneous phases and the austenite can be seen in the above Figure 43 c showing the XRD pattern from a θ-2θ scan range of 30°-60° of the milled powders for 14 h, 20 h, 23 h, 35 h, 47 h, and 56 h. These peaks intensity increased with the increase in the milling duration. Heat treating the sample at 1273 K resulted in the formation of precipitates of $Ni_3(Mo, Ti)$ [50]. Similarly, the evolved extraneous phases are probably the precipitates of $Ni_3(Mo, Ti)$, $FeMo_2$, etc. The broadening of the peaks increased with the milling duration. Since it was difficult to finalize the peaks from the XRD patterns of these samples, it was challenging to find the grain size, lattice strain, and lattice parameter of these powder samples. As the formed precipitate peaks are much closer to each other, it was difficult to estimate the grain size, lattice parameter, and the lattice strain of the milled powder more than 8 h.

Thus, the lattice parameter, lattice strain and the average grain size of the as-received and milled samples of 3h, 5h, and 8 h were estimated from Bragg's equation and Williamson Hall method respectively. These parameters of the powders are shown in Figures 44 and 45. The lattice parameter of the martensite α phase in as-received powder was estimated to be ~ 0.2881±0.0004 nm using equation (1) which is near similar (within ~0.5%) to the lattice parameter of martensite

in maraging 300 steel (~0.2886 nm) [13]. The lattice parameter of the martensite α phase in milled powders was estimated, and they are near the constant value of ~ 0.2873±0.0003 nm. The lattice parameter of the martensite in the milled powders is ~ 0.2 % less than the lattice parameter of martensite in the as-received powder. Minor differences in the lattice parameter of the powder obtained by high energy ball milling could be likely due to the combined effect of the presence of nanocrystalline grains and lattice distortion (due to lattice strain). This can be concluded by the grain size and the lattice strain.

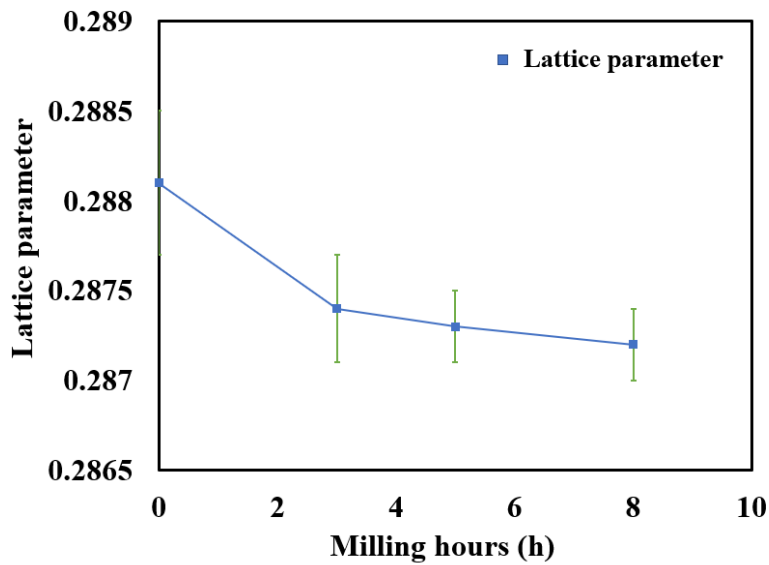Figure 44 Lattice parameter of the as-received (S0) and milled powders of S3, S5, and S8; estimated from their respective XRD spectra at ambient temperature
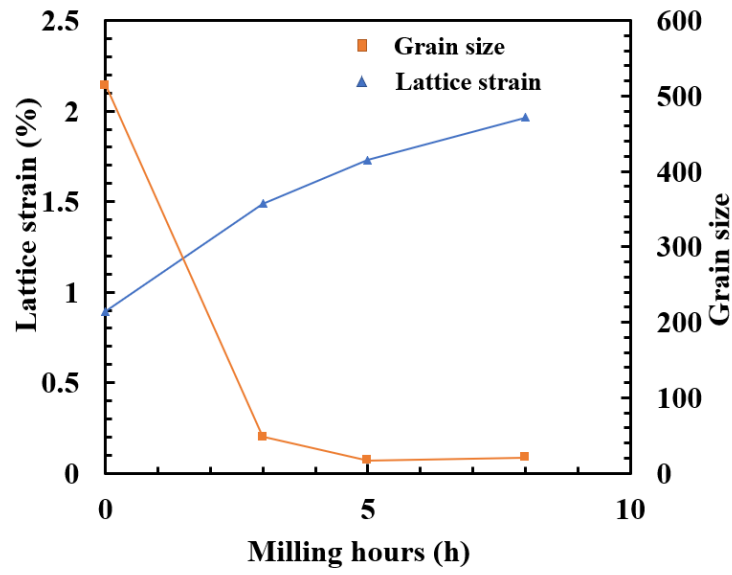
Figure 45 Lattice strain and grain size of the as-received (S0) and milled powders of S3, S5, and S8; estimated from their respective XRD spectra
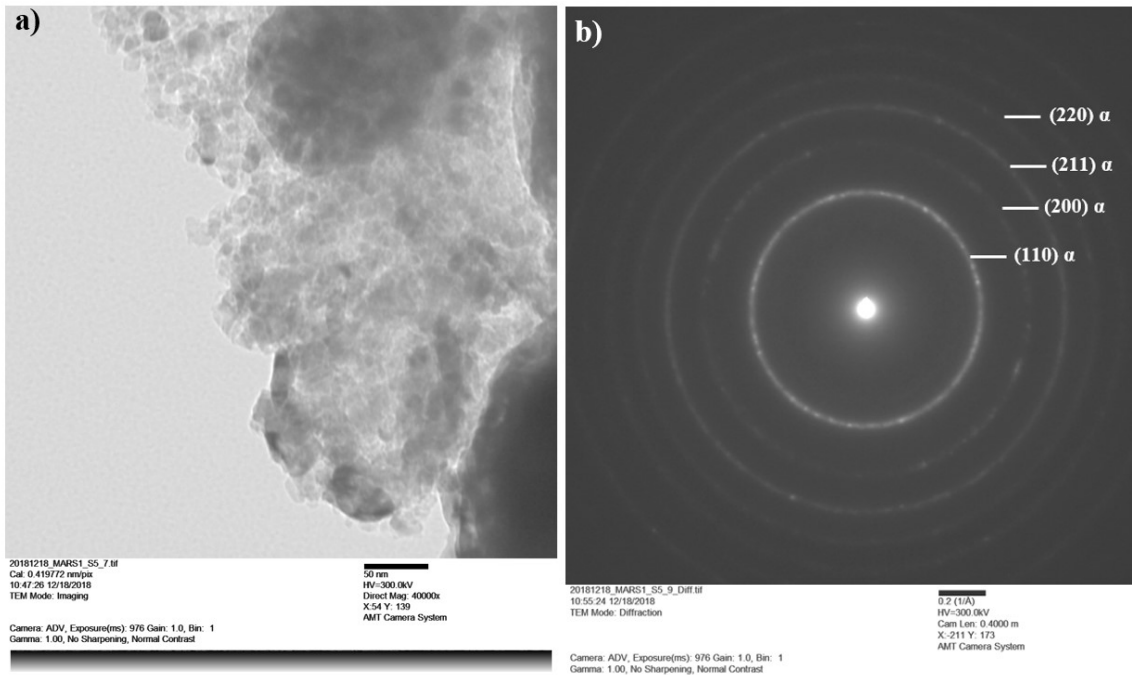
Figure 46 a) Bright field image and b) Selected area diffraction pattern of the maraging steel powder milled for 5h

The grain size and lattice strain of the as-received powder and the milled powders were ~ 513 nm & 0.895 %(S0), ~48 nm & 1.49 %(S3), ~17 nm & 1.73 % (S5), ~21 nm & 1.96 % (S8) respectively. The milled maraging steel powders till 8 h are in the nanocrystalline regime. Figures 46 a and b shows the TEM images of the powder milled for 5 h, as a representative of the milled powders (S3, S5, and S8). The grain size was estimated to be ~11 nm from the bright field image (Figure 46 a) which is in fair agreement to the grain size estimated from the XRD pattern of the 5 h milled powder. The selected area diffraction pattern was indexed to martensite (α phase), as shown in Figure 46 b.

Figure 47 shows the typical morphology of the as-received was observed to be predominantly spherical, with low levels of asymmetric particles. The milled maraging steel powders were irregularly shaped, and the size distribution of the powders particles was rather inhomogeneous, consisting of predominantly finer particles coupled with a fair amount of coarser particles. The reason for the coarser particles is due to the agglomeration of the particles due to excessive cold welding. Majority of the particles are finer than the as-received powder, which is probably due to the repeated fracturing. Powder particle size distribution (histograms) of the as-received powder and milled powders for a milling duration of 3, 5, 8, 14, 20, 23, 35, 47, and 56 h on population basis respectively are shown in Figure 48 a. Qualitatively, the particle size distribution of the as-received powder seems to be coarser and by milling the powders become finer. Figure 48 b shows the cumulative particle size distribution. The powder particle size characteristics D_{10} (the particles size equal to or less than 10 % of the powder particles by population), D_{50} (the particles size equal to or less than 50 % of the powder particles by population), and D_{90} (the particles size equal to or less than 90 % of the powder particles by population) of the as-received moreover, milled powders was estimated from the SEM images using ImageJ. These characteristics are shown in Figure 48 c. D_{90} of the as-received powder was found to be ~ 21 μm. The D_{90} of the nanocrystalline maraging steel powders (milled for 3h, 5h, and 8h) are ~8.5 μm, ~ 8.9 μm, and 5.7 μm. The particle size decreased with the increase in the milling hours till 20 h and started to increase with further milling duration. D_{90} of the milled powders reached a minimum of ~4.5 μm at 14 h and 20 h of milling. The increase in the particle size can be accommodated to the increase in the rate excessive cold welding which results in the agglomeration of the powder and forming coarser particles. D_{90} of the milled powders above 20 h increased gradually and the value at 56 h is ~5.5 μm.
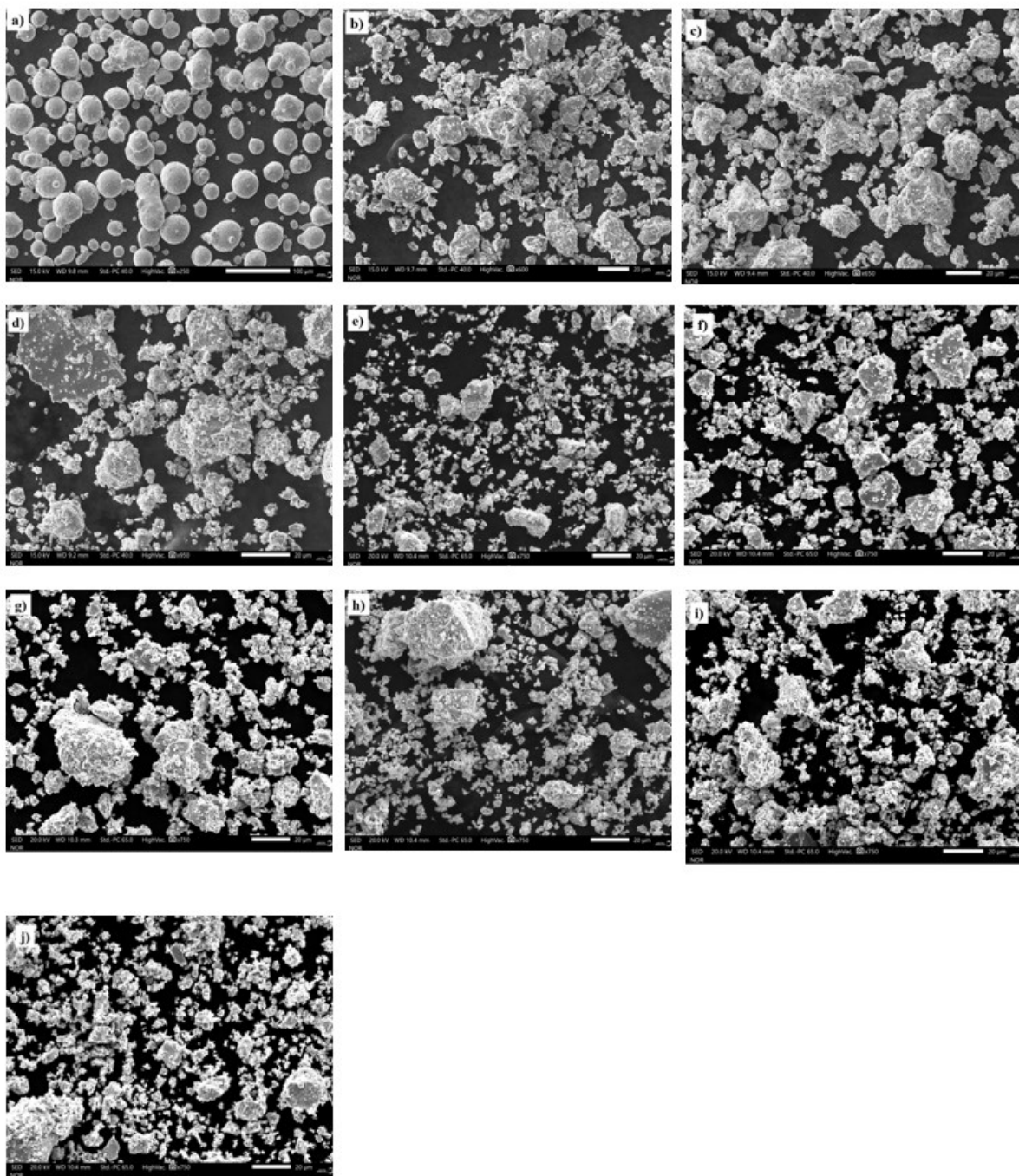
Figure 47 Scanning electron micrograph of the a) as-received powder (S0) and milled powders b) 3 h, c) 5 h, d) 8 h, e) 14 h, f) 20 h, g) 23 h, h) 35 h, i) 47 h, and j) 56 h respectively, at a magnification of ~750 X
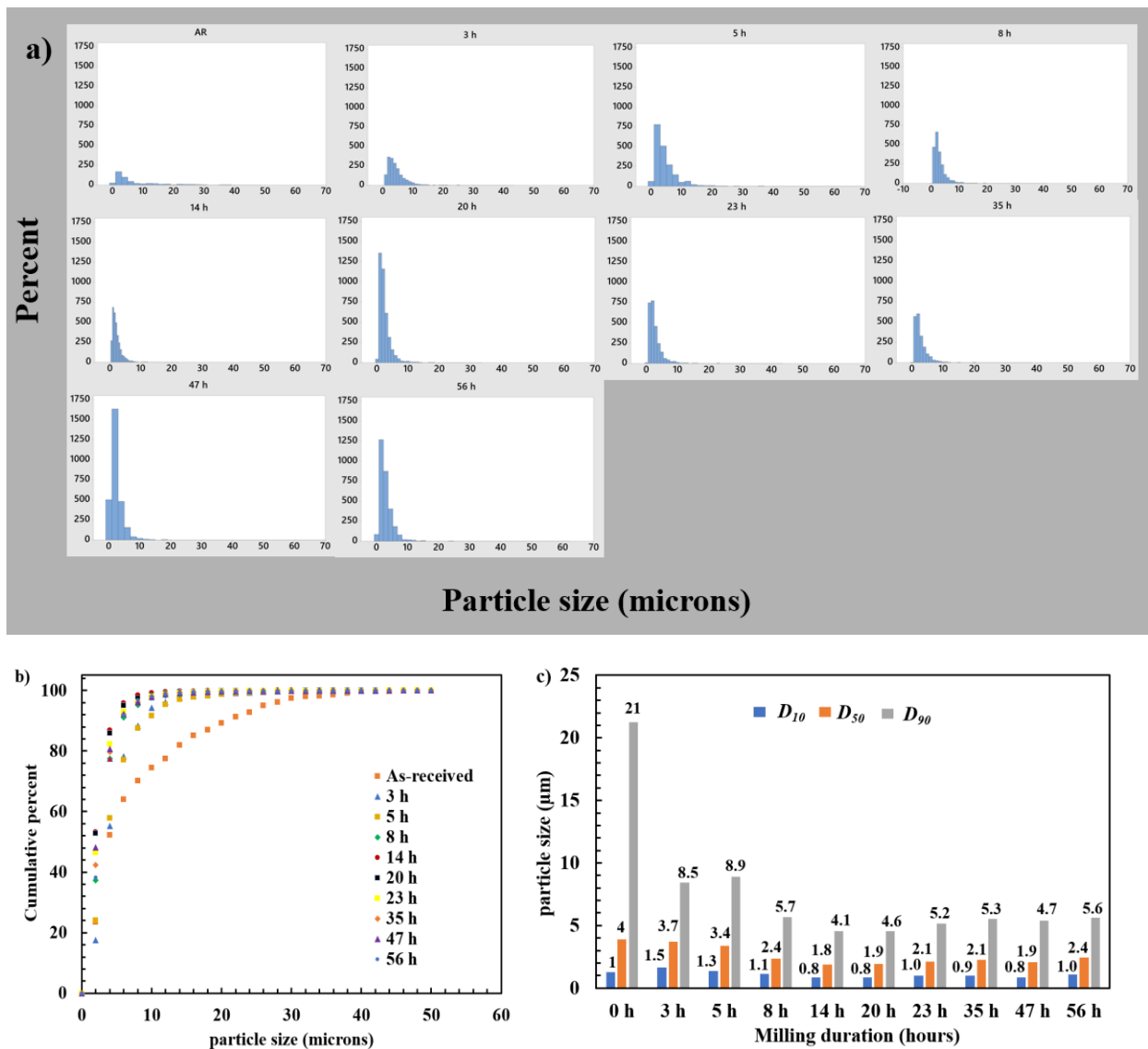
Figure 48 a) Powder particle size distribution (histograms), b) cumulative particle size distribution, and c) D_{10}, D_{50}, and D_{90} of the as-received powder and milled powders for a milling duration of 3, 5, 8, 14, 20, 23, 35, 47, and 56 h respectively

Magnetic properties were measured by generating the magnetization (M) versus the applied magnetic field (H) curves at ambient temperature. The magnetization (M) versus the applied magnetic field (H) curves of the as-received maraging steel powder(S0) and the milled powders for different hours are presented in Figure 49. The inset shows the M-H curves at low magnetic field region (± 10kA/m).
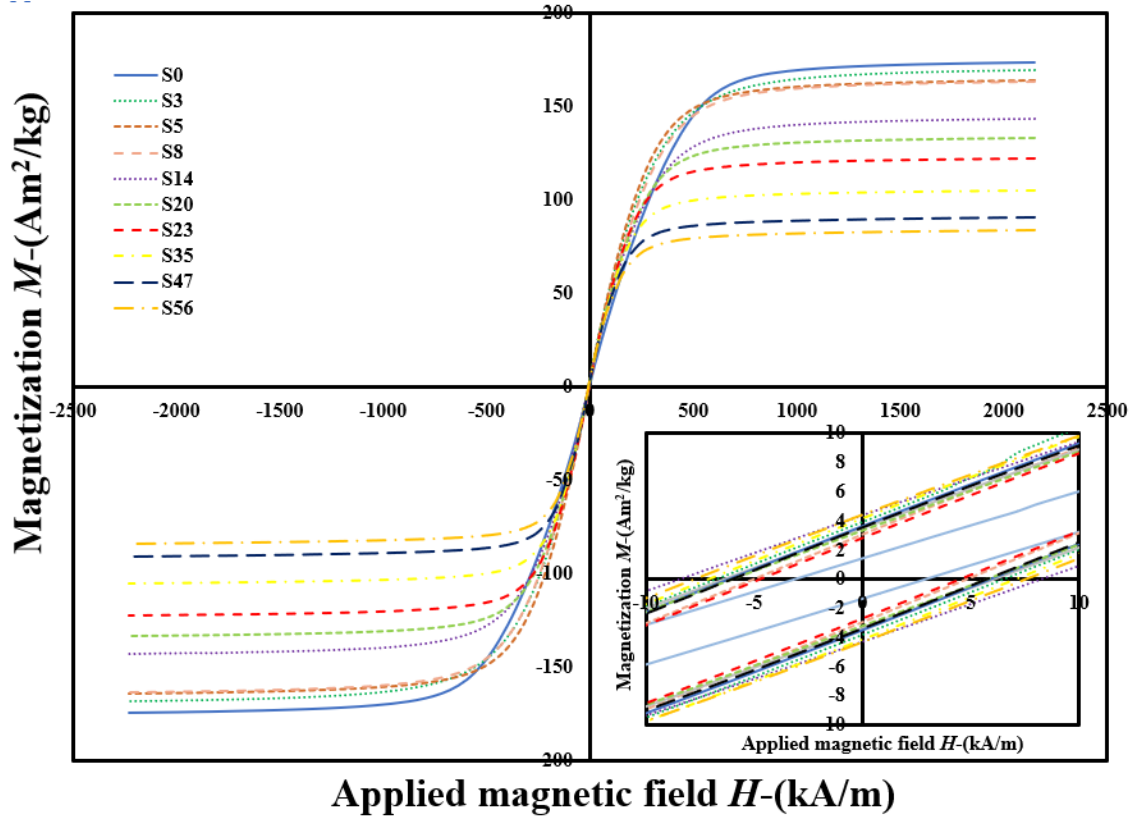
Figure 49 Magnetization (*M*) versus applied magnetic field (*H*) curves of the as-received powder (S0) and the milled powders

The saturation magnetization (M_S) can be observed that it decreased with the increase in hours of milling. The M_S of the pre-alloyed gas-atomized powder was estimated as $\sim 176\pm2$ Am^2/kg. The M_S of maraging 300 steel sheet specimen at ambient temperature was recorded as $\sim$188 Am^2/kg [27]. The decrease in M_S by $\sim$6% can be attributed as the increased surface area in powders, which result in a relatively higher degree of magnetic disorder in powders. Milling of the as-received powder resulted in a decrease in the M_S. The decrease in M_S is due to the increase in the surface effect (i.e., a greater fraction of surface spins leading to relatively smaller net moment) due to the decrease in particle size during mechanical milling [36, 38-39]. The trend of M_S of the as-received and the milled powders are shown in Figure 50 a. The dashed lines show the value of M_S comparison between the M_S of as-received, milled nanocrystalline maraging steel powder with maraging steel in sheet form [27] and a nanocrystalline $Fe_{46}Co_{34}Ni_{20}$ alloy [55]. M_S of nanocrystalline $Fe_{46}Co_{34}Ni_{20}$ alloy is $\sim$169 A m^2/kg which is like the as milled nanocrystalline

maraging steel powders. Thus, the nanocrystalline milled maraging steel powders can also be used instead at room temperature. In the case of requiring similar magnetization, nanocrystalline form and comprising of single phase these powders can be used. If multiple phases are acceptable, the nanocrystalline $Fe_{46}Co_{34}Ni_{20}$ can be used as it has low coercivity.

The milled samples for a duration of 3 h, 5 h, and 8 h are nanocrystalline and show a minimal decrease in M_S and are ~ 169.3±1.88 Am^2/kg, ~165.5±1.5 Am^2/kg, and 164±3 Am^2/kg respectively. The decrease in M_S in the milled powders till 8 h could be due to the combined effect of reduced grain size and particle size when compared with the as-received powder. These powders are in the nanocrystalline form. While by further milling, the decrease in M_S is high. It can be not only due to the reduction in the grain size and the particle size but also the combined effect of the new phases - austenite and probably the precipitates of Ni_3(Mo, Ti) and Fe_2Mo. Formation of austenite associated with the precipitates started to occur after aging at high temperatures and which resulted in a decrease in the M_S [27]. The formation of precipitates and the austenite reduces the magnetization due to the martensite, and thus, a reduction in the M_S was observed [22].
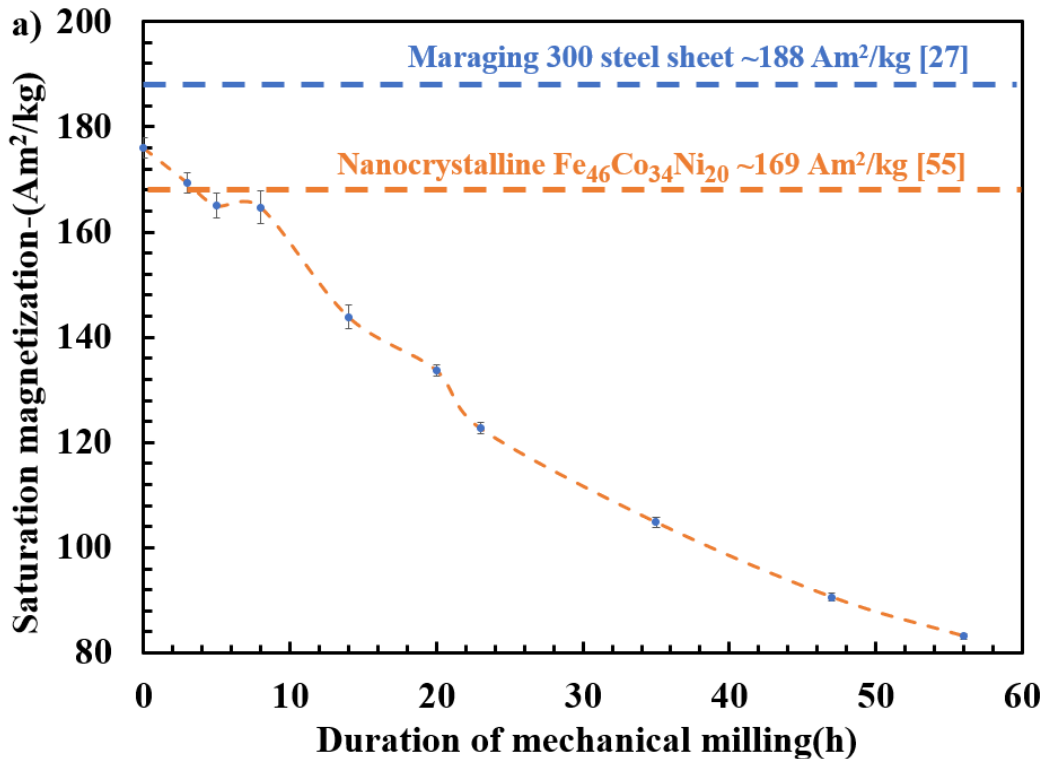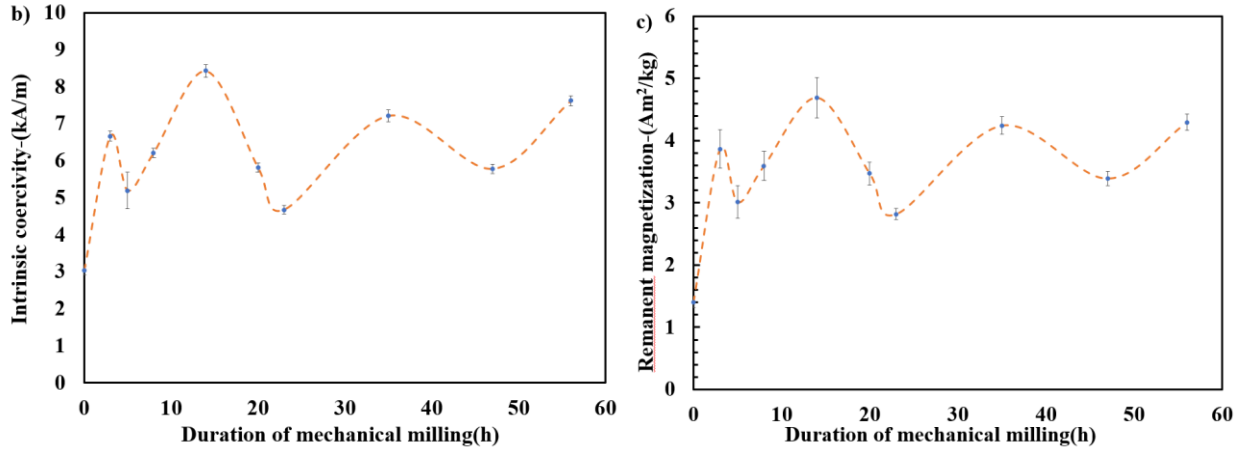
Figure 50 a) Saturation magnetization (M_S), b) Intrinsic coercivity (H_{CI}), and c) Remanent magnetization (M_R) of the as-received and milled maraging steel powders

While on the other side, the intrinsic coercivity (H_{CI}) changed abruptly with an increase in the duration of milling following a similar trend, as shown in Figure 50 b. H_{CI} of the as-received powder was estimated as ~3.0±0.11 kA/m. The H_{CI} increased with milling when compared to the as-received powder, but there was a subsequent trend followed. It reached a maximum of ~8.4±0.17 kA/m at 14 h of milling. The H_{CI} of the milled sample fluctuated between ~4.7±0.12 kA/m – 8.4±0.17 kA/m. H_{CI} is a structure-sensitive property. It is strongly influenced by the magneto crystalline anisotropy, grain size, particle size, lattice strain, and no of the phases present. The increase in H_{CI} in the milled powders when compared with the as-received powders can be attributed as the effect of the decrement in the grain size, particle size and increment in the lattice strain during the milling process, also the evolution of new phases due to milling for a longer duration. There are fluctuations in the trend of H_{CI}.

From the grain size, lattice strain and the lattice parameter estimated from the XRD patterns of the as-received, milled powders of 3 h, 5 h, and 8 h; particle size from the SEM micrographs— it is helpful to explain the subsequent changes in the trend till 8 h of milling. The D_{90} particle size of 3h &5h is ~8.5 μm and ~8.9 μm respectively. However, the grain size of the 5h milled powder (17.32 nm) is ~3 times less than the sample milled for 3 h. Thus, the lower grain size has a higher influence on the H_{CI}, which reduces to 6±0.12 kA/m. While the samples milled for 5h and 8 h have a similar grain size of ~ 17.32 nm & ~ 21.12 nm respectively. However, the particle size of the 5 h milled powder is ~ 1.5 times greater than the 8 h milled sample. The higher H_{CI} for 8 h milled

68

powder when compared to the 5 h milled powder is mainly due to the effect of finer particle size distribution. As it was difficult to estimate the grain size, lattice strain and the lattice parameter of the powder milled for more than 8 h, we cannot conclude the reason for the subsequent decrease in the H_{CI}. The reason could be additionally due to the extraneous phases too. A clear understanding of this trend can be evaluated by understanding the phases that evolved from the TEM micrographs.

Like the trend of intrinsic coercivity (H_{CI}), remanent magnetization (M_R) changed abruptly with an increase in the duration of milling following a trend, as shown in Figure 50 c. The M_R of the as-received powder was estimated as ~1.4±0.08 Am^2/kg. Due to the crystal defects induced during the milling and lattice distortion, the M_R followed an abrupt change in the milled samples. It reached a maximum of ~4.7±0.3 Am^2/kg in 14 h milled powders and reached a minimum of ~2.8±0.09 Am^2/kg at 23 h. This could be due to the similar reasons stated for the H_{CI}.

5.3 Magnetic properties at cryogenic temperatures

The as-received and the milled powders magnetic properties were measured at sub-ambient temperatures from as low as ~60 K to ambient temperatures 300 K at regular intervals of 30 K. This approach was considered to understand the influence of cryogenic temperatures on the magnetic properties and to investigate whether these powders can be used for the cryogenic applications. The magnetization (M) versus applied magnetic field (H) curves of these powders are shown in Figure 51, and inset in each figure shows an enlarged view of the respective M vs. H curves at a low magnetic field region of ± 10 kA/m.
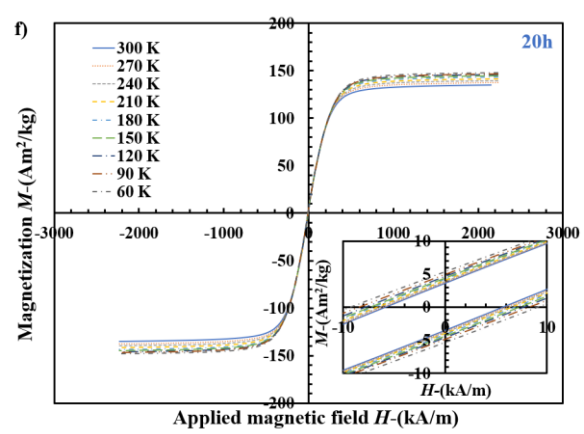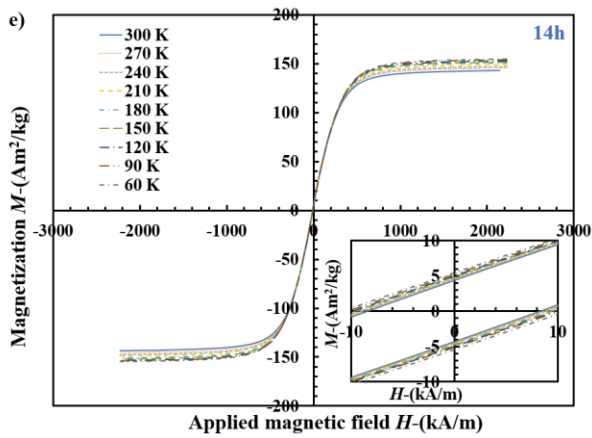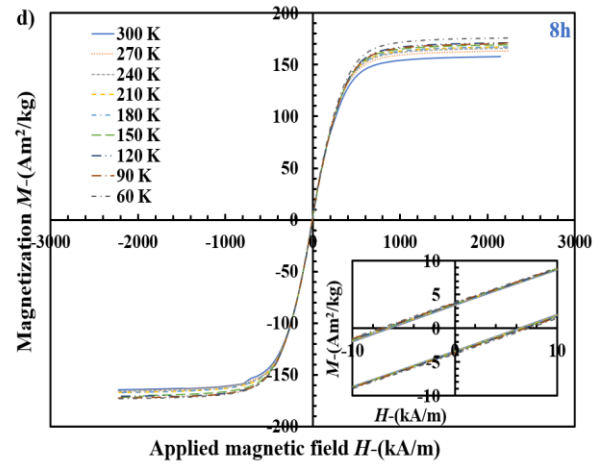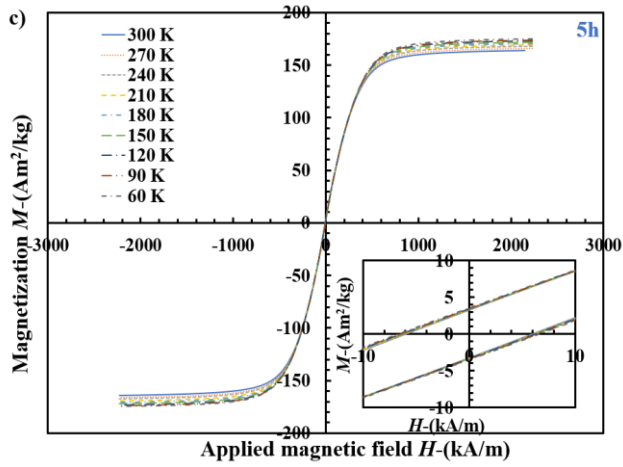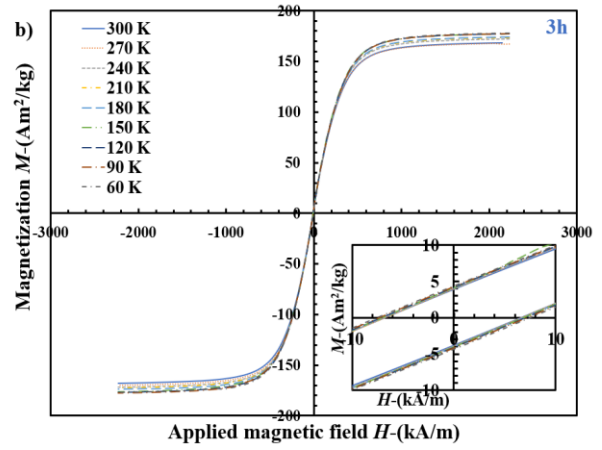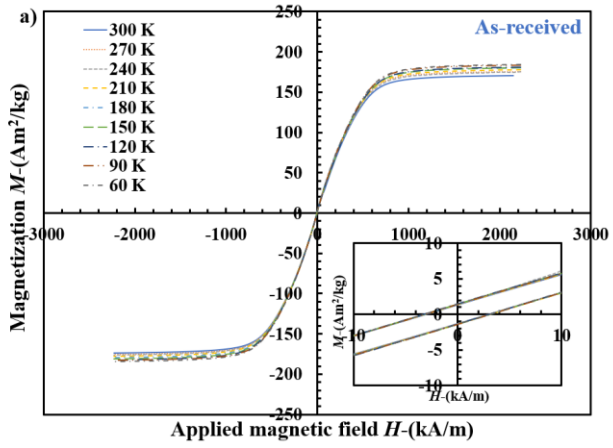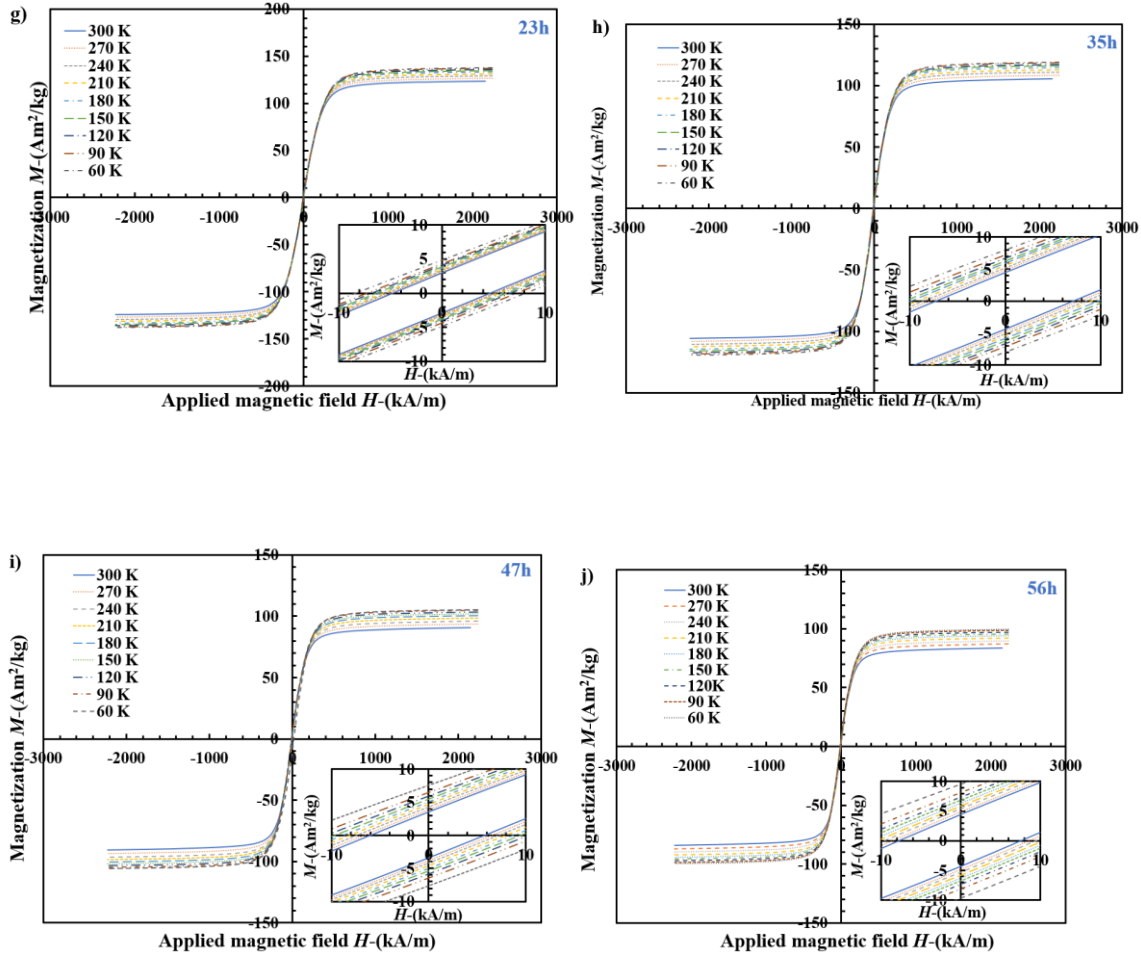
Figure 51 Magnetization(M) versus applied magnetic field (H) curves of the a) as-received powder and the milled powders for b) 3 h, c) 5 h, d) 8 h, e) 14 h, f) 20 h, g) 23 h, h) 35 h, i) 47 h, and j) 56 h; from temperatures of 60 - 300 K respectively. The inset in each figure shows the M vs. H curves in a low magnetic field region of ± 10 kA/m

The M_S of the powders at various temperatures was estimated from figure 51, and the variation of M_S with temperature T is shown in figure 52. The M_S of the powders, irrespective of milling duration, showed a trend of decrease with the increase in temperature, which was expected since an increase in temperature decreases magnetic ordering [30, 36, 42-43]. The decrease in the M_S from 60 - 300 Kranged followed two different rates. The as-received and the nanocrystalline milled maraging steel powder till 8h showed a decrease with the increase in temperature by ~ 5-7 %. While the milled samples more than 8 h showed a substantial decline ranging from ~8-16 %. The M_S (0) (saturation magnetization at absolute 0 K) of the powders were estimated by fitting the observed experimental results in the equation (6) as mentioned in the experimental procedure. The M_S (0) and the constant A values can be seen in the equations plotted next to the trend of their

respective M_S. The as-received powder was estimated to have the highest M_S (0) of ~188.95 Am²/kg and reduced gradually with increase in milling time and reaching to a minimum of ~ 101.62 Am²/kg for 56 h milled powder. Contrarily to the trend of M_S (0) with the increase in milling duration, A constant value increased. The value of A for the as-received powder was estimated as ~1.3×10^{-5} K$^{-3/2}$, and it increased gradually to ~3.3×10^{-5}K$^{-3/2}$ for 56 h milled powder with an increase in milling. The estimated value of constant A remained nearly constant of ~1.3×10^{-5} K$^{-3/2}$ till 8 h of milling similar to the as-received powder. This is close to the typical experimentally estimated value of A for Ni, reported in the literature ~$0.75 \pm 0.2 \times 10^{-5}$ K$^{-3/2}$ [40].
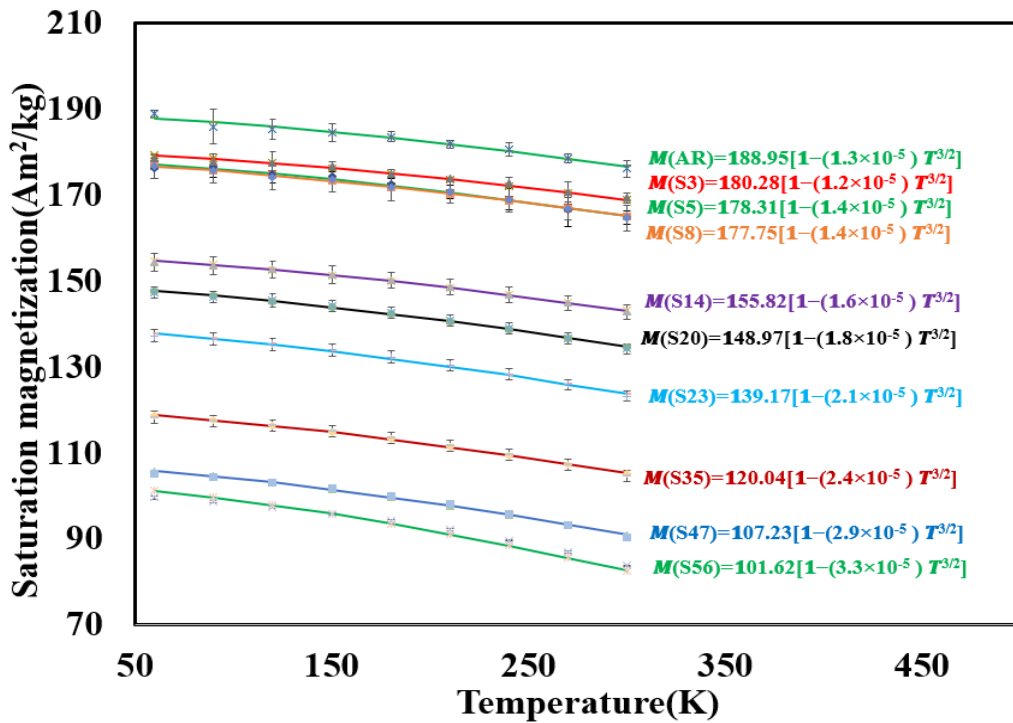
Figure 52 M_S versus temperature (T) of the as-received powder and the milled powders from 60-300 K

At absolute 0 K, where complete saturation is attained, the saturation magnetization is given by the maximum magnetic moment per atom (μ_H) in the direction of the applied magnetic field multiplied by the number of atoms per gram. The atomic weight of a nominal composition maraging steel powder is ~ 57.12 g/mol. From equation (7) the μ_H was calculated, and it was found that it decreased with the increase in milling duration. The trend is shown in Figure 53. The nanocrystalline milled maraging steel powders comprising of single α phase (milled for 3h, 5h, and 8 h) maintained nearly a similar μ_H of ~1.83 μ_B (where μ_B is Bohr magneton, and its value is

~9.27×10^{-24} J/T). Even though comprising of single α phase, the μ_H value decreased by ~5% when compared to the as-received powder (comprising of both α phase and γ phase). Probably the presence of crystal defects imparted during the milling dominate and thus a decrease in μ_H was observed in the milled powders for 8 h. This decline started to increase at a high rate after the 8 h of milling can be not only due to the crystal defects but also due to the emergence of extraneous phases of the precipitates.
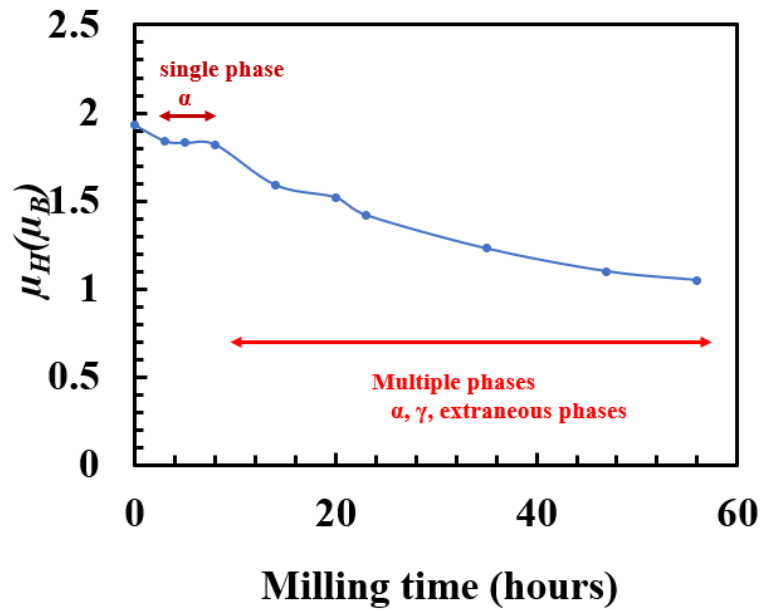
Figure 53 Maximum magnetic moment of the powders (µH) at absolute 0 K

a)

S56-$H_{CI}(T)$ = $0.0001T^2$ - $0.0822T$ + 22.117; R^2 = 0.9792
S47-$H_{CI}(T)$ = $8E-05T^2$ - $0.0584T$ + 16.53; R^2 = 0.986
S35-$H_{CI}(T)$ = $5E-05T^2$ - $0.0446T$ + 16.294; R^2 = 0.9939
S23-$H_{CI}(T)$ = $3E-05T^2$ - $0.026T$ + 9.3964; R^2 = 0.9905
S20-$H_{CI}(T)$ = $4E-05T^2$ - $0.0269T$ + 10.602; R^2 = 0.9951
S14-$H_{CI}(T)$ = $2E-05T^2$ - $0.0184T$ + 11.983; R^2 = 0.9929
S8-$H_{CI}(T)$ = $1E-05T^2$ - $0.0078T$ + 7.5083; R^2 = 0.9907
S5-$H_{CI}(T)$ = $1E-05T^2$ - $0.0073T$ + 6.3522; R^2 = 0.9597
S3-$H_{CI}(T)$ = $1E-05T^2$ - $0.0081T$ + 7.9734; R^2 = 0.9836
S0-$H_{CI}(T)$ = $-5E-06T^2$ + $0.0016T$ + 3.0586; R^2 = 0.9565

b)

S56-$M_{R}(T)$ = $5E-05T^2$ - $0.0366T$ + 11.192; R^2 = 0.9859
S47-$M_{R}(T)$ = $3E-05T^2$ - $0.0275T$ + 8.6856; R^2 = 0.9888
S35-$M_{R}(T)$ = $2E-05T^2$ - $0.0214T$ + 8.8422; R^2 = 0.9947
S23-$M_{R}(T)$ = $2E-05T^2$ - $0.0135T$ + 5.3549; R^2 = 0.9912
S20-$M_{R}(T)$ = $2E-05T^2$ - $0.013T$ + 5.7844; R^2 = 0.9956
S14-$M_{R}(T)$ = $1E-05T^2$ - $0.0085T$ + 6.2717; R^2 = 0.9922
S8-$M_{R}(T)$ = $5E-06T^2$ - $0.0033T$ + 4.1013; R^2 = 0.9826
S5-$M_{R}(T)$ = $5E-06T^2$ - $0.0027T$ + 3.5193; R^2 = 0.8941
S3-$M_{R}(T)$ = $7E-06T^2$ - $0.0043T$ + 4.7087; R^2 = 0.9742
S0-$M_{R}(T)$ = $-3E-06T^2$ + $0.001T$ + 1.4241; R^2 = 0.7295

Figure 54 a) H_{CI} and b) M_R versus temperature (T) of the as-received powder and the milled powders from 60 - 300 K

The H_{CI} and M_R of the as-received, and the milled powders were estimated from Figure [51]. The trends of the H_{CI} and M_R of the powders are shown in Figure 54 a and 54 b respectively. It can be observed that the as-received powder and the nanocrystalline milled maraging steel

powders (milled for 3h, 5h, and 8 h) show a minimal change of ~ 5-11% when compared with the other milled powders. Powder milled for above 20 h showed a higher rate of decrease by ~ 1.7 to 2.1 times in both H_{CI} and M_R with the increase in temperature from 60 K to 300 K. In a temperature regime of 60 - 300 K the temperature typically has a negligible effect on the grain size and lattice strain. So, the observed decrease in the powders could be due to the decrease in the anisotropy field with an increase in temperature. These trends fit quadratically, and their values at absolute 0 K can be found by extrapolating the respective quadratic curves to absolute 0 K.

5.4 Magnetic properties at elevated temperatures as high as 900 K

To study the effect of T on the magnetic properties on these powders—the thermomagnetic curves (MvT) were plotted for the as milled and the as-received powders. The magnetic field was set to ~79.6 kA/m, and the magnetization was measured from temperatures 300 -900 K at a sweep rate of ~5 K/min in two different cycles: 1) heating (300 - 900 K) and 2) cooling (900 - 300 K). As the as-received, nanocrystalline milled maraging steel powders (milled for 3h, 5 h, and 8 h) showed better magnetic properties. Thermomagnetic analysis of these powders will be helpful to understand the effect of elevated temperatures on the magnetic properties. Also, the powder milled for 56 h was taken as a representative of the powders milled for more than 8 h (as the new phases started to evolve from 14 h of milling). Two consecutive MvT runs were performed on these powders (as-received, milled powders for 3 h, 5 h, 8 h, and 56 h respectively), as shown in Figures 55 a, 55 b, 55 c, 55 d, and 55 e. It is seen that qualitatively the as-received powder and the milled powders exhibit a reversible trend in both the 1st and 2nd MvT runs.
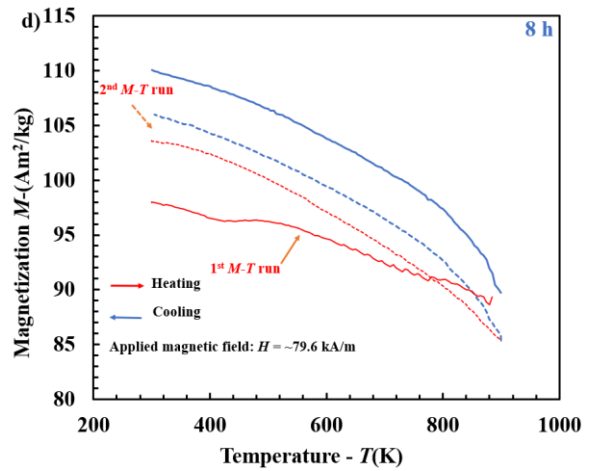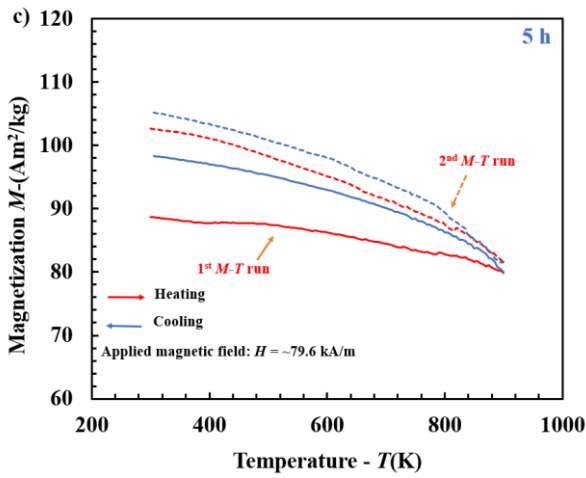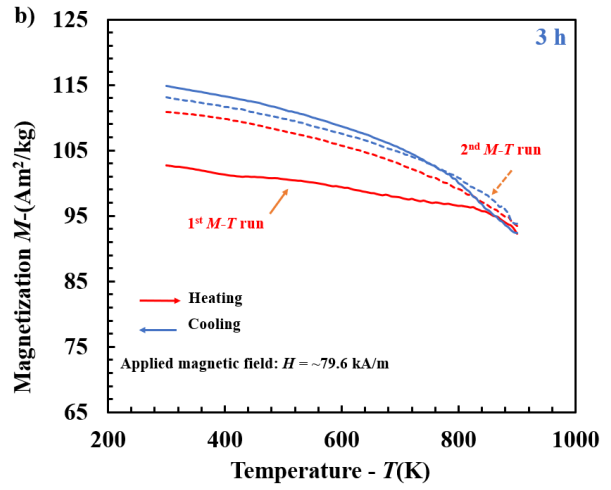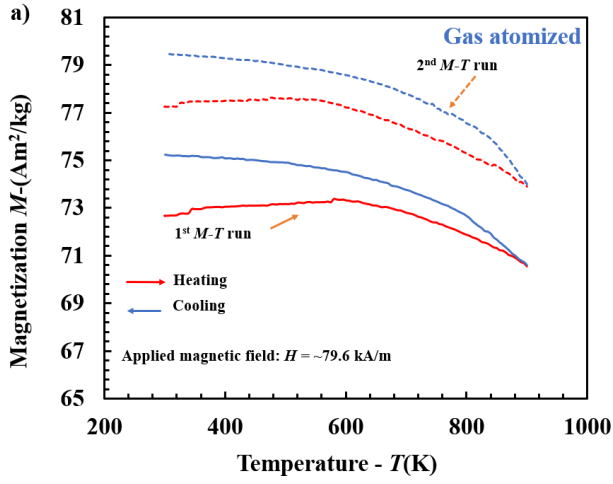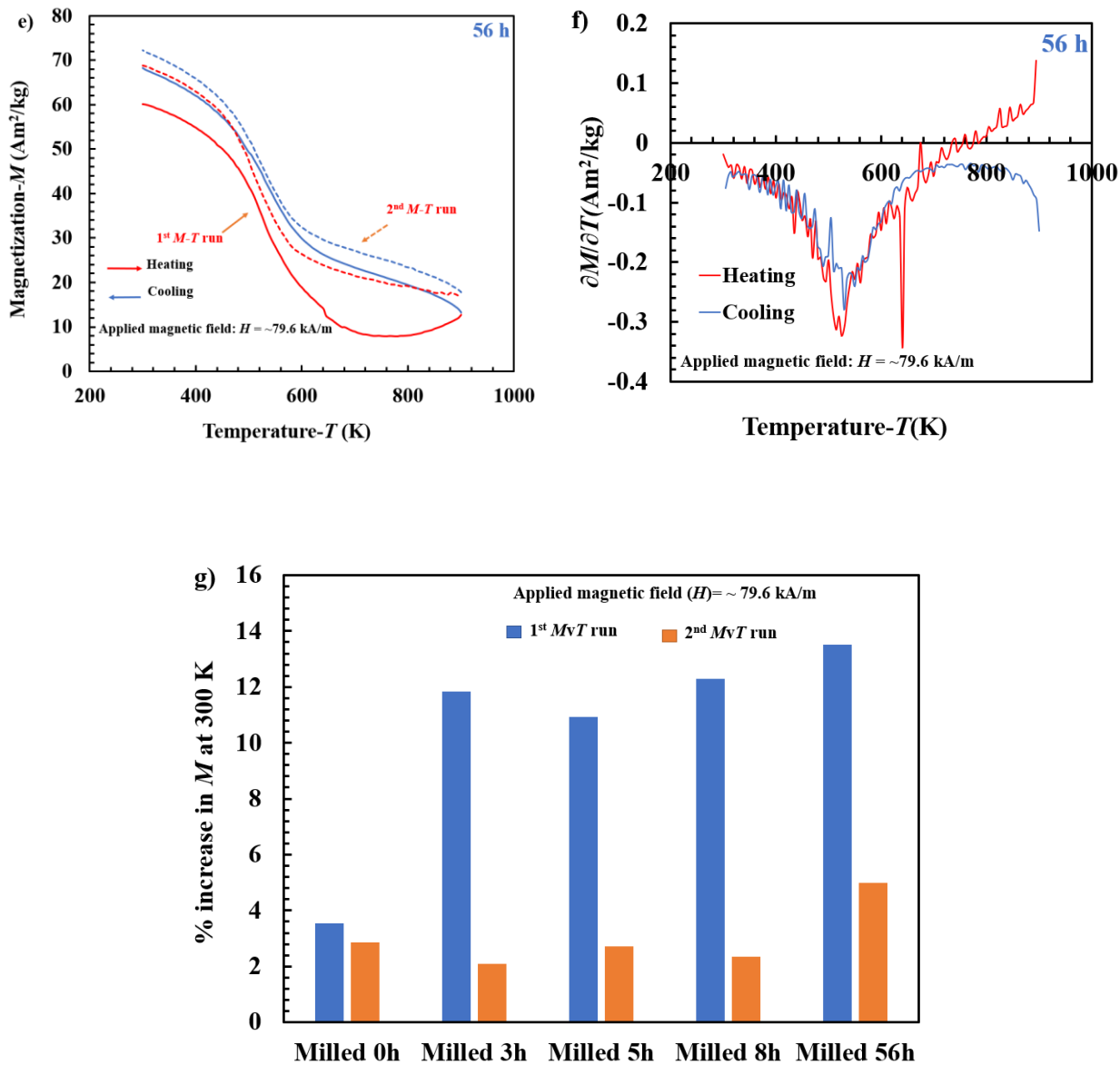
Figure 55 The thermomagnetic curves (*MvT*) of the a) as-received powder (S0) and the as-milled powders of b) S3, c) S5, d) S8, and e) S56; from 300-900 K and return, at ~5 K/min, and at an applied magnetic field (*H*) ~79.6 kA/m, f) the rate of change of magnetization (∂*M*/∂*T*) with *T* during the heating (red colored) and cooling (blue colored) cycles in first *MvT* run of the S56 powder, and g) Comparison of the percentage increase in *M* at *T*~300 K and *H* ~ 79.6 kA/m, before and after each *MvT* run—i.e., between the end and the beginning of the 1ˢᵗ *MvT* run (brown colored bars) and the between the end and the beginning of 2ⁿᵈ *MvT* run (orange colored bars)

Typically, an increase in temperature results in a decrease in magnetization due to the thermal effect on magnetic ordering (magnetic interaction with neighboring atoms) [30, 36, 42-43]. Figure 55 g shows the comparison of the % increase in the M at T~300 K at an applied magnetic field (H) ~ 79.6 kA/m in the as-received and milled powders for milling duration of 3 h, 5 h, 8 h, and 56 h, before and after each MvT run. The gradual decrease in the M of the as-received powder during the heating cycle in the 1st MvT run could be attributed as due to this effect. Similarly, during the cooling cycle, the magnetization value increased gradually with the decrease in temperature. The magnetization value increased by ~ 4% at the end of the 1st MvT run (when compared with the M at the end and the start of M at 300 K of the 1st MvT run). M of the 2nd MvT run followed a similar trend as the 1st MvT run with an increase in M of ~3% (when compared with the M at the end and the start of M at 300 K of the 2nd MvT run), and the thermomagnetic curve was reversible too. It is giving evidence that the as-received powder is stable up to ~ 900 K.

In the case of the milled powders, a decrease in the M with the effect of temperature is not only due to the effect of the magnetic ordering but also the relieving the residual stress induced during milling. A careful observation of the MvT curves reveals that the rate of decrease in the M during heating in the 1st MvT run of the milled samples was somewhat less (slower) than the rate of decrease in M during heating in the 2nd MvT run. This could be attributed by the differences in the residual stress in the milled samples, between the 1st and 2nd MvT runs. In the 1st MvT run, during heating, the thermal energy is used not only to relieve the residual stress induced during the milling process but also to influence the magnetic exchange interaction between the neighboring atoms. On the other hand, in the 2nd MvT run the powders are likely to have significantly lower residual stress compared to the powders in the 1st MvT run (as some amount of residual stress is relieved from the powder in the 1st MvT run by exposing it to elevated temperatures). Thus, the thermal energy expended during the 2nd MvT run is used to decrease the magnetic exchange interaction between the neighboring atoms and to relieve the unwanted residual stress in the powders. In the case of nanocrystalline milled maraging steel powders for a milling duration of 3 h, 5 h, and 8 h There was a significant increase in M by ~12% in these samples after the 1st MvT run, while the increase in M was by ~3% after the 2nd MvT run as shown inOn the other hand, in the milled powder for a duration of 56 h showed a different trend when compared to the nanocrystalline milled maraging steel powders with the exposure to temperature. This was expected due to the presence of extraneous phases of the precipitates. The rate of change of

magnetization (∂M/∂T) with T during the first M–T run was plotted to determine the inflection points and is shown in Figure 55 f. During the heating cycle, M gradually decreased with the increase in temperature until ~400 K followed with a steep decrease in M till ~650 K and reaching a minimum value of ~ 8 Am^2/kg (~750 K). After that, the M started to increase gradually and reached ~12 Am^2/kg at ~900 K. While in the cooling cycle, M gradually increased from ~ 900 K to ~650 K and showed a steep increase after ~ 650 K. The 2nd MvT run curve followed a similar trend as 1st MvT run showing the reversible behavior. This trend of a sudden decrease in the M in the region between ~ 400 – 750 K could be due to the formation of new phases or reverted austenite at that temperature regime during the heating cycle which results in the decrease in the magnetization. During the cooling cycle, the trend was reversible. There was a significant increase of ~ 13% in M after the 1st MvT run and ~ 5% after the 2nd MvT run.
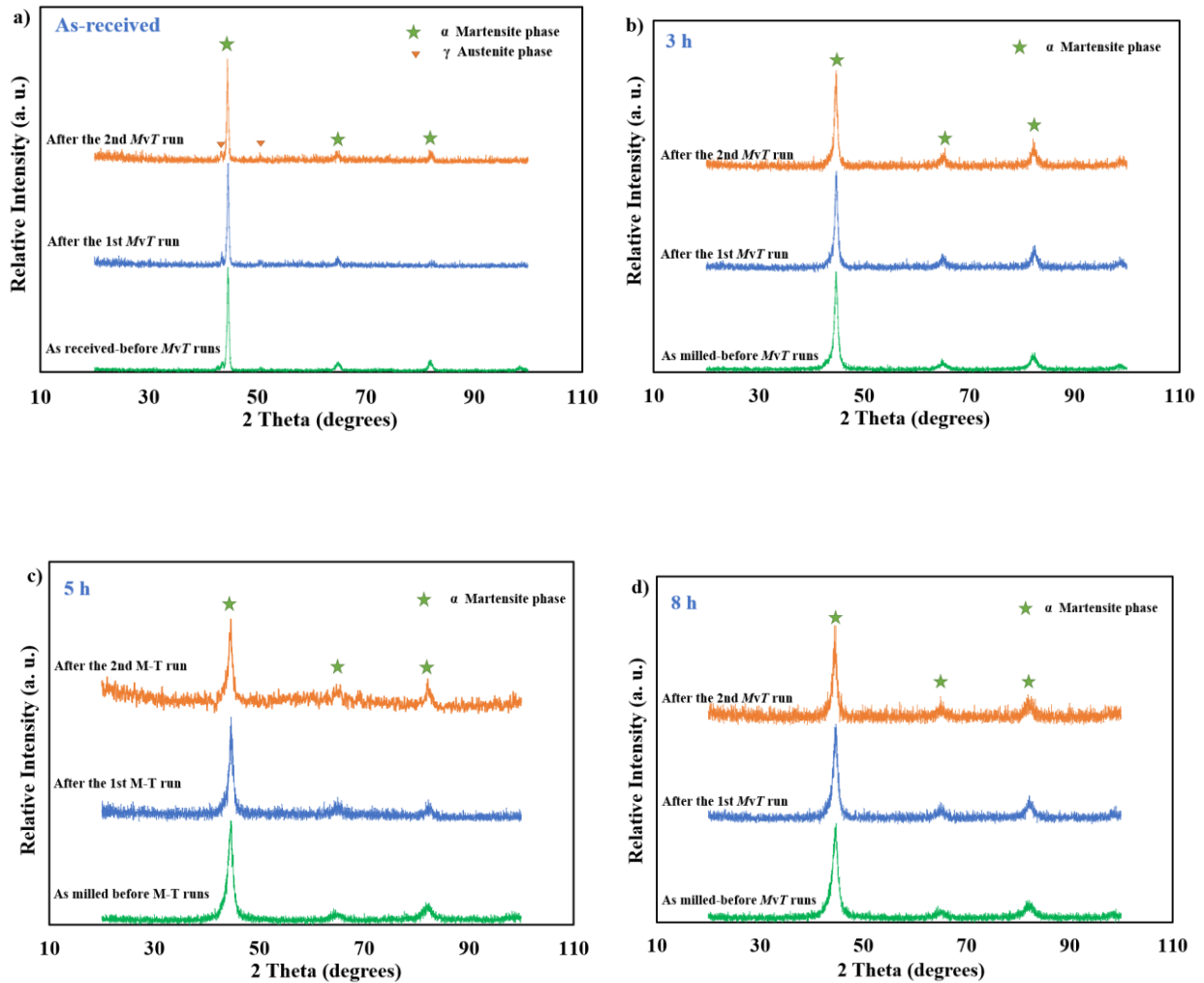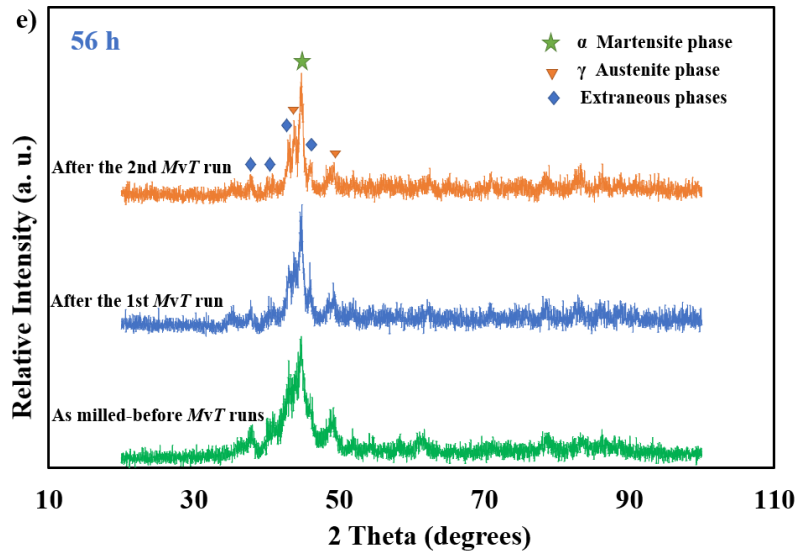
Figure 56 X-ray diffraction spectra of the a) as-received and the milled powders for milling duration of b) 3 h, c) 5 h, d) 8 h, and e) 56 h; before the *MvT* runs, after the 1st *MvT* run, and after the 2nd *MvT* run

Figures 56 a, 56 b, 56 c, 56 d, and 56 e show the comparison between the XRD spectra of the as-received and the milled powders for milling duration of 3 h, 5 h, 8 h, and 56 h respectively recorded at ambient temperature. From Figure 56 a, as-received powders even after the *MvT* runs show the presence of predominantly α- martensite phases and small traces of the γ-austenite phases similar to the XRD spectra of the as-received powders before the *MvT* runs. The nanocrystalline milled maraging steel powders (milled samples of 3 h, 5 h, and 8 h) from Figures 56 b, 56 c, and 56 d showed the presence of single phase (α- martensite phases) before and even after the *MvT* runs. The 56 h milled sample (Figure 56 e) showed the presence of a mixture of phases (α-martensite, γ-austenite, and some extraneous phases of intermetallic precipitates). No phase changes were observed in any of the samples. Qualitatively, from the XRD spectra of the milled samples (3h, 5h, 8h, and 56 h) the broadening of peak reduced after the *MvT* runs when compared to that of it before the *MvT* runs which could be attributed as due to the relieving of the residual stress during the *MvT* runs.

The as-received (S0) powder, nanocrystalline milled maraging steel (S5) milled for 5 h, and milled powder for 56 h (S56) was chosen to study the effect of elevated temperatures on their magnetic properties. The nanocrystalline milled maraging steel (S5) milled for 5 h was chosen as a representative of the nanocrystalline milled maraging steel powders because the M_S is similar to the other two milled samples and it has the lowest coercivity of ~4.9 kA/m among them. Milled

powder for 56 h (S56) was taken as a representative of the further milled samples more than a milling duration of 8 h — as the new phases were formed and their intensities increased with further milling.

The (*M*) versus (*H*) curves of these powders at different elevated temperatures are shown in Figure 57, and inset in each figure shows an enlarged view of the respective *M* vs *H* curves at a low magnetic field region of ± 10 kA/m.
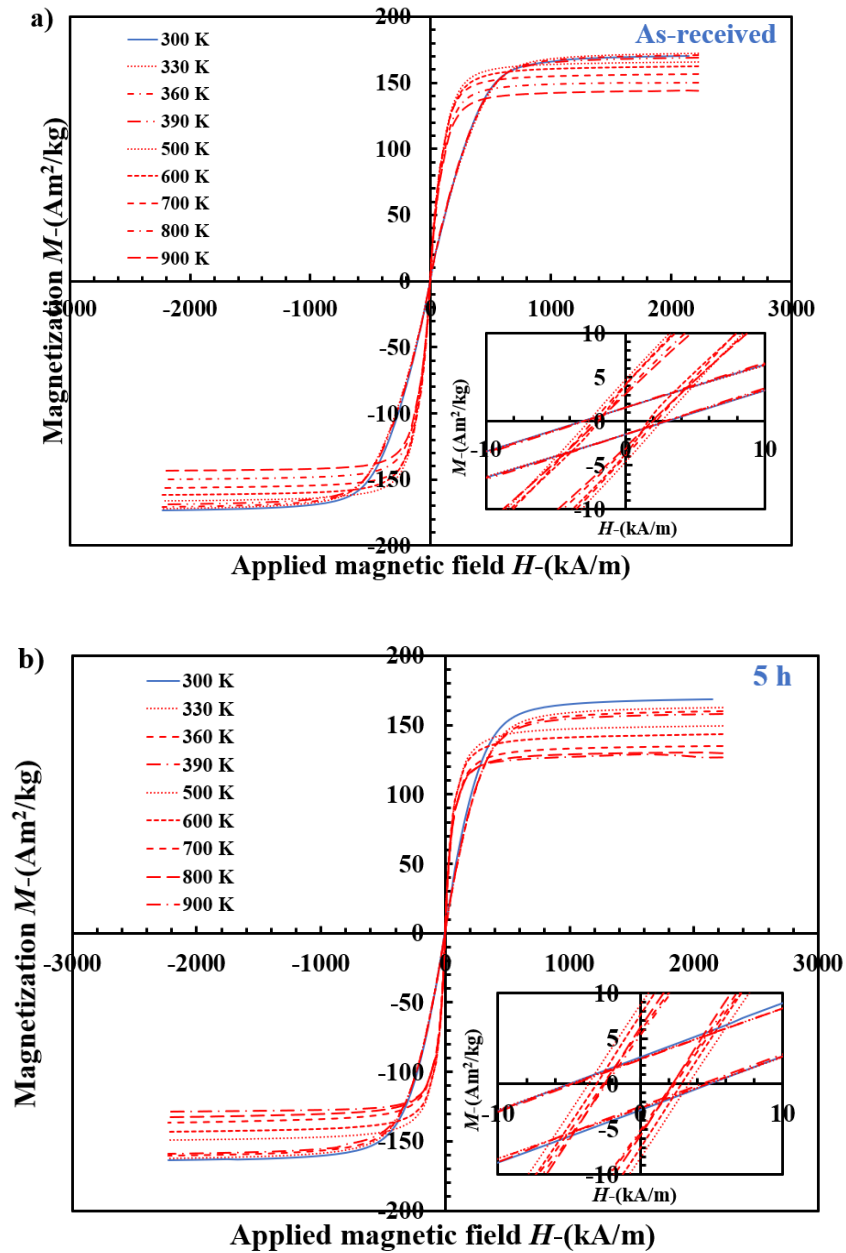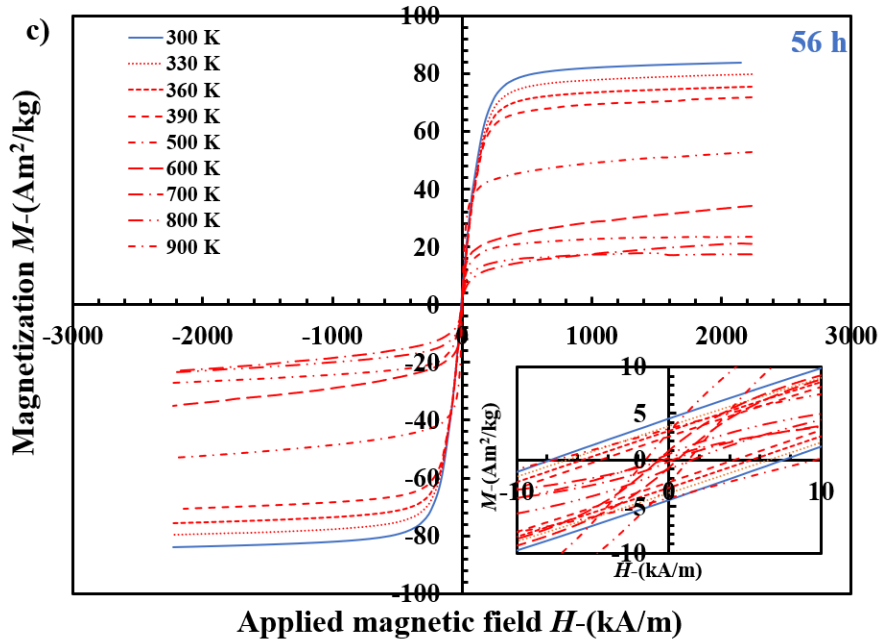
Figure 57 *M* versus *H* curves of the a) as-received (S0), milled samples for b) 5 h, and c) 56 h at elevated temperatures. *M* versus *H* curves of these powders at ambient temperature are included as a reference, and the inset shows the curves at a low-magnetic-field region (± 10 kA/m)

M_S and H_{CI} of these samples at elevated temperatures were estimated from the plotted *MvH* curves from the Figure 57 as explained earlier (M_S – by using Law of approach to saturation and H_{CI} – by averaging the intercepts from the hysteresis loops). The accurate M_R cannot be estimated from the *M*) versus (*H*) curves due to the presence of copper foil surrounding the powders. Thus, only M_S and H_{CI} were estimated. The variation with temperature in M_S and H_{CI} of these samples are shown in Figure 58. There was a gradual decrease in M_S with an increase in temperature for both as-received and milled powder for 5 hours. The M_S of the as-received sample decreased from ~176.15 Am^2/kg (300 K) to ~ 143.21 Am^2/kg (900 K) i.e., by ~19 %. While the M_S of the milled powder for 5 h decreased from ~165.31 Am^2/kg (300 K) to ~ 128.4 Am^2/kg (900 K) i.e., by ~22 %. The decrease in M_S can be attributed as the effect of temperature on the magnetic ordering (interaction with neighboring atoms). Additionally, for the milled sample of S5, the decrease is also because of the temperature in the relieving the residual stress induced during milling. Unlikely as the other two samples, the S56 sample followed a different trend in M_S at elevated temperatures. The M_S decreased gradually from ~83 Am^2/kg (300 K) to ~70.36 Am^2/kg till ~400 K. After 400 K, there was a steep decrease in M_S and it reached a minimum of 21.37 Am^2/kg at ~ 700 K and started to increase gradually to ~26 Am^2/kg at 900 K. This trend of the powders matches with the

82

*M*v*T* even though the powders are maintained at elevated temperature for a longer duration of ~ 1 h.

Similarly, H_{CI} also decreased with the increase in temperature in the case of S0 & S5. H_{CI} decreased by ~ 1.5 times i.e., from ~3 kA/m (300 K) to ~1.97 kA/m (900 K) for S0 and For S5, H_{CI} decreased by ~2 times i.e., from ~4.9 kA/m (300 K) to ~ 2.3 kA/m (900 K). The decrease in H_{CI} in S0 can be attributed probably the influence of temperature causing the increase in the grain size of the sample. In the S5 sample, the decrease in the H_{CI} is most likely due to the effect of a decrease in the lattice strain induced during the milling process and along with the increase in the grain size. While in the case of S56, H_{CI} decreased gradually from ~7.6 kA/m at 300 K and reached a minimum of ~ 0.6 kA/m at 700 K. After that, H_{CI} increased and reached a maximum of ~9 kA/m at ~900 K. The initial decrease in H_{CI} till 700 K suggests that could be due to the increase in the grain size and decrease in the lattice strain induced during the milling process. The steep decrease and increase in H_{CI} can also be possible because of the formation of either new phases or existing phases which tend to follow this trend at that particular temperature. These can be evaluated by using an in-situ high-temperature XRD and in-situ TEM studies at elevated temperatures. This will help to understand any new phase transformation or disappearance of an existing phase causing at elevated temperatures.
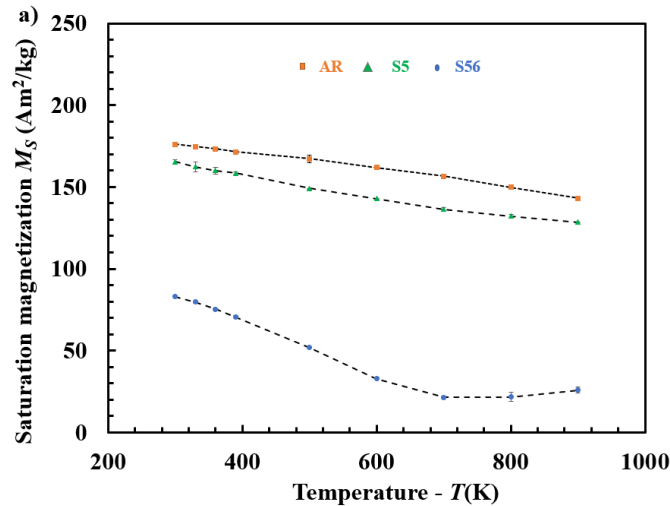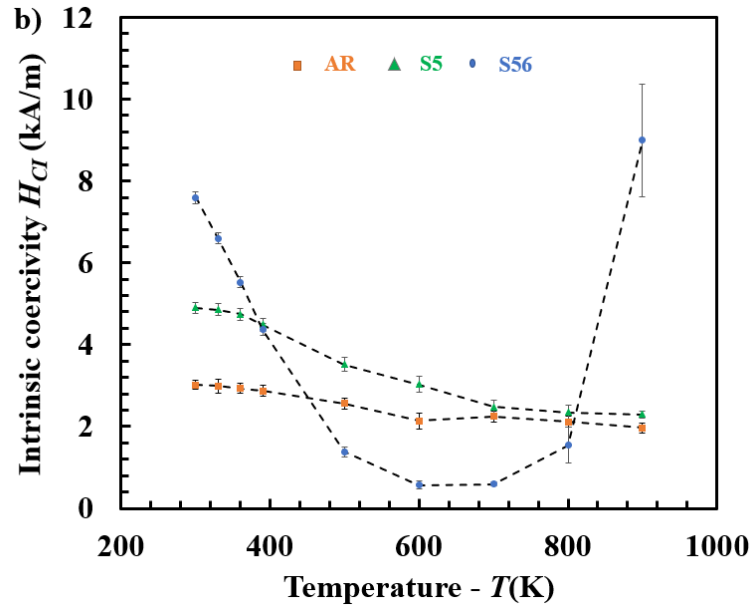
Figure 58 The variation of a) M_S and b) H_{CI} with elevated temperatures (T) of the as-received (S0) powder, milled powders of S5, and S56

5.5 Magnetic properties of thermally treated powders

X-ray diffraction was performed at ambient temperature on the thermally treated powders in order to understand the influence of elevated temperatures. X-ray diffraction spectra were recorded for the thermally treated powders exposed at different elevated temperatures (330-900 K) for ~1 h during the generation of MvH curves followed by cooling to ambient temperature at 15 K/min. XRD spectra of the thermally treated powders were stacked above other to have a qualitative representation of the changes of that particular powder with the increase in temperature. The as-received and the as-milled x-ray diffraction spectra of the powders were also included as a reference to understand the phase changes. Figure 59 a, 59 b, and 59 c represents the x-ray diffraction spectra of the thermally treated S0, S5, and S56 samples at 300 K respectively.
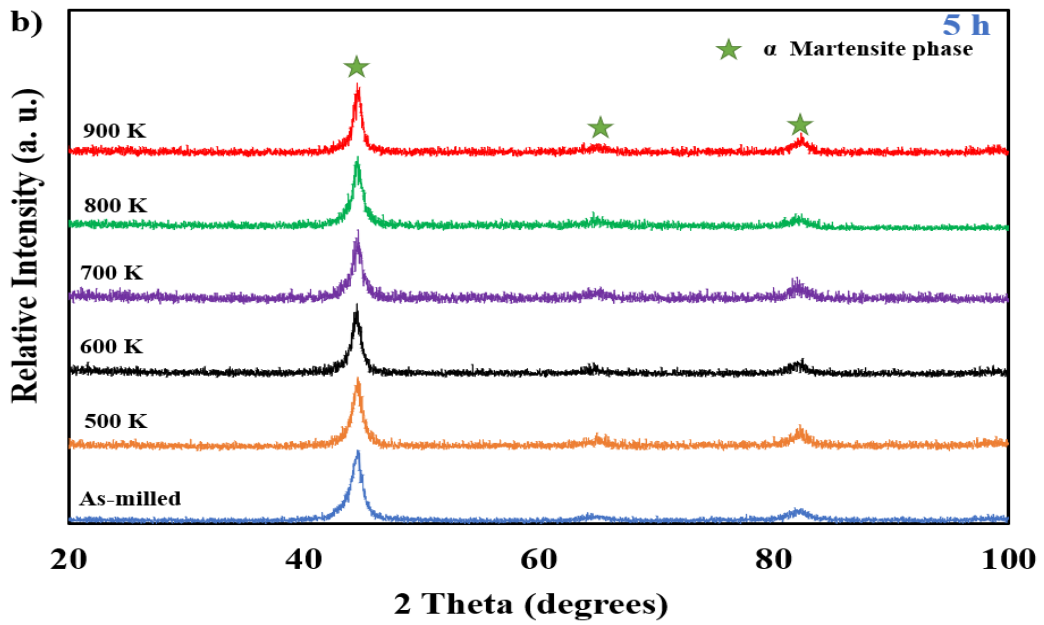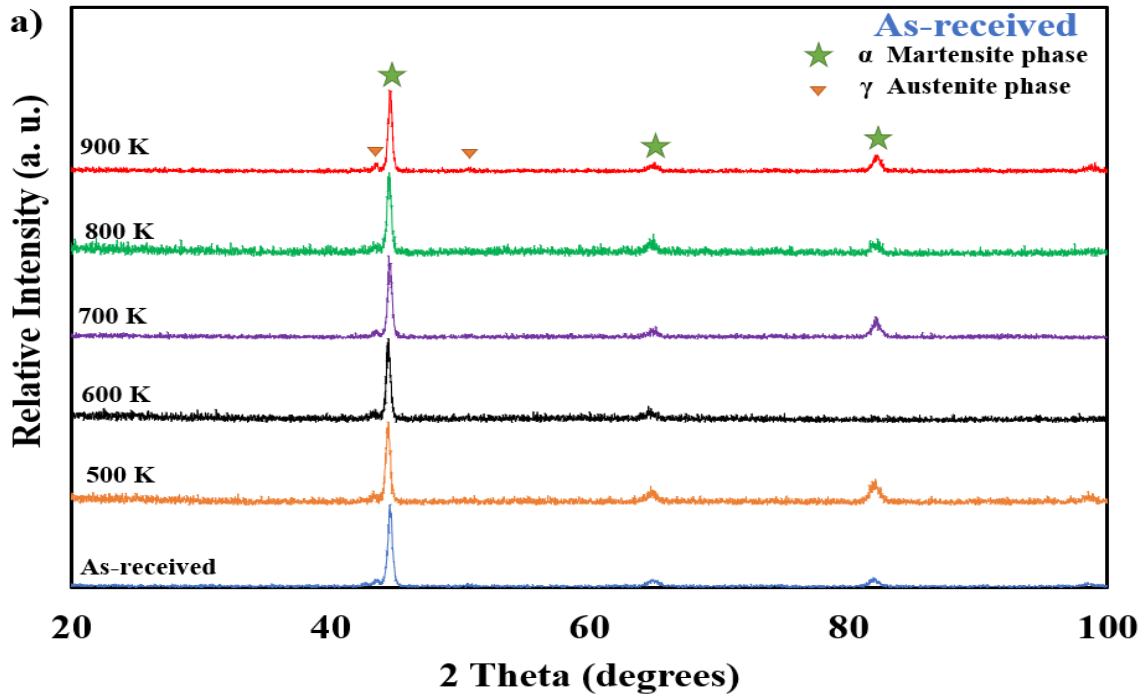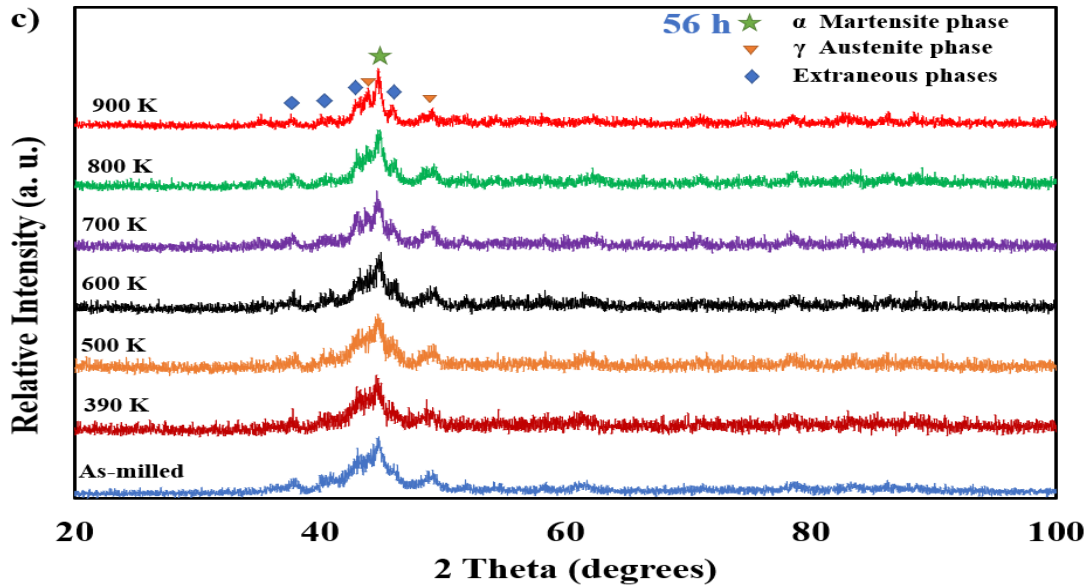
Figure 59 X-ray diffraction spectra at 300 K, of the thermally treated samples— a) S0, b) S5, and c) S56; X-ray diffraction spectra of each powder at 300 K is also included as a reference

Figure 59 a shows the XRD spectra recorded at room temperature of the thermally treated as-received powders exposed at elevated temperatures. Even when exposed to elevated temperatures as high as ~900 K, is comprised of predominantly martensite phase (α) and small traces of the austenite (γ) phase and is same as the as-received powder. Formation of new peaks or transformation of (α- γ) is not observed in the XRD spectra. Thus, it is evident that the phases are stable even up to an elevated temperature of 900 K. Similarly, in the case of the S5 sample (as in Figure 59 b), it comprised of single martensite (α) phase even after exposure to the elevated temperatures, same as the as-milled powder. No traces of new phases were observed from the XRD spectra when exposed to elevated temperatures in the nanocrystalline milled sample. Thus it can be concluded as the S5 sample is also stable up to an elevated temperature of 900K. Qualitatively, it can be seen that the broadening of the peak reduced with an increase in the elevated temperatures suggesting that the thermal energy is utilized to relieve the residual stress induced during milling. Figure 59 c shows the XRD spectra recorded at room temperature of the thermally treated milled powder for 56 h exposed at elevated temperatures. The emergence of new phases or disappearance of any existing phase was not observed. Similar to the S5 sample, qualitatively the broadening of the peak reduced with an increase in the elevated temperatures suggesting that the thermal energy is utilized to relieve the residual stress induced during milling.
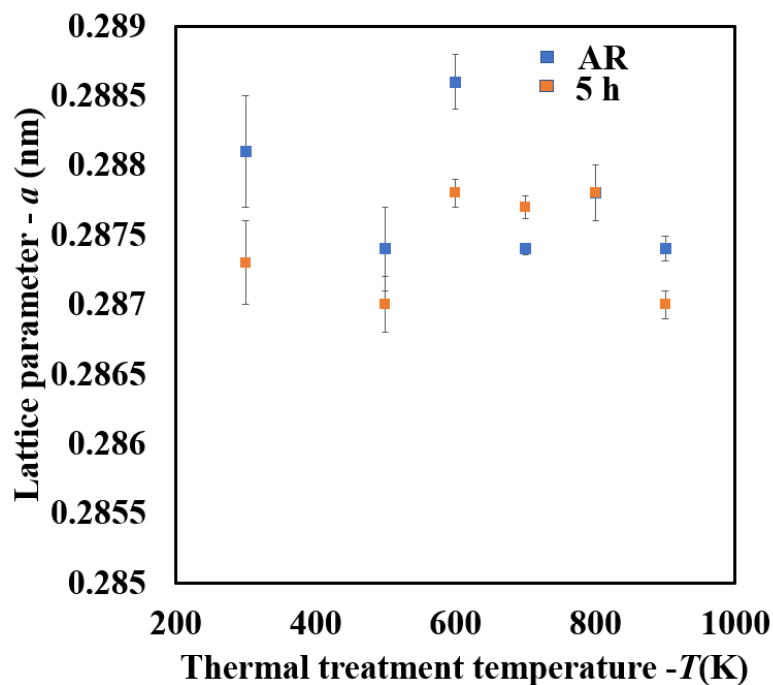
Figure 60 The lattice parameter with the thermal treatment temperature (900 K) of the as-received powder and the milled powder for 5 h

The lattice parameter with the thermal treatment temperature of the as-received powder and the milled powder for 5 h was estimated and represented in Figure 60. The lattice parameter of both the thermally treated as-received and the milled powder for 5 h showed a minimal change. The lattice parameter of the milled powder for 56 h cannot be determined from the XRD spectra because of the nearby peaks of the extraneous phases. The grain size of the thermally treated powders was estimated, and it tends to increase with the increase in thermal treatment temperature. The milled powder for 5 h remained nanocrystalline even after thermal treatment till 900 K.
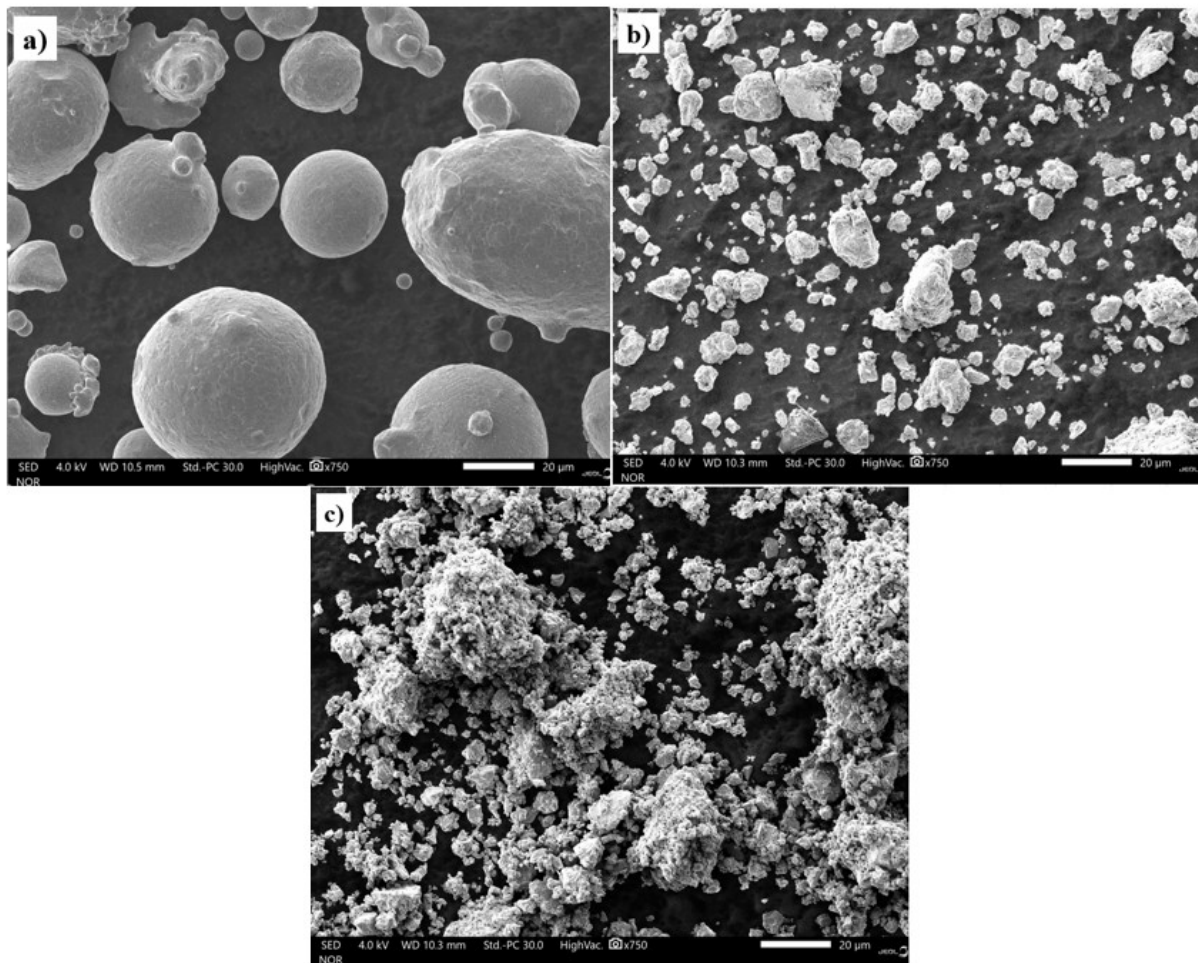
Figure 61 Scanning electron micrographs at ambient temperature of the thermally treated at ~900 K — a) as-received powder(S0) and milled powders b) 5 h and c) 56 h respectively, at a magnification of ~750 X

Figure 61 a, b, and c show the scanning electron micrographs at ambient temperature of the thermally treated at ~900 K — a) as-received powder(*S0*) and milled powders b) 5 h and c) 56 h respectively, at a magnification of ~750 X. The particle size is expected to increase with the thermal treatment. Qualitatively it appears that the particle size increased when compared with the as-milled powders. The particle size D_{90} of the thermally treated powders at ~900 K increased to ~33μm (i.e., increased by ~ 1.5 times) for the as-received powder, ~ 6.5 μm (decreased by ~ 1.3 times) for the 5 h milled powder, and ~ 7.5 μm (i.e., increased by ~ 1.3 times)for the 56 h milled powder. The reason for the decrease in the particle size of the milled powder for 5 h is because of the number of particles in the SEM image are low when compared to the as-milled powder of 5 h.

The (*M*) versus (*H*) curves were plotted for the thermally treated samples of S0, S5, and S56 (exposed at elevated temperatures) at ambient temperatures, as shown in Figure 63 and inset in each figure shows an enlarged view of the respective *MvH* curves at a low magnetic field region of ± 10 kA/m. *MvH* curves of the as-received and the as-milled powders were also included as a reference to understand the variation in the magnetic properties with thermal treatment at elevated temperatures.
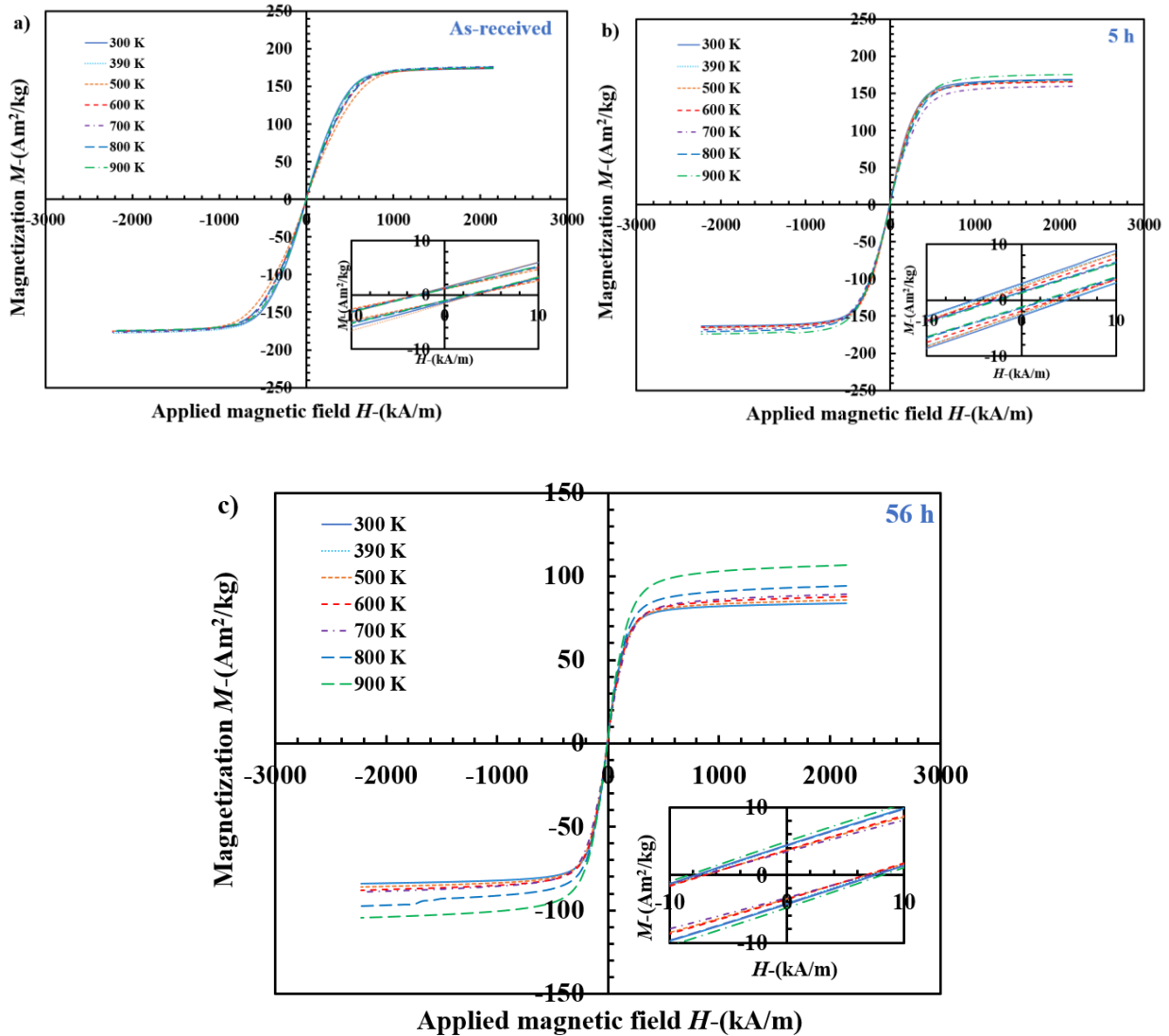
Figure 62 *MvH* curves of the thermally treated as-received (*S0*), milled powders for the milling duration of 5 h (S5), and 56 h (S56); at ambient temperatures (after the *MvH* runs at elevated temperatures). Inset in each figure shows the curve at a low-magnetic-field region (±10 kA/m). *MvH* curves of the as-received and the as-milled powder was also included as a reference

89

The M_S, H_{CI}, and M_R of the as-received and the as-milled powders, at ambient temperature, after their respective MvH curves at elevated temperatures were estimated from the Figure 62 as explained earlier (M_S – by using Law of approach to saturation and H_{CI}, and M_R – by averaging the intercepts from the hysteresis loops). The M_S of the as-received powder Figure 63 a thermally treated at ~500 K -900 K varied within the range of ~177±0.4 Am^2/kg – 179.5±1.0 Am^2/kg. There was a very minimal increase in M_S when compared to the as-received powder at ambient temperature, which is negligible. Thus, similar M_S can be achieved in these powders even after thermally treating them to high temperature as ~900 K for approximately 1 h. In the case of the milled powder for a duration of 5h, the M_S maintained nearly similar values to the as-milled powder at ambient temperature till 700 K. The M_S increased to ~ 171 Am^2/kg and ~ 174 Am^2/kg at 800 K and 900 K (by ~5% when compared to as milled powder). While in the milled powder of 56 h, there was a gradual increase in the M_S till 700 K (~88 Am^2/kg) i.e., by ~ 7% when compared to the as-milled powder at ambient temperature. It increased by ~14 % (95 Am^2/kg) and ~19% (105 Am^2/kg) at 800 K and 900 K respectively.
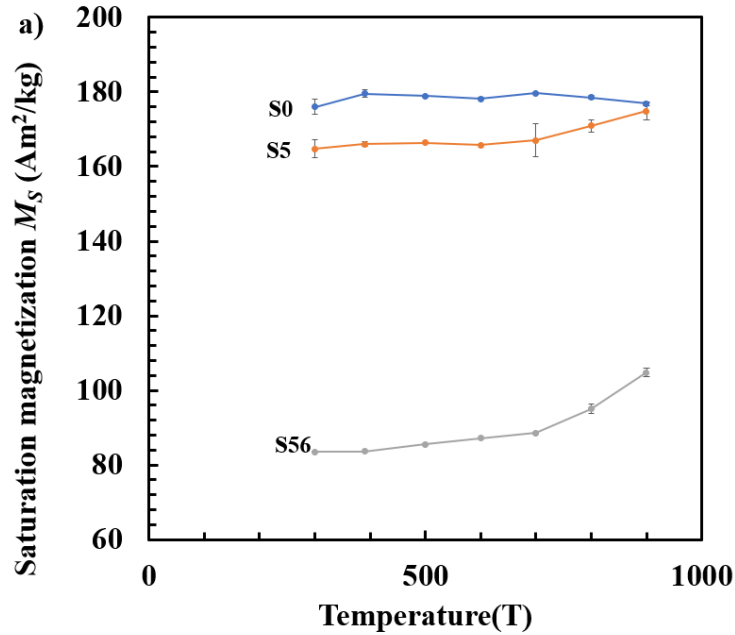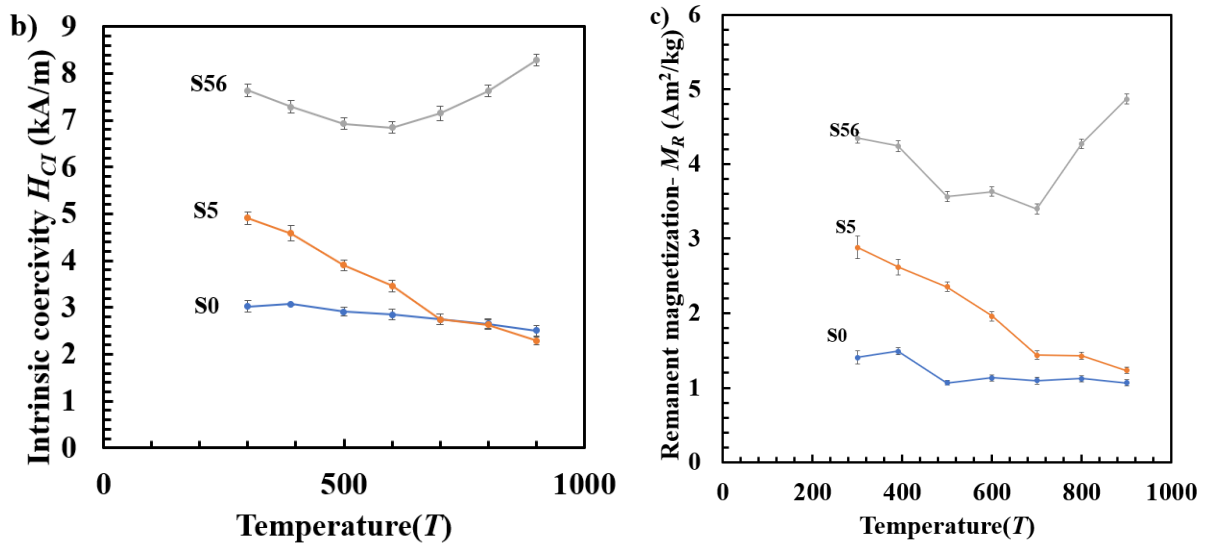
Figure 63 The variation of a) M_S, b) H_{CI}, and c) M_R with thermal treatment temperature of the as-received (S0) powder, milled powders of S5, and S56 at ambient temperature (300 K)

The H_{CI}, and M_R of the as-received and the as-milled powders, at ambient temperature, after their respective MvH curves at elevated temperatures followed a similar trend. The H_{CI} and M_R of the as-received and the milled powder for 5 h showed a gradual decrease with the increase in the thermal treatment temperature. The decrease in H_{CI}, and M_R of the as-received powder at thermal treatment temperature of 900 K when compared to that at ambient temperature was ~1.2 times (3.0 kA/m at 300 K to 2.5 kA/m at 900 K) and ~1.4 times (1.4 Am²/kg at 300 K to 1.0 Am²/kg at 900 K) respectively. In the case of milled powder of 5 h, the decrease in H_{CI}, and M_R was ~ 2.1 times (4.91 kA/m at 300 K to 2.29 kA/m at 900 K) and ~2.4 times (2.9 Am²/kg at 300 K to 1.2 Am²/kg at 900 K) respectively. While in the case of milled powder for 56 h showed a gradual decrease in the H_{CI} till 600 K i.e., from ~7.6 kA/m at 300 K to ~6.8 kA/m at 600 K. It increased and reached a maximum of 8.3 kA/m at 900 K. M_R also followed a similar pattern, it initially gradually decreased and reached a minimum of ~3.4 Am²/kg at 700 K and it reached a maximum of ~ 4.9 Am²/kg at 900 K.

Finally, even after thermally treating the as-received powder at 900 K for ~ 1 h there was no significant increase in the M_S, while the H_{CI}, and M_R decreased showing the better magnetic properties. So, these powders can be reused even after thermally treating them. In the case of the milled powder for 5 h, the M_S had a significant increase in the range of ~800-900 K reaching the M_S nearly equal to the as receive powder. Simultaneously, the H_{CI}, and M_R decreased by ~2 times

at 900 K when compared with the as-milled powder for 5h. Hence, it can be implied that mechanical milling the pre-alloyed gas atomized powder for a shorter duration ~ 5h followed by thermal treatment ~ 800-900 K exhibited similar magnetic properties as the as-received and additionally being nanocrystalline and being single martensite phase.

The (*M*) versus (*H*) curves were plotted for the thermally treated as-received powder (exposed at elevated temperatures) at ambient temperatures, as shown in **Figure 64** and inset in each figure shows an enlarged view of the respective *M*v*H* curves at a low magnetic field region of ± 10 kA/m.
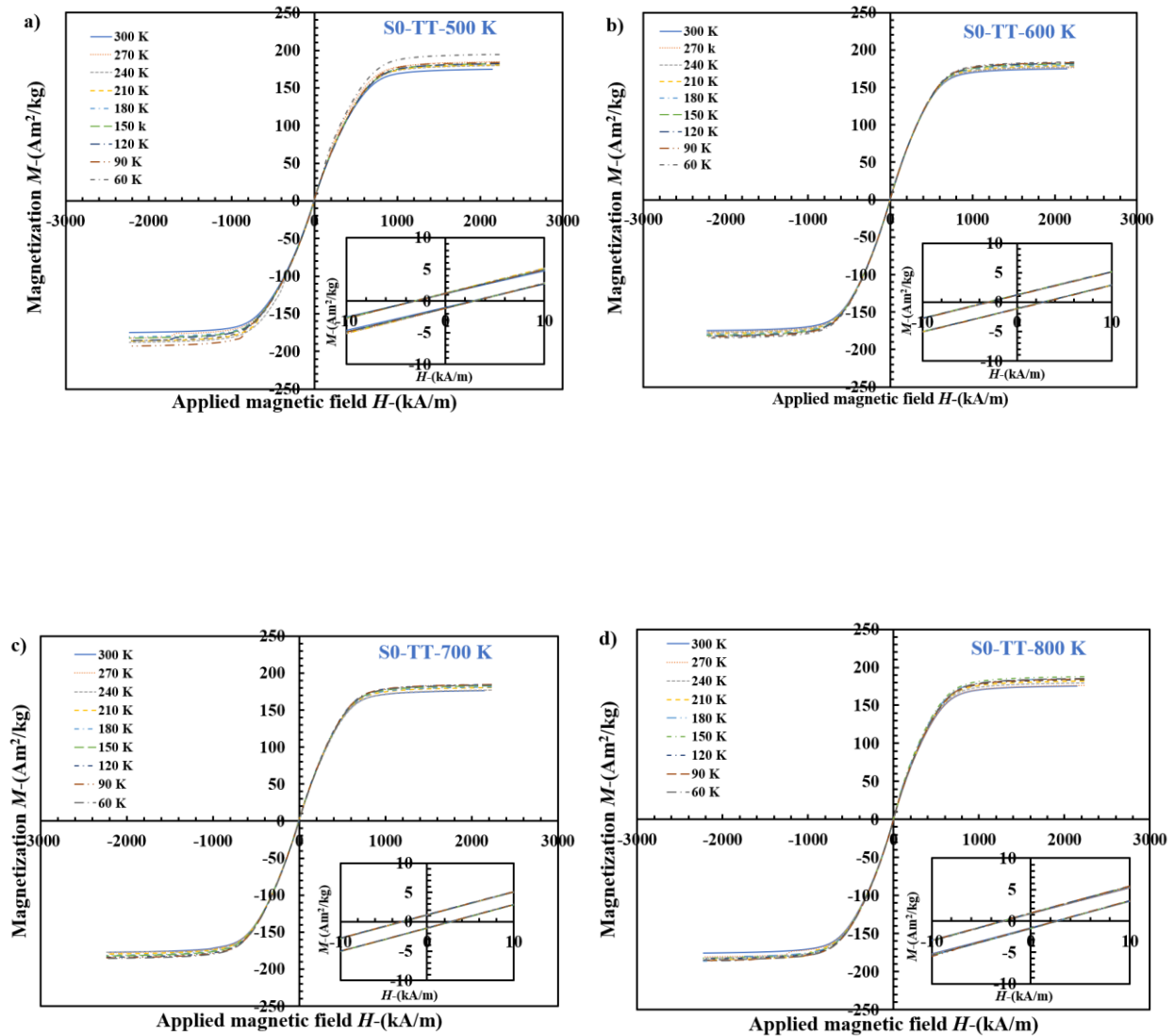
Figure 64 *MvH* curves of the pre-alloyed gas atomized (S0) thermally treated at a) 500 K, b) 600 K, c) 700 K, d) 800 K, and e) 900 K; at sub-ambient temperatures (60 - 300 K). Inset in each figure shows the curve at a low-magnetic-field region (±10 kA/m)

M_S, H_{CI}, and M_R at sub-ambient temperatures of the thermally treated powders at different elevated temperatures were estimated from their respective sub-ambient *MvH* curves. The variation of M_S, H_{CI}, and M_R for the thermally treated as-received (S0) powder at sub-ambient temperatures concerning the temperature are shown in Figure 65 a, 65 b, and 65 c. An increase in M_S was observed in all the thermally treated samples with a decrease in temperature, irrespective of temperatures the sample was exposed. M_S increased gradually by ~5% at ~60 K when compared to that of the thermally treated powder at ambient temperature for all the thermally treated as-received powders. The observed experimental results from the above *MvH* curves were fitted with equation (5) (Bloch's Law), and M_S (0) was estimated. The M_S (0) of the thermally treated as-received (S0) powders exposed to elevated temperatures was estimated to be in the range between ~186 Am²/kg to ~ 193 Am²/kg. The values of constant A are shown in the figure 65 a below.

a)

Saturation magnetization M_s (Am^2/kg)

TT-500 K=193.03[1−(1.1×10^{-5}) $T^{3/2}$]
TT-600 K=188.65[1−(1.1×10^{-5}) $T^{3/2}$]
TT-700 K=189.57[1−(1.1×10^{-5}) $T^{3/2}$]
TT-800 K=190.49[1−(9.8×10^{-6}) $T^{3/2}$]
TT-900 K=186.20[1−(1.0×10^{-5}) $T^{3/2}$]

Temperature - T(K)

b)

Intrinsic coercivity H_{CI} (kA/m)

TT-500 K = -8E-06T^2 + 0.0026T + 2.8239;R^2 = 0.5843
TT-600 K = -4E-06T^2 + 0.0011T + 2.8451;R^2 = 0.9836
TT- 700 K = -4E-06T^2 + 0.0014x + 2.7099;R^2 = 0.9638
TT-800 K = -5E-06T^2 + 0.0016T + 2.6134;R^2 = 0.9122
TT- 900 K = -4E-06T^2 + 0.0015T + 2.3992;R^2 = 0.9008

Temperature - T(K)

c)

Remanent magnetization M_R (Am²/kg)

TT- 500 K = $-5E-06T^2 + 0.0016T + 1.0437$; $R^2 = 0.4689$
TT- 600 K = $-2E-06T^2 + 0.0005T + 1.1245$; $R^2 = 0.994$
TT- 700 K = $-2E-06T^2 + 0.0005T + 1.0879$; $R^2 = 0.9897$
TT- 800 K = $-4E-06T^2 + 0.0012T + 1.1198$; $R^2 = 0.9548$
TT- 900 K = $-1E-06T^2 + 0.0005T + 1.0376$; $R^2 = 0.9146$

Temperature - T(K)

Figure 65 Variation of a) saturation magnetization (M_S) and b) intrinsic coercivity (H_{CI}), and remanent magnetization (M_R) with temperature (T) of the thermally treated (500-900 K) S0 sample, at sub-ambient temperatures (60 - 300 K)

The variations in the H_{CI} and M_R of these powders were estimated from the respective MvH curves. H_{CI} and M_R had a negligible change of less than ~2% with an increase in temperature, irrespective of the thermal treatment temperature. These trends fit quadratically, and their values at absolute 0 K can be found by extrapolating the respective quadratic curves to absolute 0 K. The H_{CI} (0) and M_R (0) of these powders are in the range between ~2.4 to ~2.8 kA/m and in between ~1.0 to 1.1 Am²/kg, respectively.

Similarly, (M) versus (H) curves were plotted for the thermally treated powders of S5 (exposed at elevated temperatures) at ambient temperatures, as shown in Figure 66 and inset in each figure shows an enlarged view of the respective MvH curves at a low magnetic field region of $\pm$ 10 kA/m.
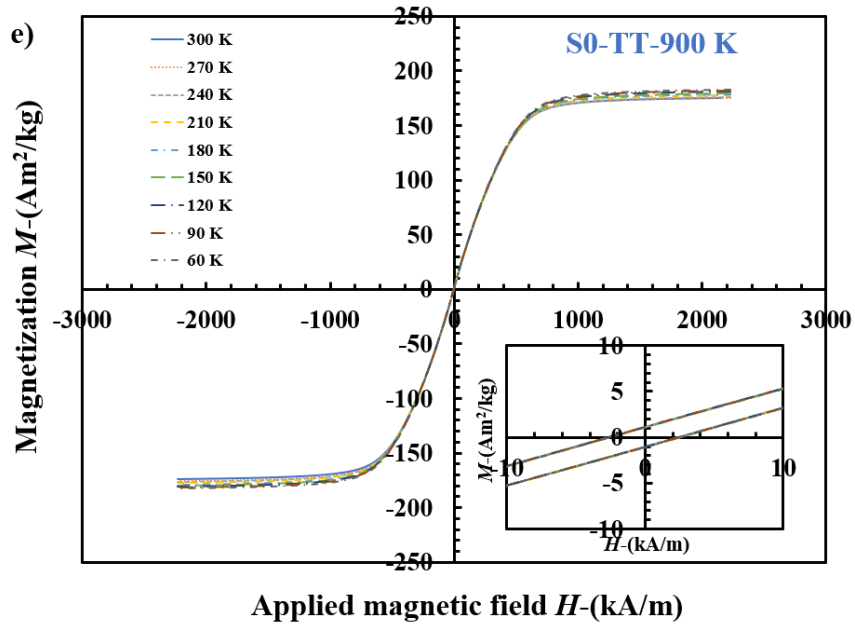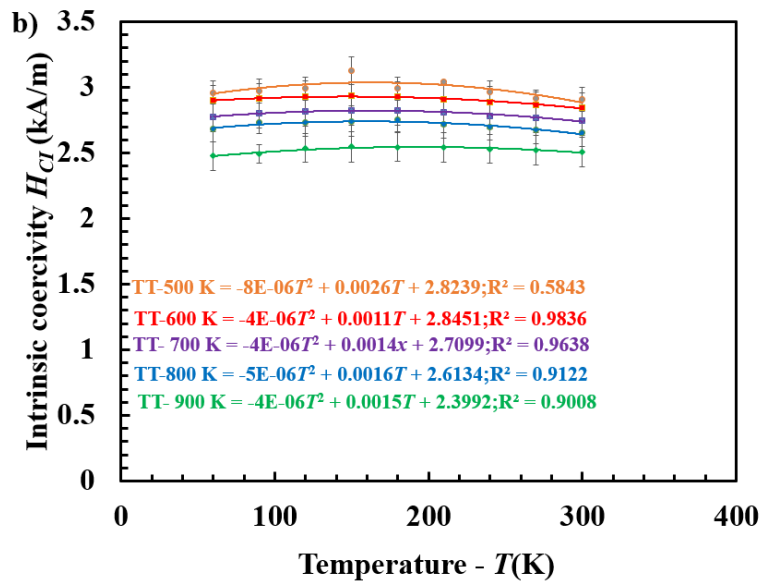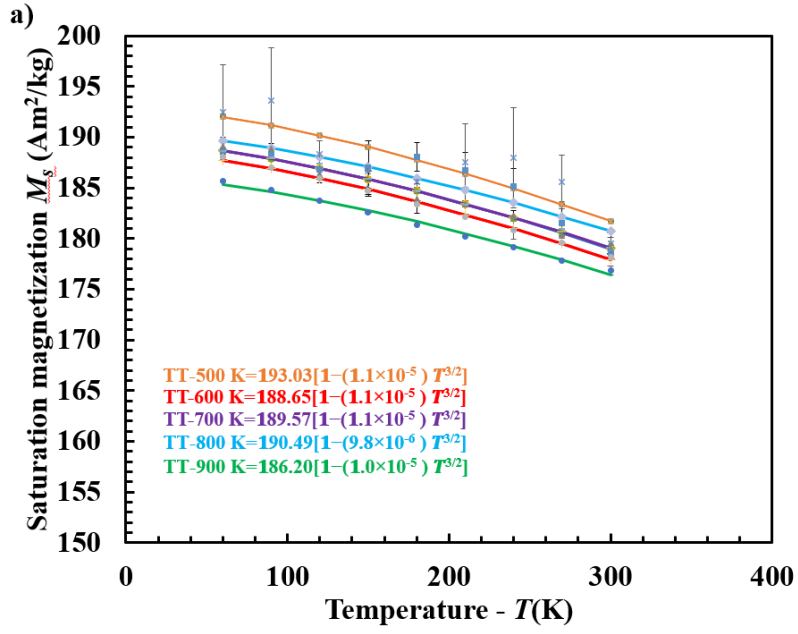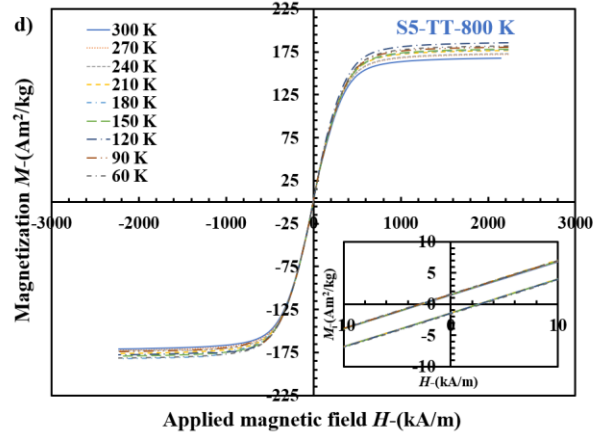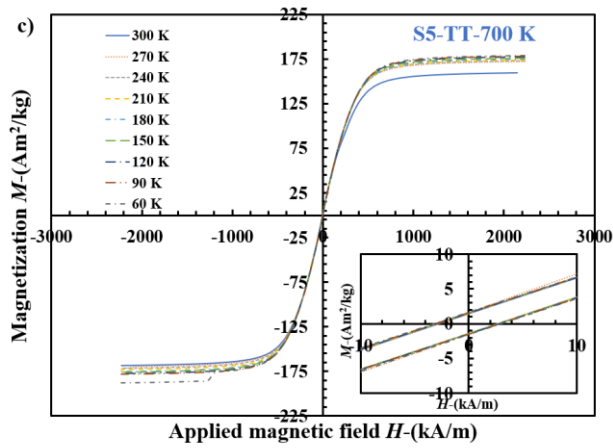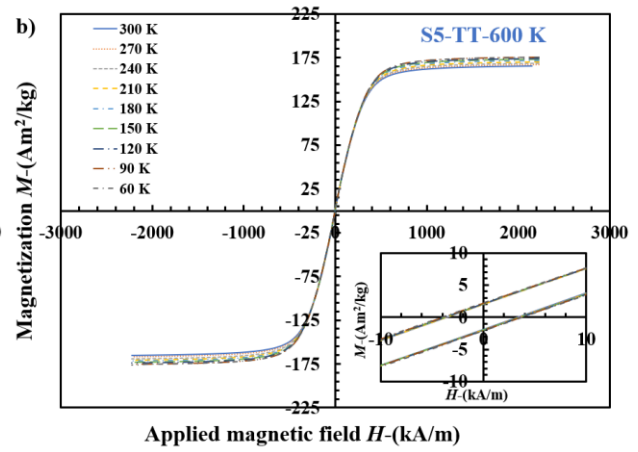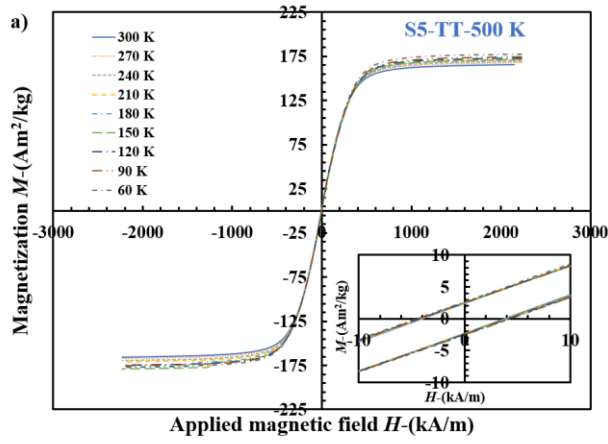
Figure 66 *MvH* curves of the milled (S5) sample thermally treated at a) 500 K, b) 600 K, c) 700 K, d) 800 K, and e) 900 K; at sub-ambient temperatures (60 - 300 K). Inset in each figure shows the curve at a low-magnetic-field region (± 10 kA/m)

The variation of M_S, H_{CI}, and M_R for the thermally treated S5 powders at sub-ambient temperatures concerning the temperature are shown in Figure 67 a, 67 b, and 67 c. M_S increased with a decrease in temperature in all the thermally treated samples, irrespective of thermal treatment temperatures. M_S increased gradually by ~7-9% at ~60 K when compared to that of the thermally treated sample at ambient temperature for the thermally treated powders. The observed experimental results were fitted with equation (5) (Bloch's Law), and $M_S(0)$ was estimated. The $M_S(0)$ was estimated to be in the range between ~179 Am^2/kg to ~ 191 Am^2/kg, as shown in figure 67 a. The $M_S(0)$ exhibited a trend of an increase in its value with the increase in thermal treatment temperature.

a)

TT-500 K=**179.13**[**1**−(**1.3×10⁻⁵**) $T^{3/2}$]
TT-600 K=**178.2**[**1**−(**1.3×10⁻⁵**) $T^{3/2}$]
TT-700 K=**184.13**[**1**−(**1.6×10⁻⁵**) $T^{3/2}$]
TT-800 K=**183.77**[**1**−(**1.2×10⁻⁵**) $T^{3/2}$]
TT-900 K=**191.16**[**1**−(**1.4×10⁻⁵**) $T^{3/2}$]

b)

TT- 500 K = **5E-06**T^2 − **0.004**T + **4.6282**;R² = **0.9634**
TT- 600 K = **7E-06**T^2 − **0.0042**T + **4.1269**;R² = **0.9916**
TT-700 K = **1E-05**T^2 − **0.0046**T + **3.3225**;R² = **0.8028**
TT- 800 K = **6E-06**T^2 − **0.0036**T + **3.1297**;R² = **0.9519**
TT- 900 K = **4E-06**T^2 − **0.0019**T + **2.5245**;R² = **0.9671**

c)

TT- 500 K = $5\text{E-}06T^2 - 0.0029T + 2.7521; R^2 = 0.9881$

TT- 600 K = $4\text{E-}06T^2 - 0.0022T + 2.2812; R^2 = 0.9873$

TT-700 K = $5\text{E-}06T^2 - 0.0022T + 1.7092; R^2 = 0.656$

TT- 800 K = $3\text{E-}06T^2 - 0.0017T + 1.6928; R^2 = 0.9522$

TT- 900 K = $2\text{E-}06T^2 - 0.0009T + 1.3349; R^2 = 0.8068$

Figure 67 Variation of a) saturation magnetization (M_S) and b) intrinsic coercivity (H_{CI}), and remanent magnetization (M_R) with temperature (T) of the thermally treated (500-900 K) milled powder for 5h (S5), at sub-ambient temperatures (60 - 300 K)

H_{CI} and M_R increased gradually with the decrease in temperature, irrespective of the thermal treatment temperature. The trend of the H_{CI} and M_R of these powders was fitted using a polynomial equation of order 2, and the equations are shown in figure 67 b and 67 c. The $H_{CI}(0)$ was estimated to be in the range between ~4.63kA/m (500 K) to ~2.52 kA/m (900 K). $M_R(0)$ was estimated to be in the range of ~2.75 Am²/kg (500 K) to ~1.34 Am²/kg (900 K). Contrarily to the trend of $M_S(0)$, $H_{CI}(0)$ and $M_R(0)$ followed a trend of decrease in their value with the increase in thermal treatment temperature.

Similarly like the thermally treated powders of S0, and S5— (M) versus (H) curves were plotted for the thermally treated powders of S56 (exposed at elevated temperatures) at ambient temperatures, as shown in Figure 68 and inset in each figure shows an enlarged view of the respective MvH curves at a low magnetic field region of ± 10 kA/m.
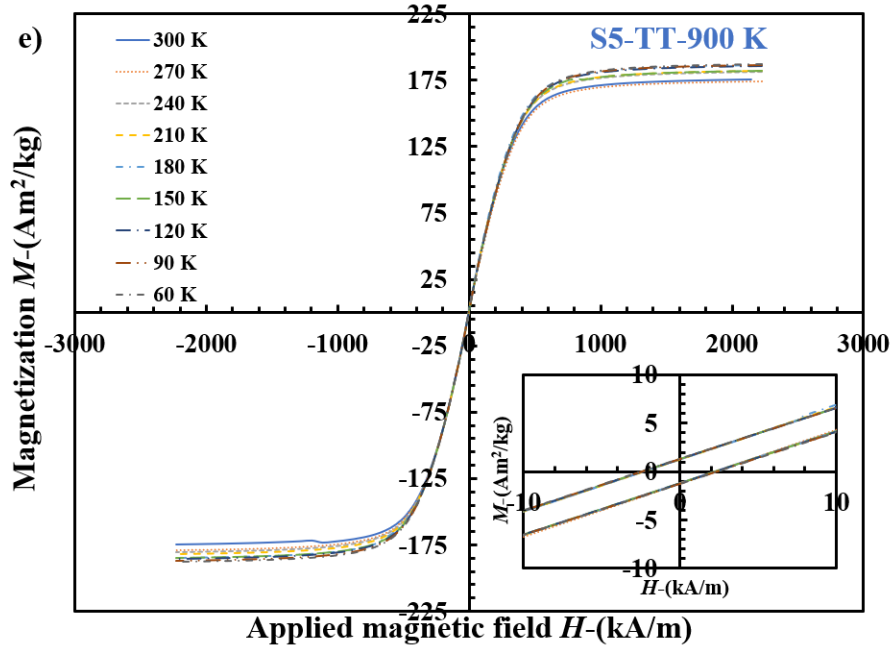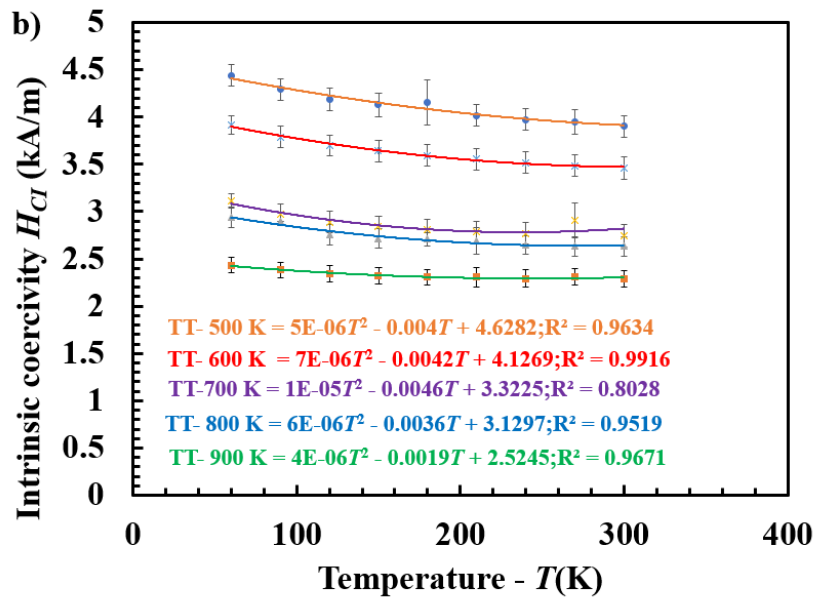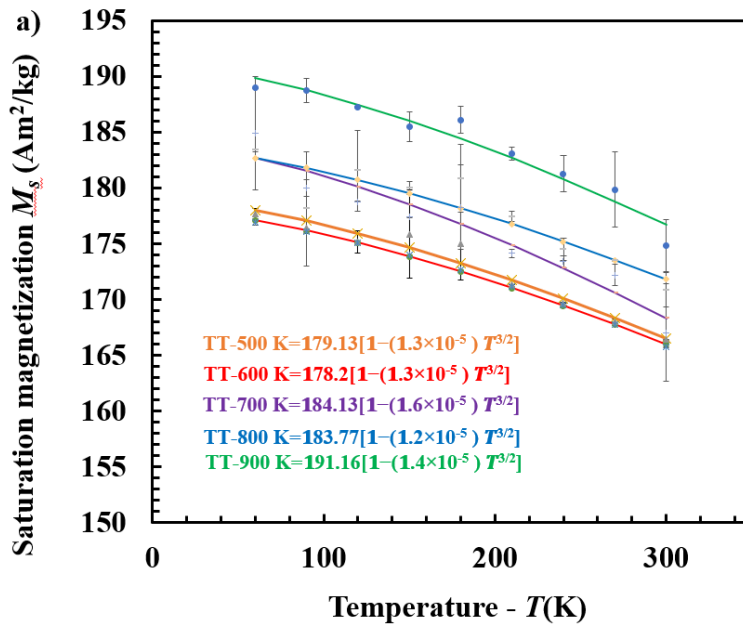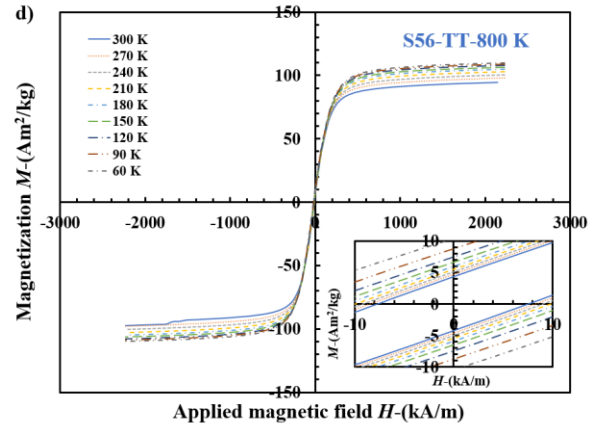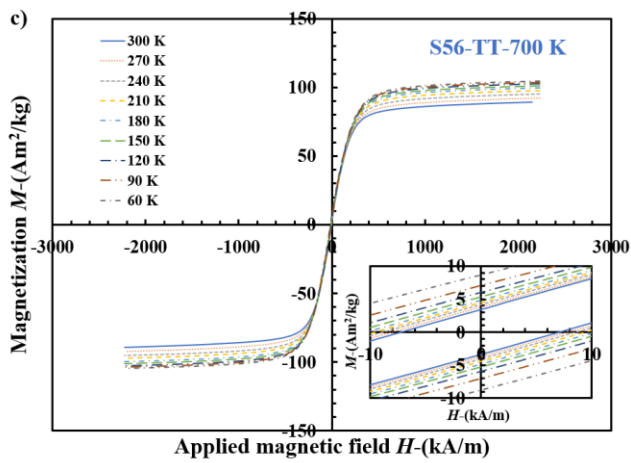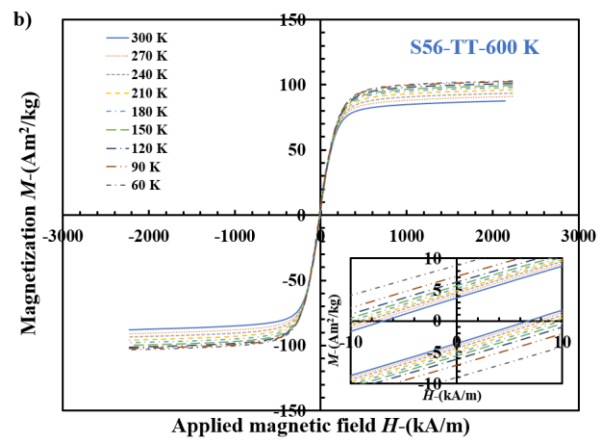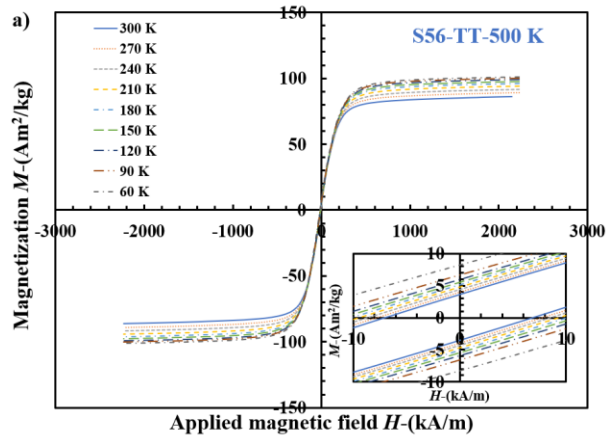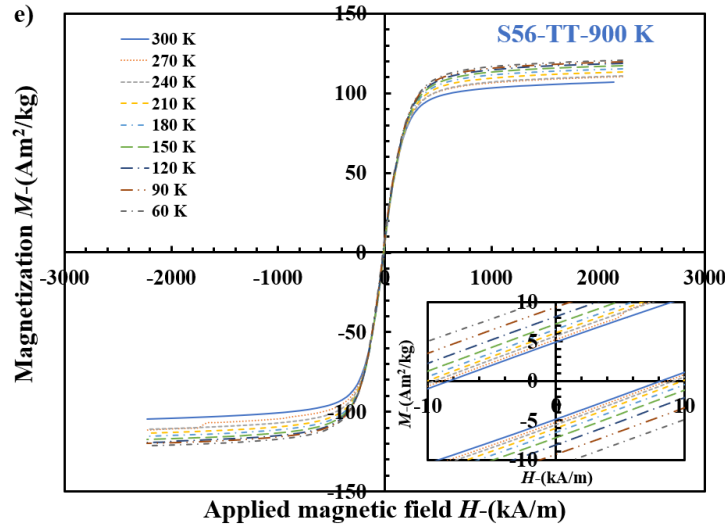
Figure 68 *MvH* curves of the milled powder of 56 h (S56) thermally treated at a) 500 K, b) 600 K, c) 700 K, d) 800 K, and e) 900 K; at sub-ambient temperatures (60 - 300 K). Inset in each figure shows the curve at a low-magnetic-field region (±10 kA/m)

The variation of M_S, H_{CI}, and M_R for the thermally treated S56 powders at sub-ambient temperatures concerning the temperature are presented in Figure 69 a, 69 b, and 69 c. M_S increased with a decrease in temperature in all the thermally treated powders, irrespective of thermal treatment temperatures. M_S increased gradually by ~15-18% at ~60 K when compared to that of the thermally treated powder at ambient temperature for the thermally treated powder. The observed experimental results were fitted with equation (5) (Bloch's Law), and M_S (0) was estimated. The M_S (0) was estimated to be in the range between ~103.01 Am^2/kg to ~ 122.55 Am^2/kg, as shown in Figure 69 a. The M_S (0) exhibited a trend of an increase in its value with the increase in thermal treatment temperature.
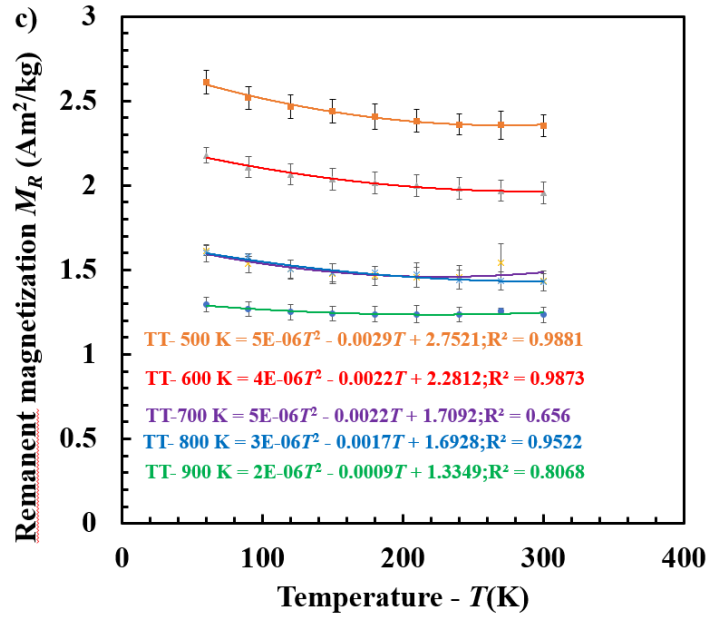
a)

Saturation magnetization M_S (Am²/kg)

TT-500 K=$103.01[1-(3.1\times10^{-5})T^{3/2}]$
TT-600 K=$104.90[1-(3.1\times10^{-5})T^{3/2}]$
TT-700 K=$106.50[1-(3.1\times10^{-5})T^{3/2}]$
TT-800 K=$111.33[1-(2.8\times10^{-5})T^{3/2}]$
TT-900 K=$122.55[1-(2.6\times10^{-5})T^{3/2}]$

Temperature - T(K)

b)

Intrinsic coercivity H_{CI} (kA/m)

TT- 500 K = $0.0001T^2 - 0.0875T + 21.13$; $R^2 = 0.9635$
TT- 600 K = $0.0002T^2 - 0.1079T + 23.076$; $R^2 = 0.9641$
TT- 700 K = $0.0002T^2 - 0.1255T + 25.643$; $R^2 = 0.9787$
TT- 800 K = $0.0002T^2 - 0.1241T + 26.189$; $R^2 = 0.99$
TT- 900 K = $0.0002T^2 - 0.1071T + 24.223$; $R^2 = 0.9956$

Temperature - T(K)

c)

TT- 500 K = $6E{-}05T^2 - 0.0373T + 9.8873; R^2 = 0.9702$
TT- 600 K = $8E{-}05T^2 - 0.0475T + 11.071; R^2 = 0.9715$
TT- 700 K = $9E{-}05T^2 - 0.0507T + 11.12; R^2 = 0.9825$
TT- 800 K = $1E{-}04T^2 - 0.0594T + 13.385; R^2 = 0.9922$
TT- 900 K = $9E{-}05T^2 - 0.055T + 13.567; R^2 = 0.9966$

Figure 69 Variation of a) saturation magnetization (M_S) and b) intrinsic coercivity (H_{CI}), and c) remanent magnetization (M_R) with temperature (T) of the thermally treated (500-900 K) S56 sample, at sub-ambient temperatures (60 - 300 K)

H_{CI} and M_R increased gradually with the decrease in temperature, irrespective of the thermal treatment temperature. The trends of H_{CI} and M_R converge with each other from 300- 60 K. The trend of the H_{CI} and M_R of these samples was fitted using a quadratic equation, and the equations are shown in figure 69 b and 69 c. The $H_{CI}(0)$ and $M_R(0)$ was estimated from the fitted equations. The $H_{CI}(0)$ was estimated to be in the range between ~21 kA/m to ~26 kA/m. $M_R(0)$ was estimated to be in the range of ~10 Am²/kg to ~13.6 Am²/kg.

The motivation of this research work is to characterize the structural and magnetic properties of the commercially available pre alloyed gas atomized powder and investigate the phase evolution in the powder due to mechanical milling and their associated structural and magnetic characterization. The thermal stability of these powders in both structural and magnetic properties was studied from sub-ambient as low as ~60 K to elevated temperatures as high as ~900 K. The magnetic properties of the thermally treated powders were studied at ambient and sub-ambient temperatures.

CHAPTER 6: CONCLUSIONS

The structure and the magnetic properties of the pre-alloyed gas-atomized and the milled maraging steel powders in a temperature regime of cryogenic temperatures as low as~60 K to elevated temperatures as high as ~ 900 K. Following are the conclusions from this work:

1) The pre-alloyed gas atomized powder was primarily comprised of the martensite (α) and austenite (γ). The powder particle size characteristics, D_{90} of the as-received powder was estimated as ~21 μm. The saturation magnetization (M_S), intrinsic coercivity (H_{CI}) and remanent magnetization (M_R) of the as-received powder at ambient temperature was ~176 Am^2/kg, ~3 kA/m, and ~1.4 Am^2/kg, respectively.

2) Even after thermal treatment, at temperatures as high as 900 K, the as-received powder showed minimal change in the M_S. The H_{CI} and M_R decreased, giving a sign of excellent soft-magnetic properties. Also, no changes were observed in the XRD patterns even after thermal treatment. The as-received powder can be reused.

3) Mechanical milling of the pre-alloyed gas atomized powder resulted in the evolution of new phases. Powders milled for 3 h to 8 h comprised of nanocrystalline martensite. While milling more than 8 h resulted in the formation of austenite and other extraneous intermetallic phases.

4) Mechanically milled powders for 3 h, 5 h, and 8 h showed the presence of martensitic nanocrystalline grains. The grain size of these powders was estimated as ~48 nm (3 h), ~17 nm (5 h), and ~21 nm (8 h). The lattice parameter was estimated to be ~0.2873 nm.

5) The powder particle size characteristics, D_{90} for the nanocrystalline milled powders (milled for 3h, 5h, and 8h) were estimated as ~ 8.5 μm, ~8.9 μm, and ~5.7 μm respectively. While the D_{90} of the milled powders more than 8 h maintained a range between ~4 – 5.5 μm.

6) The M_S decreased with the increase in the milling duration, while the H_{CI} and M_R showed no specific trend with the increase in milling time but were greater than that of the nanocrystalline powders. The M_S, H_{CI} and M_R of the nanocrystalline milled powders (3h,

5h, and 8h) ranged between ~ 164 Am^2/kg to ~169 Am^2/kg, from ~4.9 kA/m to ~6.7 kA/m and ~3.4 Am^2/kg to 3.9 Am^2/kg respectively.

7) The saturation magnetization (M_S) decreased with the increase in the temperature from 60 K to 300 K. The $M_S(0)$ and the maximum magnetic moment per atom (μ_H) decreased with the increase in the milling duration. The $M_S(0)$ and μ_H of the as-received powder was estimated to be ~188.95 Am^2/kg and ~ 1.93 μ_B. The $M_S(0)$ and μ_H of the nanocrystalline milled maraging powders ranged between ~ 178 Am^2/kg and ~ 1.83 μ_B. The $M_S(0)$ decreased and reached a minimum of ~101 Am^2/kg and ~ 1.05 μ_B in the milled powders for 56 h.

8) The thermomagnetic behavior of the as-received and the milled powders (3h, 5h, 8h, and 56 h) from 300-900 K showed a fairly reversible nature. With the increase in temperature, M_S and H_{CI} decreased gradually in both the as-received powder and the milled powder for 5h. The M_S and H_{CI} of the as-received sample decreased from ~176Am^2/kg (300 K) to ~ 143Am^2/kg (900 K) i.e., by ~19 % and ~ 1.5 times i.e., from ~3 kA/m (300 K) to ~2 kA/m (900 K) While the M_S and H_{CI} of the milled powder for 5 h decreased from ~165 Am^2/kg (300 K) to ~ 128 Am^2/kg (900 K) i.e., by ~22 % and ~ by ~2 times i.e., from ~4.9 kA/m (300 K) to ~ 2.3 kA/m (900 K).

9) The as-received powder milled for 5h followed by thermal treatment temperature of ~ 900 K resulted in nanocrystalline martensitic milled maraging steel powders having similar M_S to the as-received powder. H_{CI} was less when compared to the as-received gas atomized powder showing promising better magnetic properties.

CHAPTER 7: FUTURE WORK

During mechanical milling of the pre-alloyed gas atomized powder resulted in the formation of intermetallic precipitates, it reduced the magnetization. Further investigation is in progress to understand the intermetallic phases evolved during mechanical milling. This will be studied by using TEM studies.

The emergence of a new phase or the disappearance of existing phases during the heat treatment at elevated temperatures is to be investigated using an in-situ high-temperature X-ray diffraction equipment and in-situ TEM which could help in the understanding the changes in magnetic properties.

As there is an increase in the magnetic properties of the milled powder for 5 h after thermal treatment at ~900 K. Annealing studies is to be performed to investigate the changes in the magnetic properties. Also, the magnetic and structural characterization with temperature is to be performed on the nanocrystalline milled maraging steel powder for 8 h.

REFERENCES

[1] S. Floreen, (1968) The physical metallurgy of maraging steels, Metallurgical Reviews, 13:1, 115-128. (https://doi.org/10.1179/mtlr.1968.13.1.115)

[2] B.-Z. Weiss, (1983) Maraging steels- Structure, properties, and applications

[3] K. Detert, (1967) The influence of small cold deformation preceding aging in 15% and 18 % nickel maraging steel, Transactions of Metallurgical Society of AIME, 239, 553-556.

[4] V.N. Antisiferov, Yu.M. Kolbenev, (1972) A maraging steel produced by powder metallurgy method, Poroshkovaya Metallurgiya, 4 (112) 40-43.

[5] L. F. Van Swam, R. M. Pelloux & N. J. Grant, (1974) Properties of maraging steel 300 produced by powder metallurgy, Powder Metallurgy 17(33) 33-45. (https://doi.org/10.1179/pom.1974.17.33.004)

[6] M.L. Schmidt, (1988) Maraging steels: Recent developments and applications, The Minerals, Metals & Materials Society, 213-235.

[7] K. Rohrbach, M.L. Schmidt, (1990) Maraging steels, ASM Handbook, Volume 1 Properties and selection: Irons, Steels, and High-Performance Alloys, 793-800.

[8] U.K. Viswanathan, G.K. Dey, and M.K. Asundi, (1993) Precipitation hardening in 350-grade maraging steel, Metallurgical TransactionsA., 24A, 2429-2442.

[9] F. Habiby, T. N. Siddiqui, H. Hussain, A. UL. Haq, A. Q. Khan, (1996) Lattice changes in the martensitic phase due to ageing in 18 wt% nickel maraging steel grade 350, Journal of Materials Science, 31, 305-309.

[10] K.Kempen, E.Yasa, L.Thijs, J.-P. Kruth, J.Van Humbeeck, (2011) Microstructure and mechanical properties of Selective Laser Melted 18Ni-300 steel, Physics Procedia 12, 255–263.

[11] J. M. Pardal, S. S. M. Tavares, M. P. Cindra fonseca, H. F. G. Abreu, and J. J. M. Silva (2006) Study of the austenite quantification by X-ray diffraction in the 18Ni-Co-Mo-Ti maraging 300 steel, Journal of Materials Science 41 2301–2307.

[12] R. Tewari, S. Mazumder, I.S.Batra, G.K. Dey, S. Banarjee, (2000) Precipitation in 18 wt.% Ni maraging steel of grade 350, Acta Mater. 48 (5) 1187-1200.

[13] F. Zhu, Y. F. Yin & R. G. Faulkner, (2011)Microstructural control of maraging steel C300, Materials Science and Technology,27(1)395-405. (https://doi.org/10.1179/026708309X12506933873503)

[14] G.M. Castro Guiza, C.A.S. Oliveira, (2016) Microstructural changes produced by hot forging in a C 300 maraging steel, Materials Science & Engineering A 655, 142–151.

[15] Venceslau Xavier Lima Filhoa, Isabel Ferreira Barrosa, Hamilton Ferreira Gomes de Abreua, (2017) "Influence of Solution Annealing on Microstructure and Mechanical Properties of maraging 300 Steel", Materials Research, 20(1) 10-14. (http://dx.doi.org/10.1590/1980-5373-MR-2016-0257)

[16] Naoki Takata, Ryoya Nishida, Asuka Suzuki, Makoto Kobashi, and Masaki Kato, (2018) Crystallographic Features of Microstructure in maraging Steel Fabricated by Selective Laser Melting, Metals 8, (440) 1-10.

[17] S. Yin, C. Chen, X. Yan, X. Feng, R. Jenkins, P. O'Reilly, M. Liu, H. Li, R. Lupoi, (2018) The influence of aging temperature and aging time on the mechanical and tribological properties of selective laser melted maraging 18 Ni-300 steel, Additive Manufacturing 22, 592-600.

[18] B.L. Averbach and M. Cohen: (1948) Trans. Am. Inst. Min. Eng., (176) 401.

[19] Adriano Gonçalves dos Reis, Danieli Aparecida Pereira Reis, Antônio Jorge Abdalla, Antônio Augusto Couto, and Jorge Otubo, (2016) An In-Situ High-Temperature X-Ray Diffraction Study of Phase Transformations in maraging 300 Steel, Defect and Diffusion Forum (371) 73-77.

[20] D.A. Colling, (1971) Soft magnetic structural alloys for elevated temperature applications, IEEE T. Magn., Vol. MAG-7 (1), 91-101.

[21] I.J. Garshelis, (1990) Magnetic and magnetoelastic properties of 18% nickel maraging steel, IEEE T. Magn., 26 (5) 1981-1983.

[22] M. Ahmed, A. Ali, S. K. Hasnain, F. H. Hashmi, and A. Q. Khan, (1994) Magnetic properties of maraging steel in relation to deformation and structural phase transformations, Acta Materialia, 42 (3), 631-638.

[23] M. Ahmed, S. K. Hasnain, I. Nasim, H. Ayub, (1995) Magnetic properties of maraging steels about nickel concentration, Metall. Mater. Trans A (26), 1869-1876.

[24] S.S.M. Tavares, H.F.G. Abreu, J.M. Neto, M.R. da Silva, I. Popa, (2003) A thermomagnetic study of the martensite–austenite phase transition in the maraging 350 steel, Journal of Alloys and Compounds 358, 152–156.

[25] S. S. M. Tavares, H. F. G. Abreu, J. M. Neto, M. R. da Silva, I. Popa, (2004) A magnetic study of maraging 350 steel, Journal of Magnetism and Magnetic Materials 272-276 ,785-787.

[26] S.S.M. Tavares, M.R. da Silva, J.M. Neto, J.M. Pardal, M.P. Cindra Fonseca, H.F.G. Abreu, (2004) Magnetic properties of a Ni–Co–Mo–Ti maraging 350 steel, Journal of Alloys and Compounds, 373, 304–311.

[27] S.S.M. Tavares, M.R. da Silva, J.M. Neto, J.M. Pardal, M.P. Cindra Fonseca, H.F.G. Abreu, (2007) Influence of temperature and aging time on hardness and magnetic properties of the maraging steel grade 300, J Mater Sci, 42,2276–2281.

[28] Metal powder EOS Maraging Steel MS1, Mill test certificate/ Material Safety Data Sheet, EOS Finland, 2018.

[29] B. S. Murthy, S. Ranganathan, (1998) Novel materials synthesis by mechanical alloying, Inter. Mater. Rev.,43:3, 101-141.

[30] R.M. Bozorth, (1993) Ferromagnetism, 3rd edition. IEEE Press, New York, 190-209.

[31] C. Suryanarayana, (2001) Mechanical alloying and milling, Prog. Mater. Sci. 46, 1–184.

[32] C. Suryanarayana, (2004) Mechanical Alloying and Milling, 1st edition. (Marcel Dekker, New York).

[33] R.M. German, (2005) Powder metallurgy and particulate processing (Metal Powder Industries Federation, New Jersey).

[34] L. Lü and M. O. Lai, (2013) Mechanical Alloying. Springer US

[35] J.S. Benjamin, T.E. Volin, (1974) The mechanism of mechanical alloying. Met. Trans. 5(9) 1929–1934.

[36] K.M. Krishnan, (2016) Fundamentals and Applications of Magnetic Materials, 1st edition, Oxford University Press.

[37] J.W. Jeffrey, (1971) Methods in X-ray crystallography, Academic Press Inc. London.

[38] C. Suryanarayana, M.G. Norton, (1998) X-ray Diffraction: A Practical Approach (Springer Science-Business Media, Plenum Publishing Corporation, New York, 153-166.

[39] B.D. Cullity, S.R. Stock, (2001) Elements of X-ray Diffraction, 3rd, Prentice Hall, Upper Saddle River, 376-383.

[40] C. Kittle, (2004) Introduction to Solid State Physics, 8th ed., John Wiley & Sons Inc.

[41] T. Ferreira, W. Rasband, (2012) Image J use guide (ImageJ/Fiji 1.46).

[42] B.D. Cullity, C.D. Graham, (2009) Introduction to the magnetic materials, IEEE Press, Wiley, Hoboken.

[43] S. Chikazumi, (1964) Physics of Magnetism, John Wiley & Sons Inc.

[44] M. Dittrich, G. Schumacher, (2014) Evolution of crystallite size, lattice parameter and internal strain in Al precipitates during high energy ball milling of partly amorphous $Al_{87}Ni_8La_5$ alloy, Materials Science & Engineering A, 604, 27–33.

[45] W.H. Qi, M.P. Wang, (2005) Size and shape dependent lattice parameters of metallic nano particles, J. Nanopar. Res., 7, 51-57.

[46] K. Lu, Y.H. Zhao, (1999) Experimental evidence of lattice distortion in nanocrystalline materials, Nanostruct. Mater. 12,559-562.

[47] G. Herzer, (1990) Grain size dependence of coercivity and permeability in nanocrystalline ferromagnets, IEEE T. Magn. 26 (5) 1397.

[48] G. Herzer, (1989) Grain structure and magnetism of nanocrystalline ferromagnets, IEEE T. Magn. 25 (1) 3327.

[49] J.B. Lecomte, C. Servant, G. Cizeron, (1985) A comparison of the structural and evolution occurring during anisothermal or isothermal treatments in the case of nickel and manganese type maraging steels, J. Mater. Sci., 20, 3339-3352.

[50] Farooque, H. Ayub, A. UL Haq, and A. Q. Khan, (1998) The formation of reverted austenite in 18% Ni 350 grade maraging steel, JOURNAL OF MATERIALS SCIENCE, 33, 2927—2930.

[51] Kurnsteiner, Markus B. Wilms, Andreas Weisheit, Pere Barriobero-Vila, Eric A. Jagle, Dierk Raabe, (2017) Massive nanoprecipitation in Fe-19Ni-xAl maraging steel triggered by the intrinsic heat treatment during laser metal deposition, Acta Materialia 129, 52-60.

[52] Hamilton F.G. Abreu, Jean J. Silva, Manoel R. Silva, Marcelo J. Gomes da Silva, (2015) The influence of reverted austenite on the texture and magnetic properties of 350 maraging steel, Journal of Magnetism and Magnetic Materials 393, 99–104.

[53] K.W. Andrews, (1965) Empirical formulae for the calculation of some transformation temperatures, J. Iron Steel Inst. 203, 721.

[54] R.K. Viswanathan, S.K. Mannan, S. Kumar, (1988) Mechanical alloying behavior in the group V transition metal/silicon systems, Scr, Metall 22, 1011-1014.

[55] Ganesh Varma Thotakura, Anuj Rathi, Tanjore V. Jayaraman, (2019) Structure and magnetic properties of mechanically alloyed nanocrystalline Fe-46 at.% Co-34 at.% Ni-20 at.% alloy powder from cryogenic to elevated temperatures, Applied Physics A, 125:235. (https://doi.org/10.1007/s00339-019-2535-7)